UNIVERSIDAD NACIONAL AUTÓNOMA DE MÉXICO

PROGRAMA DE MAESTRÍA Y DOCTORADO EN INGENIERÍA

CENTRO DE INVESTIGACIÓN EN ENERGÍA

DINÁMICA DE FLUJOS EN OBSTÁCULOS MAGNÉTICOS

T E S I S

QUE PARA OPTAR POR EL GRADO DE:

DOCTOR EN INGENIERÍA
ENERGÍA - SISTEMAS ENERGÉTICOS

P R E S E N T A :
M. I. ALBERTO BELTRÁN MORALES

T U T O R :
DR. SERGIO CUEVAS GARCÍA

SEPTIEMBRE 2010

Universidad Nacional Autónoma de México
UNAM
Biblioteca Central
Dirección General de Bibliotecas de la UNAM

UNAM – Dirección General de Bibliotecas
Tesis Digitales
Restricciones de uso

DERECHOS RESERVADOS ©
PROHIBIDA SU REPRODUCCIÓN TOTAL O PARCIAL

Todo el material contenido en esta tesis esta protegido por la Ley Federal del Derecho de Autor (LFDA) de los Estados Unidos Mexicanos (México).

El uso de imágenes, fragmentos de videos, y demás material que sea objeto de protección de los derechos de autor, será exclusivamente para fines educativos e informativos y deberá citar la fuente donde la obtuvo mencionando el autor o autores. Cualquier uso distinto como el lucro, reproducción, edición o modificación, será perseguido y sancionado por el respectivo titular de los Derechos de Autor.

JURADO ASIGNADO

Presidente: Dr. Eduardo Ramos Mora

Secretario: Dr. Cuevas García Sergio

Vocal: Dr. José Roberto Zenit Camacho

1er. Suplente: Dr. Julio Javier Martinell Benito

2do. Suplente: Dr. Raúl Alejandro Avalos Zúñiga

Lugar donde se realizó la tesis:

CENTRO DE INVESTIGACIÓN EN ENERGÍA

TUTOR DE TESIS:

Dr. Sergio Cuevas García

FIRMA

Agradecimientos

A la Universidad Nacional Autónoma de México y en especial al Centro de Investigación en Energía por el apoyo brindado durante mis estudios de doctorado.

A **CONACyT** (Consejo Nacional de Ciencia y Tecnología), por brindarme el financiamiento para realizar mis estudios de doctorado, así como al proyecto CONACYT Ciencia Básica No. 59977 (*Flujos magnetohidrodinámicos en campos magnéticos inhomogéneos*) por el apoyo recibido.

Agradezco a todos mis amigos de estos 6 aos en el CIE.

Dedicado a mi familia.

Contents

1 Introduction **1**

2 MHD mathematical formulations **7**
2.1 Background 7
2.2 Formulation based on the electric scalar potential: φ-formulation . . . 9
2.3 Formulation based on the induced magnetic field: B-formulation . . . 10
2.4 Formulation based on the induced electric current density: j-formulation 12

3 The flow past a magnetic obstacle **17**
3.1 Background 17
3.2 Liquid metal flow past a magnetic obstacle: B- and j-formulation 2D comparison 20
3.2.1 Boundary conditions and numerical implementation 23
3.2.2 Numerical method 23
3.2.3 Preliminary description of the flow 25
3.2.4 Numerical results 29
3.2.5 Some dynamic properties of a magnetic obstacle 33
3.3 Quasi-two dimensional approach 38
3.3.1 Q2D Liquid metal flow past a magnetic obstacle 40
3.3.2 Q2D Electrolytic flow past a magnetic obstacle 47
3.4 3D numerical simulation of the electrolytic flow past a magnetic obstacle. 55
3.4.1 Parallelization strategy 57
3.4.2 Numerical results 59

4 Oscillatory Magnetic Obstacle **73**
4.1 Oscillating magnetic obstacle in a liquid metal layer 74

4.1.1 Formulation 75
4.1.2 Numerical results 77
4.1.3 Bifurcation map 85
4.2 Theoretical bifurcation analysis 86
4.3 Oscillating magnetic obstacle in an electrolytic layer 90
4.3.1 Experimental results 90
4.3.2 Numerical results 92

5 Conclusions **97**

References **101**

Resumen

El presente estudio está enfocado en el análisis numérico de flujos de fluidos eléctricamente conductores, tanto de metales líquidos como electrolitos, bajo campos magnéticos espacialmente localizados. La interacción del campo magnético con corrientes eléctricas inducidas por el movimiento del fluido (en el caso de los metales líquidos) o externamente inyectadas (en el caso de los electrolitos) crea una fuerza de Lorentz que actúa como un obstáculo para el flujo (*obstáculo magnético*), dando lugar a una variedad de patrones de flujo que exhiben un comportamiento dinámico muy rico. El propósito principal de esta tesis es profundizar en el conocimiento de este tipo de flujos y desarrollar modelos numéricos y estrategias computacionales adecuados para su exploración. El estudio está motivado en diversas aplicaciones industriales, tales como el mezclado y frenado electromagnéticos y la velocimetría por fuerza de Lorentz, donde los campos magnéticos localizados juegan un rol fundamental. Primeramente, se presentan las ecuaciones de la magnetohidrodinámica (MHD) en la aproximación de números del Reynolds magnético bajos, basadas ya sea en el potencial eléctrico o en el campo magnético inducido. Adicionalmente, se introduce una nueva formulación de las ecuaciones de la MHD basada en la densidad de corriente eléctrica inducida. Se exploran dos problemas físicos. Primero, utilizando modelos numéricos bidimensionales y cuasi-bidimensionales, se estudia el flujo rectilíneo de un fluido conductor (un metal líquido o un electrolito) a través de un obstáculo magnético, comparando los resultados, cuando es posible, con patrones de flujo experimentales. Adicionalmente, se explora el flujo tridimensional en una capa delgada de electrolito a través de un campo magnético localizado, usando una versión paralelizada del código numérico. En el segundo problema se exploran los patrones de flujo en una capa delgada de un fluido conductor, producidos por el movimiento armónico oscilatorio de un campo magnético localizado. En el caso de un metal líquido, el problema se analiza numéricamente explorando las bifurcaciones del flujo conforme se varía la frecuencia de oscilación. Adicionalmente, se presentan resultados experimentales y numéricos del patrón de flujo en una capa

delgada de electrólito, producido por por la inyección de una corriente directa paralela al eje de oscilación del campo magnético.

Abstract

The present study is devoted to the numerical analysis of flows of electrically conducting fluids, either liquid metals or electrolytes, under localized non-uniform magnetic fields. The interaction of the field with electric currents induced by the fluid motion (in the case of liquid metals) or externally injected (in the case of electrolytes) creates a Lorentz force that acts as an obstacle for the flow (a *magnetic obstacle*) and gives rise to a variety of flow patterns that show a rich dynamic behavior. The main purpose of this thesis in to provide a deeper physical understanding of these flows and develop suitable numerical models and computational strategies that allow their exploration. The study is motivated in several applications in the process and metallurgical industries, such as electromagnetic stirring, electromagnetic braking and Lorentz force velocimetry, where spatially localized magnetic fields play a fundamental role. The magnetohydrodynamic (MHD) equations for low magnetic Reynolds number flows based on either the electric potential or the induced magnetic field, are presented. In addition, a new formulation of the MHD equations based on the induced electric current density is introduced and tested. Two physical problems are explored. First, the rectilinear flow of a conducting fluid (a liquid metal or an electrolyte) past a magnetic obstacle is addressed with two-dimensional and quasi-two-dimensional numerical models. Whenever possible, a comparison with experimental flow patterns is provided. In addition, the three-dimensional shallow flow of an electrolyte past a localized magnetic field is explored using a parallelized version of the numerical code. The second problem deals with the analysis of flow patterns in a thin layer of a conducting fluid produced by the oscillatory harmonic motion of a localized magnetic field. This problem is analyzed numerically for the case of a liquid metal, exploring the flow bifurcations as the oscillation frequency is varied. Also, experimental and numerical results of the flow patterns generated in a thin electrolytic layer when a D.C. current is injected in a direction parallel to the axis of oscillation of the magnetic field, are presented.

Chapter 1

Introduction

Recently, the analysis of electrically conducting fluid flows influenced by non-uniform and, particularly, local external magnetic field has gained a considerable interest from theoretical and practical points of view. In fact, many technological applications such as fusion reactors and metallurgical process involve the flow of conducting fluids under non-uniform magnetic fields. In nuclear fusion reactors, extremely hot plasma volumes are kept away from the walls of the reactor by an intense magnetic field of the order of 10 Tesla, generated by a set of superconducting magnet coils. A liquid metal blanket is placed between the plasma and the coils,to among other goals, evacuate the heat from the fusion reactions and convert it into useful power. In many zones of the blanket, the liquid metal has to flow under a strongly non-uniform magnetic field that influences the flow dynamics (Abdou et al. 2001, Smolentsev et al. 2006). Industrial applications of localized magnetic fields are present in the field of metallurgical processes, (e.g. Davidson 1999), including stirring of melts by electromagnetic forces (called electromagnetic stirring, e.g. Kunstreich 2003) and damping of undesired turbulent fluctuations during steel casting using steady magnetic fields (called electromagnetic braking, e.g. Takeuchi et al. 2003). On the other hand, a non-contact technique for velocity measurements in liquid metals, called Lorentz force velocimetry (LFV) (Thess et al. 2006), has been developed. It is based on exposing the fluid to a localized magnetic field and measuring the drag force acting upon the magnetic field lines. The volume flux is related with the drag force and hence the mass flux is inferred. This non-contact technique is suited for high-temperature applications. It is important to note that, in the LFV experiments vortical flow structures can appear, due to the interaction of the induced currents with the localized magnetic field, and should be

accounted for the measurements (Kolesnikov et al. 2008).

From the fundamental side, it has been recently recognized that rectilinear flows of conducting fluids exposed to localized non-uniform magnetic fields, posses a rich variety of dynamical states, that can be compared to the classical problem of flows past bluff bodies (Cuevas et al. 2006a, Cuevas et al. 2006b, Votyakov et al. 2007). These flows exhibit several patterns such as, a steady open-streamline flow, steady vortex pair and even vortex shedding, as well as more complex patterns. In fact, flows of conducting fluids in localized magnetic fields are worth exploring fluid dynamical systems which can shed new light on flows in ordinary hydrodynamics (Andreev et al. 2009, Afanasyev and Korabel 2006). Presenting specific differences according to the working fluid, these flows have been explored using either electrolytes or liquid metals (LM). They can be produced when the conducting fluid flows in a main direction passing through a fixed localized magnetic field or by dragging a permanent magnet longitudinally close to a quiescent conducting fluid layer. The flow pattern is produced by a Lorentz force, which is due to the interaction of the non-uniform localized magnetic field with induced or injected electric currents. In experiments with electrolytes, owing to the low electrical conductivity of the liquid, induced currents produced by the relative motion of the fluid and the magnetic field are negligible. Therefore, in order to create a Lorentz force capable of braking the fluid and producing vorticity, it is required to inject an electrical current in the transversal direction. On the other hand, when LM are used, the high electrical conductivity of the medium gives rise to strong induced electric currents which interact with the field, producing a non-negligible Lorentz force localized in the in the zone where the applied magnetic field has a strong intensity, which represents a small fraction of the total flow domain. In both electrolytic and LM flows the Lorentz force opposes the oncoming flow and, as a matter of fact, acts as an obstacle, where stagnation and reverse flow regions may appear and lead to steady or time dependent flow patterns. In order to emphasize the analogy of flows of conducting fluids passing through a localized zone of applied magnetic field, and ordinary flows around solid obstacles and describe the obstruction found by the fluid as it moves through a zone of localized magnetic field the term *magnetic obstacle* was recently coined (Cuevas et al. 2006a, Cuevas et al. 2006b). It is important, however, to stress that fundamental differences exist between flow past solid and magnetic obstacles, as will be shown in this work.

It appears that the first experiments of magnetic obstacle flows with electrolytes were performed by Honji (1991) where two permanent magnets were located externally so that a small zone of a thin layer of an electrolyte was between a north - south pole magnetic field. The magnets were moved at a constant velocity along the centreline of a water tank while a steady electric current was imposed on the fluid layer transversely to the motion of the magnets. For a sufficiently high velocity of the magnet pair and imposed electric current, Honji observed a wavy motion in the far wake behind the

region influenced by the field. In a subsequently study, Honji and Haraguchi (1995) dragged a single permanent magnet underneath a thin layer of an aqueous electrolytic solution, injecting a direct electric current transversely. The interaction of this current with the applied magnetic field generated a Lorentz force that produced different flow patterns, depending on the velocity of the magnet and the electric current, such as a steady vortex pair and a periodic vortex shedding. More recently, similar experiments were performed by Afanasyev and Korabel (2006) dragging the magnet over a thin layer of a stratified electrolytic fluid. These authors explored flows produced by a single magnet as well as by two magnets with opposite orientations and aligned with the direction of the motion. For the case of a single magnet, the initial formulation of vortex dipoles and their subsequent shedding were observed, while for the case of two magnets the inverted Kármán vortex street, consisting of interconnected vortex quadrupoles was found. This study was motivated by the analysis of self-propelled bodies which on a large scale seem to be produced by localized forces. It is important to emphasize that while dealing with electrolytes, where induced currents are negligible, the theoretical description of these flows can be based on the hydrodynamic equations with a specified Lorentz force.

On the other hand, in LM fows under localized magnetic fields strong induced currents appear, in such a way that the flow dynamics is coupled with the electromagnetic field and therefore, a magnetohydrodynamic (MHD) description is necessary. A very illustrative experiment of a LM flow past a magnetic obstacle is shown in an educational film by Shercliff (1965), where a layer of mercury at rest is placed in between the poles of a magnet. As the magnet is moved manually, a vortex-type flow develops in the zone affected by the magnetic field and a wake is created. Shercliff's qualitative experiment seems to be the first one that showed the effect of a moving localized magnetic field on a liquid metal. However, this effort was not followed by additional quantitative experiments or theoretical models that could shed more light on these interesting flows. Apart from a numerical calculation by Gelfgat et al. (1978) that found a kind of recirculation in the flow of a LM in a localized field, and a subsequent experiment that failed to confirm these results (Gelfgat and Olshanskii 1978), no other studies were reported on this topic in the last century. Recently, the interaction of a uniform LM duct flow with a localized magnetic field was analyzed numerically by Cuevas et al. (2006a) with a quasi-two-dimensional (Q2D) model that considers the effect of the boundary layers through a friction term that includes both the viscous and the magnetic friction (Hartmann braking). Considering the case where inertial effects dominate over diffusive ones, it was shown that induced currents interacting with the applied field create an opposing non-uniform Lorentz force that is able to generate steady vortex pairs and that, under certain conditions, an instability leading to vortex shedding can appear. In further study, Cuevas et al. (2006b) analyzed the LM flow past a magnetic obstacle but restricted to the creeping flow regime, finding

steady patterns of two and four vortices. Previous works motivated new numerical calculations as well as experimental studies that have shown new aspects of LM flows past magnetic obstacles. In particular (Votyakov et al.) (2007,2008) showed that stationary flow patterns in these flows can be more complex than in the wake behind a solid body. They found that the steady flow undergoes two bifurcations (instead of one) that involve up to six vortices (instead of two). The first bifurcation creates a pair of vortices within the region of magnetic field that are called inner magnetic vortices. In turn, the second bifurcation produces a pair of attached vortices that are linked to the inner vortices by a pair of connecting vortices. Several experiments using LM in rectangular domains under non-uniform magnetic fields have been reported recently in the literature (Andreev et al. 2006, Kolesnikov et al. 2008, Andreev et al. 2009). In all of them the working fluid was GaInSn eutectic alloy. Andreev et al. (2006) performed an experimental study in a rectangular duct under the influence of an inhomogeneous magnetic field generated by two permanents magnets located at some distance from the duct inlet. This kind of experimental configuration is relevant under a wide variety of circumstances ranging from magnetic breaking in steel casting to electromagnetic stirring in aluminium production. In turn, Andreev et al. (2009), explored this flow configuration using an ultrasonic velocimeter obtaining two-dimensional flow maps, which confirm the new typological configuration consisting of three pairs of vortices. Kolesnikov et al. (2008), using an experimental configuration with a moving permanent magnet, also reported three pairs of vortices, in a thin layer of GaInSn alloy with a solution of HCl covering the liquid metal surface.

In spite of the experimental and theoretical advances of the last years, the dynamic behavior of flows of electrically conducting fluids in magnetic obstacles is far from being fully understood. Hence, the main purpose of this thesis is to provide a deeper physical understanding of flows of conducting fluids, both electrolytes and LM, in localized non-uniform magnetic fields. With this aim, this work addresses, on the one hand, the development of numerical models and computational strategies that allow a more realistic description of the flows of interest and, on the other, the exploration of new physical situations that involve the interaction of conducting fluids with localized fields. Although LM flows under uniform magnetic fields have been widely explored, flows under non-uniform magnetic fields have received much less attention, owing to their higher complexity. The search of suitable numerical approaches for these flows is still a current field of research. In the present work, a new formulation of the MHD equations (Smolentsev et al. 2010) that considers the electric current density as a dependent variable (j-formulation) is presented and tested numerically considering the flow past a magnetic obstacle, in steady and time-dependent states. In the present study, this flow is analyzed with a generalized approach that can be applied either to electrolytes or LM flows. Further, different numerical models with an increasing degree of complexity, namely, two-dimensional (2D), quasi-two-dimensional (Q2D) and three-

dimensional (3D) are considered, which allow to reproduce experimental flow patterns reported in the literature. It is worth mentioning that for the 3D flow analysis, a parallelized version of the numerical code has been developed using MPI functions. In addition, a new physical problem is considered: the vortex flow generated by an oscillatory magnetic obstacle. This problem is addressed in two cases. In the first one, using a 2D numerical approach, the bifurcation analysis of the vortex flow in a LM layer is carried out as the oscillation frequency of the magnetic obstacle is varied. In the second case, the vortex generation in a thin layer of an electrolyte due to the interaction of an oscillating magnetic dipole (a permanent magnet) and a DC current, injected in a direction parallel to the axis of oscillation of the magnet, is considered experimentally and preliminary numerical results are presented.

Apart from the present introductory chapter, the thesis contains four additional chapters. In chapter two, a general overview of two of the most common mathematical formulations for the analysis of low magnetic Reynolds number magnetohydrodynamic (MHD) flows is presented. The first one is based on the scalar electric potential and a second one, on the induced magnetic field. In addition, a new formulation is derived (denominated j-formulation), which is based on the induced electric current. Main advantages and disadvantages of this new formulation, compared with the other two, are presented.

Chapter three is focused on the numerical analysis of the shallow flow of a conducting fluid past a localized non-uniform magnetic field. This flow is simulated using a two-dimensional (2D) model by implementing both the B- and j-formulation, finding a good quantitative comparison. Then a quasi-two dimensional (Q2D) averaged numerical model is proposed, where the vertical diffusion produced by the bottom friction is modeled through a linear term. With this model the experimentally observed six-vortex flow pattern in a LM (Kolesnikov et al. 2008) is reproduced. Also, the steady and time-periodic patterns found in a thin electrolytic layer (Honji and Haraguchi 1995) are obtained. In the last section, a full three-dimensional (3D) model is used to analyze the flow of a shallow layer of an electrolyte, using a parallelized version of the numerical code. The 3D flow structures are analyzed for different force intensities which lead to steady and time-periodic regimes

In chapter four, two variants of a new physical situation, namely, the flow produced by the harmonic oscillation of a localized magnetic field in a quiescent viscous, electrically conducting fluid, are explored. First, the flow patterns created by the oscillating magnetic field in a thin liquid metal layer, are analyzed through a 2D numerical model. In particular, a bifurcation analysis of the different periodic vortex patterns observed as the oscillating frequency varies, is carried out. Secondly, experimental observations in a thin electrolytic layer with a permanent magnet oscillating at different frequencies, and a DC current injected in a direction parallel to the axis of oscillation of the magnet, are reported. For a restricted frequency range, local vortical structures are

formed and shed periodically along the main direction of the applied Lorentz force. A preliminary 2D numerical simulation of this flow is also presented. Finally, in chapter five the main conclusions of this thesis are offered.

Chapter 2

MHD mathematical formulations

In this chapter, the fundamental equations of MHD are presented in three different formulations that can be implemented numerically. Two of these formulations are well known in the literature, namely, the formulations based on the electrical potential (φ-formulation) and on the induced magnetic field (B-formulation). The third formulation has been proposed recently (Smolentsev, Cuevas and Beltrán 2010) and is based on the electric current density (j-formulation). General aspects of these formulations are presented, and the advantages and disadvantages are discussed.

2.1 Background

The governing equations for the flow of electrically conducting incompressible fluids under magnetic fields involve the continuity and Navier-Stokes equations with a Lorentz force term (as the body force) coupled with an additional set of equations, that includes the Maxwell equations for a moving medium and the Ohm's law. It is well known that Navier-Stokes equations can be formulated in different forms based on the choice of the primitive variables (Tannehill et al. 1997) for instance, velocity and pressure ($\mathbf{V}$, P); vorticity (ω) and the stream function (ψ) (in 2D flows); and vorticity - velocity or vector potential - vorticity. Analogously, in the case of MHD flows, the governing equations can also be formulated in different ways. We can refer to several formulations of considerable use that implement the electric scalar (φ) or magnetic vector ($\mathbf{A}$) potentials, as well as the magnetic field ($\mathbf{B}$) (Moreau 1990). An important point to stress here is that modeling ordinary or MHD flows involves the freedom

to chose a proper set of dependent variables. For a particular MHD flow problem, selecting one or another set of electromagnetic variables in combination with a proper numerical technique can result in a higher accuracy and faster convergence. Vice versa an inappropriate choice can lead to unphysical results as well as poor or no convergence at all. The choice of the electromagnetic variables can also affect the size and the shape of the integration domain and the way in which the boundary conditions are formulated that ultimately affects the computation cost. More recently, there have been attempts on implementation of a formulation making use of the induced electric current as the main electromagnetic variable; this formulation avoids some disadvantages specific to the traditional velocity-magnetic field, although so far it has been applied to a few classes of MHD flow problems (see Smolentsev et al. 2010 for a review of the bibliography on this topic).

The behavior of LM MHD flows can be characterized by three dimensionless parameters: the Hartmann number ($Ha = B_0 L\sqrt{\sigma/\rho\nu}$), the Reynolds number ($Re = U_0 L/\nu$), and the magnetic Reynolds number ($Re_m = \mu\sigma U_0 L$). Here, B_0, L and U_0 are the characteristic magnetic field, flow dimension and velocity; while μ, σ, ρ and ν are the magnetic permeability, electrical conductivity, density and kinematic viscosity of the fluid, correspondingly (incidentally for LM and electrolytes $\mu \approx \mu_0$). Hartmann number squared gives an estimate of the ratio of magnetic to viscous forces, while Re estimates the ratio of viscous to inertial forces, and Re_m (when small) estimates the ratio of induced to applied magnetic fields. In most applications involving MHD flows at industrial or laboratory scales with liquid metals, molten salts and electrolytes, Re_m is much less than unity, which means that the field created by induced currents is much smaller than the applied field.

For a viscous, incompressible, electrically conducting fluid with constant material properties in a magnetic field, the governing flow equations can be formulated in terms of the primitive variables $(\mathbf{V}, P)$ as follows

$$\frac{\partial \mathbf{V}}{\partial t} + (\mathbf{V}\cdot\nabla)\mathbf{V} = -\frac{1}{\rho}\nabla P + \nu\nabla^2\mathbf{V} + \frac{1}{\rho}\mathbf{j}\times\mathbf{B^0}, \tag{2.1}$$

$$\nabla\cdot\mathbf{V} = 0. \tag{2.2}$$

The last term on the right-hand-side of the momentum balance equation (2.1) is the Lorentz force, where $\mathbf{j}$ is the electric current density vector. Equation (2.1) has been written in the inductionless approximation (Moreau 1990) by decomposing the magnetic induction (magnetic field) into the applied and induced parts

$$\mathbf{B} = \mathbf{B}^0 + \mathbf{B}^i, \tag{2.3}$$

and then neglecting the induced contribution, $\mathbf{B}^i$, to the Lorentz force, since in inductionless flows $\mathbf{B}^i \ll \mathbf{B}^0$ (which means $Re_m \ll 1$, as was previously mentioned).

Balance equations (2.1)-(2.2) must be complemented by Ampere's and Faraday's laws

$$\mathbf{j} = \frac{1}{\mu}\nabla \times \mathbf{B}, \tag{2.4}$$

$$\nabla \times \mathbf{E} = -\frac{\partial \mathbf{B}}{\partial t}, \tag{2.5}$$

and Ohm's law as a constitutive equation

$$\mathbf{j} = \sigma(\mathbf{E} + \mathbf{V} \times \mathbf{B}), \tag{2.6}$$

where $\mathbf{E}$ is the electric field. From (2.4), it follows that the electric current is solenoidal, i.e.

$$\nabla \cdot \mathbf{j} = 0. \tag{2.7}$$

Both the applied and induced magnetic field in (2.3) are also solenoidal:

$$\nabla \cdot \mathbf{B}^0 = 0, \qquad \nabla \cdot \mathbf{B}^i = 0. \tag{2.8}$$

In addition, the applied magnetic field satisfies the magnetostatic condition,

$$\nabla \times \mathbf{B}^0 = 0, \tag{2.9}$$

which is a consequence of (2.3) and (2.4).

Equations (2.1)-(2.9) govern the flow of a conducting fluid interacting with a magnetic field. In order to solve a particular problem, a given formulation (characterized by a specific set variables) must be selected. Next section outlines the main characteristics of three different MHD formulations.

2.2 Formulation based on the electric scalar potential: φ-formulation

In general terms, different formulations are characterized by the procedure in which induced currents are calculated. In the φ-formulation the induced electric current is calculated directly from Ohm's law. This formulation is very common in the literature of MHD flows (Leboucher 1999, Smolentsev 1999, Votyakov et al. 2008). Assuming the standard conditions of the inductionless approximation are met, the electric field can be treated as potential and expressed in terms of the electric potential, such that $\mathbf{E} = -\nabla\varphi$. Then the induced current equation (2.6), can be rewritten in the following way

$$\mathbf{j} = \sigma(-\nabla\varphi + \mathbf{V} \times \mathbf{B}^0). \tag{2.10}$$

The equation for φ can be obtained by applying the divergence operator to (2.10), assuming the electric conductivity σ to be constant and using (2.7). This results in

$$\nabla^2\varphi + S_\varphi = 0, \tag{2.11}$$

where $S_\varphi = \nabla \cdot (\mathbf{V} \times \mathbf{B}^0)$.

Equations (2.1) and (2.2) along with (2.10) and (2.11) constitute a closed system of equations that characterize the φ-formulation. Note that the applied field $\mathbf{B}^0$ always must satisfy the div- and curl-free conditions.

At the boundaries of the flow domain where thin conducting walls exist, a thin wall condition (Walker 1981) can be used

$$-\sigma\frac{\partial\varphi}{\partial n} = \nabla \cdot (\sigma_w t_w \nabla_\tau \varphi_w), \tag{2.12}$$

where φ_w is the electric potential in the wall, $\mathbf{n}$ is the inward unit normal to the wall with thickness t_w and electric conductivity σ_w. The subscript "τ" represents the projection on the plane tangential to the wall. Condition (2.12) means that the currents leaving the liquid penetrate the wall potential, which to the leading order of approximation does not vary across the wall. Equation (2.11) with the thin wall condition (2.12) have the advantage that the computational domain does not fall outside the flow region. In case of electrically insulated walls, the thin wall condition just reduces to $\frac{\partial\varphi}{\partial n} = 0$.

In spite of all the advantages of the φ-formulation (only one scalar equation exists; the boundary conditions are relatively simple and imposed at the boundaries of the flow domain), using it in computations of high Hartmann number flows may lead to unphysical results. This makes the φ-formulation difficult to implement for most of the high Hartmann number applications and special care is required to avoid spurious numerical effects. It appears that the main source of error during numerical simulations comes from the calculation of induced currents through Ohm's law by subtracting two terms ($\nabla\varphi$ and $\mathbf{V} \times \mathbf{B}^0$) that at high Hartmann numbers have the same order of magnitude. This may introduce numerical inaccuracies which may prevent the condition (2.7) to be satisfied.

2.3 Formulation based on the induced magnetic field: B-formulation

Alternatively to Ohm's law, induced electric currents can also be calculated from Ampère's law:

$$\mathbf{j} = \frac{1}{\mu}\nabla \times \mathbf{B}^i. \tag{2.13}$$

From the point of view of numerical computations, relation (2.13) has some advantage over (2.10). Even with some inaccuracy in $\mathbf{B}^i$, the electric current calculated with (2.13), by virtue of the vector identity $\nabla \cdot (\nabla \times \mathbf{B}^i) = 0$, is always divergence-free (not counting the numerical error from approximation of the ∇ operator). Physically, this means that the induced electric current paths are closed. In contrast, a divergence-free current is not directly guaranteed by (2.6), since $\nabla \cdot \mathbf{j} = -\nabla \cdot (\sigma \nabla \varphi) + \nabla \cdot (\sigma \mathbf{U} \times \mathbf{B})$, that involves an error associated with the numerical method by which the governing equations were solved. That is why the current paths are not necessarily closed. As mentioned in the previous section, such an error can be quite inappropriate at high Ha especially for non-conducting channel walls.

The equation for $\mathbf{B}^i$ can be derived by applying the curl operator to Ohm's law (2.6) and then substituting the electric field and the current by using Faraday's law (2.5) and Ampère's law (2.13). After some rearrangements the so-called induction equation is obtained

$$\frac{\partial \mathbf{B}^i}{\partial t} = \nabla \cdot (\eta \nabla \mathbf{B}^i) - \nabla(\eta \nabla \cdot \mathbf{B}^i) + \mathbf{S}_B - \frac{\partial \mathbf{B}^0}{\partial t}, \tag{2.14}$$

where $\mathbf{S}_B = \nabla \times (\mathbf{V} \times \mathbf{B}^0) = (\mathbf{B}^0 \cdot \nabla)\mathbf{V} - (\mathbf{V} \cdot \nabla)\mathbf{B}^0$ is the source term. Equation (2.14) is written in a conservative form (the magnetic diffusivity, $\eta = 1/\mu\sigma$, is inside the derivative). A reduced form of (2.14) under the assumption of constant η is also widely used

$$\frac{\partial \mathbf{B}^i}{\partial t} = \eta \nabla^2 \mathbf{B}^i + \mathbf{S}_B - \frac{\partial \mathbf{B}^0}{\partial t}. \tag{2.15}$$

Equation (2.15) is obtained from (2.14) by taking η outside the differential operator and putting the second term on the right hand side of (2.14) equal to zero in accordance with (2.8). In most cases, the applied magnetic field is steady and the last term of equation (2.15) can also be omitted. In this case equations (2.2) and (2.1) are complemented with equations (2.13) and (2.14) (or (2.15)) to get a closed system of equations.

Equation (2.14) can be used in calculations in a "sandwich-type" geometry that includes domains of different electrical conductivity. In doing so, outside the flow domain, $\mathbf{V}$ in the induction equation (2.14) should be set equal to zero. This allows continuous computations through the whole domain providing that the discrete analog of the induction equation assures the conservation properties.

Unlike the electric potential, which has a distribution in a conductor only, the induced magnetic field diffuses from the flow domain far outside creating some distributions in non-conducting or conducting walls and within the outside space. Strictly

speaking, the zero boundary conditions on $\mathbf{B}^i$ should be imposed at "infinity" where it vanishes. However, in practice, the zero boundary conditions can be formulated at some finite distance from the flow domain without a perceptible effect on the velocity field.

When solving an induction equation in the form of (2.14), constraint (2.8) on the magnetic field should be satisfied. Failure to satisfy the divergence-free condition may lead to spurious currents and unphysical flow patterns. Applying the divergence operator to equation (2.14) results in

$$\frac{\partial(\nabla \cdot \mathbf{B}^i)}{\partial t} = 0. \tag{2.16}$$

This means that the initially divergence-free magnetic field retains the same property in time. For a more complete discussion concerning the divergence-free condition for the magnetic field see Brackbill and Barnes (1980) and Smolentsev et al. (2010).

2.4 Formulation based on the induced electric current density: j-formulation

The j-formulation implements the induced electric current density as a variable. This formulation has been recently proposed (Smolentsev et al. 2010) and presents some advantages with respect to other formulations. The governing equations for **j** can be obtained by applying the curl operator to the induction equation (2.14). As before, we assume that the physical properties (η and μ) are constant within the flow domain, and that the condition $Re_m \ll 1$ is also valid. By using standard transformations of the vector analysis, the j-equation in the flow domain was derived in the following form:

$$\frac{\partial \mathbf{j}}{\partial t} = \eta \nabla^2 \mathbf{j} - \eta \nabla(\nabla \cdot \mathbf{j}) + \mathbf{S}_j, \tag{2.17}$$

where the source term, $\mathbf{S}_j$, is given by

$$\mathbf{S}_j = \frac{1}{\mu} \nabla \times \mathbf{S}_B. \tag{2.18}$$

In accordance with the continuity equation for the electric current, the second term on the right hand side of (2.17) can be omitted. However, keeping this term can help to assure $\nabla \cdot \mathbf{j} = 0$ in numerical calculations. Applying the divergence operator to (2.17) gives

$$\frac{\partial(\nabla \cdot \mathbf{j})}{\partial t} = 0. \tag{2.19}$$

Here, equations (2.2), (2.1) and (2.17) form a closed systems of equations for the j-formulation.

Similar to the electric potential, electric current is distributed only within a conducting region that may include liquid and conducting walls. No calculations of $\mathbf{j}$ are needed in the outside space or within a non-conducting wall. In case of a thin conducting wall, the current in the wall is mostly tangential and almost does not vary across the wall thickness. This leads one to use approximate boundary conditions at the boundaries of the flow domain. In doing so, the calculations of the electric current can be reduced to the flow domain only.

To derive the boundary conditions on the electric current density (Smolentsev et al. 2010), let us consider a fragment of the thin solid wall with adjacent liquid. The current generated in the liquid enters the wall through the liquid-wall interface Γ and then turns in the wall in a tangential direction. The continuity equation in this region can be written as

$$\frac{\partial j_n}{\partial n} = -\nabla_\tau \cdot \mathbf{j}_\tau. \tag{2.20}$$

Integrating (2.20) through the wall assuming that the normal component of the current at the outside surface of the wall is zero yields

$$j_n(\Gamma) = -\nabla_\tau \cdot (t_w \mathbf{j}_{\tau w}), \tag{2.21}$$

where $\mathbf{j}_{\tau w}$ is the wall current, which to the leading order of approximation does not vary across the wall. Due to the continuity of the tangential component of the electric field across the interface, we have

$$\frac{\mathbf{j}_\tau(\Gamma)}{\sigma} = \frac{\mathbf{j}_{\tau w}(\Gamma)}{\sigma_w}. \tag{2.22}$$

Substituting $\mathbf{j}_{\tau w}$ from (2.22) into (2.21) and using again the continuity equation for the electric current results in the following boundary condition for the normal component of the current at the wall

$$j_n(\Gamma) = \frac{t_w \sigma_w}{\sigma} \frac{\partial j_n}{\partial n} - \left(\nabla_\tau \frac{t_w \sigma_w}{\sigma} \right) j_\tau(\Gamma), \tag{2.23}$$

or assuming that t_w and σ_w are constant over the wall area

$$j_n(\Gamma) - c_w \frac{\partial j_n(\Gamma)}{\partial n} = 0, \tag{2.24}$$

where $c_w = t_w \sigma_w / \sigma$. This boundary condition is identical in form to that on the induced magnetic field in the thin conducting wall approximation in fully developed

flows (Shercliff 1956). As for the boundary condition on $\mathbf{j}_\tau$, it can be obtained through introducing the wall potential, φ_w, such that

$$\mathbf{j}_{\tau w} = -\sigma_w \nabla_\tau \varphi_w. \tag{2.25}$$

After substitution of (2.25) into (2.21) one can obtain the following second-order partial differential equation for the wall potential

$$j_n(\Gamma) = \nabla_\tau \cdot (t_w \sigma_w \nabla_\tau \varphi_w). \tag{2.26}$$

Provided equation (2.26) is solved over the whole wall area, the electric current in the wall can be calculated using (2.25) and then the distribution of the tangential current at the liquid-wall interface, $\mathbf{j}_\tau(\Gamma)$, can be found using (2.22).

In the special case of non-conducting walls, boundary condition (2.24) is reduced to $j_n = 0$. The tangential current at the wall assuming no-slip velocity condition there, is given by the expression

$$\mathbf{j}_\tau(\Gamma) = -\sigma \nabla_\tau \varphi(\Gamma). \tag{2.27}$$

Combining (2.27) with (2.20) results in the following equation for the potential at the wall

$$\frac{\partial j_n(\Gamma)}{\partial n} = \nabla_\tau \cdot (\sigma \nabla_\tau \varphi(\Gamma)). \tag{2.28}$$

After solving (2.28), the tangential current at the wall is calculated with (2.27).

It is easy to see that the j-formulation is a trade-off between the electric potential and induced magnetic field formulations. Similar to the φ-formulation, the domain of integration is reduced only to the flow region, even though the channel walls are electrically conducting. Similar to the B-formulation, it does not rely on Ohm's law as a way for calculating the electric current in the flow domain. Hence, potentially it can be applied to flows with high Hartmann numbers. Although the formulation uses the electric potential in the wall area, the problem encountered in the φ-formulation in the flow domain does not arise, since Ohm's law in the wall is reduced to $\mathbf{j} = -\sigma \nabla \varphi$. However, the number of equations to be solved in comparison with the B-formulation is increased by one due to the need of computing the wall potential.

Next chapter is focused on the implementation of B- and j-formulations to the flow past a magnetic obstacle. The j-formulation has also been used for the numerical simulation of other important MHD duct flows, obtaining very satisfactory results (Smolentsev et al. 2010). φ-formulation is not implemented in this work although other authors have applied it to simulate, particularly the flow past a magnetic obstacle (Votyakov and Zienicke 2007, Votyakov et al. 2008, Votyakov and Kassinos 2009).

Part of the results in this chapter have been published in

- Smolentsev S., Cuevas S., Beltrán A. (2010). Induced electric current-based formulation in computations of low magnetic Reynolds number magnetohydrodynamic flows. *Journal of Computational Physics*, 229, 1558 - 1572.

Chapter 3

The flow past a magnetic obstacle

In this chapter, we analyze numerically the rectilinear flow past a magnetic obstacle considering both a LM and an electrolyte. Different numerical approaches are used, namely, 2D, Q2D and 3D. First, with a 2D numerical model, the LM flow past a magnetic obstacle is analyzed by implementing the new j-formulation and comparing results with the well-known B-formulation. In addition, the time dependent behavior of the flow is analyzed as the Reynolds and Hartmann numbers are varied, showing a dynamic behavior characteristic of this kind of flows. Then, we implement a Q2D numerical model that considers the friction with the bottom wall in the shallow fluid flow past a magnetic obstacle, in the cases of LM and electrolytic working fluids. Finally, using a parallelized version of the numerical code, 3D results of the shallow flow of an electrolyte in a localized field are presented.

3.1 Background

There is a practical interest to investigate magnetohydrodynamic (MHD) flows that may become unstable and present a time-dependent behavior. In fact, promotion of unsteady inertial flows, in particular time-dependent mixing, is desirable for heat transfer enhancement purposes. In spite of some stabilizing effects of steady magnetic fields, there are several MHD flows at low magnetic Reynolds number that may present unstable behavior. For instance, high velocity side layer flows in rectangular ducts (Reed and Picologlou 1989, Burr et al. 2000), flows past solid obstacles (Mück et al. 2000, Frank et al. 2001), flows in ducts with non-uniform wall conductance (Alpher

et al. 1960, Bühler 1996), electrically driven flows (Hansen et al. 1998, Rothstein et al. 1999), and flows in localized magnetic fields (Honji 1991, Honji and Haraguchi 1995, Afanasyev and Korabel 2006, Cuevas et al. 2006a, Cuevas et al. 2006b), provide examples of the appearance of instabilities in flows of conducting liquids under steady magnetic fields.

In general, an external magnetic field affects the stability of a base flow of an electrically conducting fluid in two opposite ways. In the one hand, there is an *stabilizing effect* produced by two mechanisms: the damping of velocity fluctuations by Joule dissipation and the braking of the flow by the Hartmann effect. The damping of fluctuations manifests the dissipative action of electric currents circulating in the fluid, since kinetic energy is converted into heat via Joule dissipation. In MHD flows, Joule dissipation leads to a more rapid damping of disturbances than in flows where only viscous dissipation prevails. Besides, the circulation of electric currents in boundary layers attached to walls where a normal component of the applied magnetic field exists, creates a Lorentz force that tends to brake the fluid motion (i.e the *Hartmann braking*). Since velocity gradients are increased near the wall, wall friction is also increased, leading to a rise in the drag coefficient. As a matter of fact, the possibility of flow stabilization through the action of a steady magnetic field, is the basis of many technological applications (Davidson 2001).

On the other hand, Lorentz forces may also produce a *destabilizing effect* on the flow by modifying the mean-flow velocity distribution. In fact, the creation of inflection points in the velocity profile is the mechanism by which Lorentz forces may reduce the stability of the flow. There are several examples that show the emergence of instabilities when non-uniformities in the electromagnetic conditions of the flow are present. Non-uniformities, for instance, in the electrical conductivity of the walls or in the strength of the magnetic field, promote the creation of internal shear layers. However, the presence of non-negligible inertial effects is a necessary condition for these layers to become unstable. This is shown very clearly in the paper by Bühler (1996), where, the quasi-two-dimensional flow in a duct with a discontinuity in the electrical conductivity of the walls under a uniform magnetic field, was theoretically analyzed. He showed that inhomogeneity in the wall conductivity may develop an instability that leads to time-dependent solutions similar to the Kármán vortex street behind bluff bodies. In fact, the formation of a Kármán street was also observed experimentally in the shallow flow of mercury in an insulating open channel in which a copper disk much thinner than the fluid depth was mounted on the bottom (Alpher et al. 1960). Non-uniform magnetic fields may also be the source of flow instabilities. Arranges of permanent magnets have long been used to promote mixing and even to get quasi-two-dimensional turbulent regimes by injecting electric currents in thin fluid layers (Hansen et al. 1998, Rothstein et al. 1999). A less studied situation involves the creation of internal shear layers by traveling localized magnetic fields in

quiescent fluids or, equivalently, uniform flows past fixed localized fields. As a matter of fact, flows of this kind exhibit some features similar to those of ordinary flows around solid obstacles but, also very important differences. It has been shown experimentally that vortical flows can be generated by the interaction of the field produced by a traveling permanent magnet, with an electric current applied through a thin layer of an electrolyte (Honji 1991, Honji and Haraguchi 1995, Afanasyev and Korabel 2006). Depending on the velocity of the magnet and the injected electric current, different flow patterns can be generated, including a wavy wake, symmetric vortex pairs and even periodic vortex shedding. On the other hand, the interaction of a uniform LM flow with a localized magnetic field may also produce vortical flows that have been recently explored theoretically and experimentally. The opposition of the generated Lorentz force in these electrolytic or LM flows is what we have called in Chapter 1 a *magnetic obstacle*.

The study of the flow around a solid obstacle, such as a cylinder, is a classical problem in fluid mechanics and has a long history of serious and well documented investigation (Williamson 1996, Zdrakovich 1997). On the other hand, the flow past a magnetic obstacle and, particularly, the structure of the wake of such obstacle, is poorly understood even in the seemingly simple steady state. However, in the past few years this problem has gained considerable attention in the literature (Honji 1991, Honji and Haraguchi 1995, Cuevas et al. 2006a, Cuevas et al. 2006b, Afanasyev and Korabel 2006, Andreev et al. 2006, Thess et al. 2006, Votyakov et al. 2007, 2008, Afanasyev and Korabel 2008 , Kolesnikov et al. 2008, Andreev et al. 2009, Votyakov and Kassinos 2009).

As it was mentioned in Chapter 1, in the LM flow past a magnetic obstacle electric currents induced by the flow in the localized field are sufficiently intense to create a breaking Lorentz force that may substantially alter the motion of the fluid. In turn, in electrolytic flows an injected current (with the proper polarity) is a necessary condition to produce a non-negligible Lorentz force capable of braking the fluid motion and produce vorticity. Each case requires a suitable treatment according to the assumed physical conditions. In both cases, however, owing to the inhomogeneous nature of the localized magnetic field, the Lorentz force is highly non-uniform. It is precisely this feature which gives rise to very rich dynamic behaviors characterized by a variety of flow patterns that, in general, are more complex than those found in the flow past bluff bodies.

3.2 Liquid metal flow past a magnetic obstacle: B- and j-formulation 2D comparison

Since many of the experimental studies of electrolytic and LM flows past magnetic obstacles are carried out in thin fluid layers, we are particularly interested in simulating shallow flows, that is, flows whose characteristic lateral dimensions is large compared with the fluid depth. For these flows, it is common to use a Q2D approach where the friction effects due to the flow-bounding walls are considered through a linear term in the momentum balance equations (see section 3.3). A first approximation to this problem is to neglect this friction force and consider a purely 2D flow. It is worth mentioning that although this appears to be a strong simplification, many fundamental aspects of the flow can be reproduced, at least qualitatively, with a 2D model. Therefore, we now analyze the LM flow past a magnetic obstacle using a 2D numerical model and implementing the j-formulation introduced in Chapter 1. Results are compared with results obtained through the B-formulation.

As previously mentioned, the problem consists of a uniform LM flow, past a strongly localized non-homogeneous magnetic field that occupies only a small fraction of the total flow domain (Figure 3.1). The motion of the fluid through the localized field induces electric currents that interact with the applied magnetic field producing a Lorentz force that opposes the oncoming flow. Originally, this flow was studied numerically using the B-formulation (Cuevas et al. 2006a).

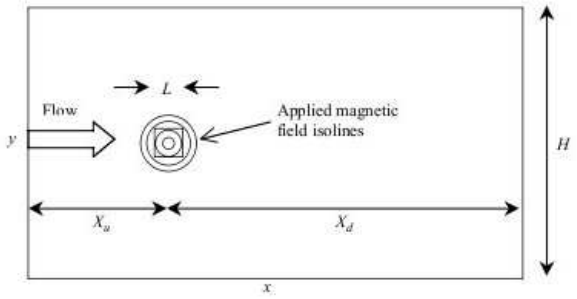

Figure 3.1: Flow configuration and basic geometrical parameters for the flow past a magnetic obstacle.

The localized magnetic field is produced by an externally imposed dipolar field distribution, created by a square magnetized surface uniformly polarized in the normal direction, so that its magnetic moment points in the direction normal to the plane of

motion. Since the dominant contribution of the applied field comes from the component normal to the $\tilde{x}-\tilde{y}$ plane, $\mathcal{B}_z^0$, under the 2D approximation condition, this is the only one considered.

The 3D field created by a rectangular magnetized surface with side lenght L is given analytically in the book by McCaig (1977). In particular, the $\mathcal{B}_z^0(x,y)$ component is expressed in dimensional terms as

$$\begin{aligned}\mathcal{B}_z^0 &= B_{max}\left\{\tan^{-1}\left(\frac{(X+a)(Y+b)}{(Z-Z_0)[(X+a)^2+(Y+b)^2+(Z-Z_0)^2]^{1/2}}\right)\right.\\ &+ \tan^{-1}\left(\frac{(X-a)(Y-b)}{(Z-Z_0)[(X-a)^2+(Y-b)^2+(Z-Z_0)^2]^{1/2}}\right)\\ &- \tan^{-1}\left(\frac{(X+a)(Y-b)}{(Z-Z_0)[(X+a)^2+(Y-b)^2+(Z-Z_0)^2]^{1/2}}\right)\\ &- \left.\tan^{-1}\left(\frac{(X-a)(Y+b)}{(Z-Z_0)[(X-a)^2+(Y+b)^2+(Z-Z_0)^2]^{1/2}}\right)\right\}, \qquad (3.1)\end{aligned}$$

where B_{max} is the maximum magnetic field strength at the geometrical center of the magnetized surface. For the sake of simplicity, we consider that the magnetized surface has a square shape, that is, $2a = 2b = L$, where L is taken as the characteristic length of the flow. Figure 3.2 shows the dimensionless distribution of the normal $B_z^0(x,y)$ component of the field, created by this magnetized square surface.

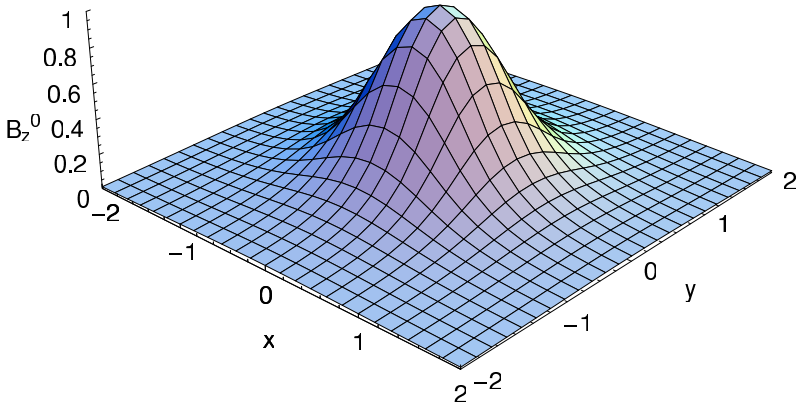

Figure 3.2: Spatial distribution of the dimensionless normal component, $B_z^0(x,y)$, of the applied magnetic field created by a magnetized square surface of unitary side length L.

Here, we solve the problem using both, B- and j-formulation. For the j-formulation,

the dimensionless governing equations (2.2), (2.1) and (2.17) can be expressed in terms of the velocity, pressure and electric current density in the form

$$\frac{\partial \tilde{U}}{\partial \tilde{x}} + \frac{\partial \tilde{V}}{\partial \tilde{y}} = 0, \tag{3.2}$$

$$\frac{\partial \tilde{U}}{\partial \tilde{t}} + \tilde{U}\frac{\partial \tilde{U}}{\partial \tilde{x}} + \tilde{V}\frac{\partial \tilde{U}}{\partial \tilde{y}} = -\frac{\partial \tilde{P}}{\partial \tilde{x}} + \frac{1}{Re}\left(\frac{\partial^2 \tilde{U}}{\partial \tilde{x}^2} + \frac{\partial^2 \tilde{U}}{\partial \tilde{y}^2}\right) + \frac{Ha^2}{Re}\tilde{j}_y \mathcal{B}_z^0, \tag{3.3}$$

$$\frac{\partial \tilde{V}}{\partial \tilde{t}} + \tilde{U}\frac{\partial \tilde{V}}{\partial \tilde{x}} + \tilde{V}\frac{\partial \tilde{V}}{\partial \tilde{y}} = -\frac{\partial \tilde{P}}{\partial \tilde{y}} + \frac{1}{Re}\left(\frac{\partial^2 \tilde{V}}{\partial \tilde{x}^2} + \frac{\partial^2 \tilde{V}}{\partial \tilde{y}^2}\right) - \frac{Ha^2}{Re}\tilde{j}_x \mathcal{B}_z^0, \tag{3.4}$$

$$\frac{\partial \tilde{j}_x}{\partial \tilde{t}} + \frac{\partial^2 \tilde{j}_x}{\partial \tilde{x}^2} + \frac{\partial^2 \tilde{j}_x}{\partial \tilde{y}^2} = \frac{\partial^2}{\partial \tilde{x}\partial \tilde{y}}(\tilde{U}\mathcal{B}_z^0) + \frac{\partial^2}{\partial \tilde{y}^2}(\tilde{V}\mathcal{B}_z^0), \tag{3.5}$$

$$\frac{\partial \tilde{j}_y}{\partial \tilde{t}} + \frac{\partial^2 \tilde{j}_y}{\partial \tilde{x}^2} + \frac{\partial^2 \tilde{j}_y}{\partial \tilde{y}^2} = \frac{\partial^2}{\partial \tilde{x}\partial \tilde{y}}(\tilde{V}\mathcal{B}_z^0) + \frac{\partial^2}{\partial \tilde{x}^2}(\tilde{U}\mathcal{B}_z^0), \tag{3.6}$$

where we use the uniform velocity U_0 as a velocity scale, the side length of the magnetized plate L as a characteristic length scale, the maximum field strength B_{max} as a magnetic field scale, $\sigma U_0 B_{max}$ as a scale for the induced currents, ρU_0^2 for the pressure, while the time t is normalized by L/U_0.

Governing equations for the B-formulation are equations (3.2)-(3.4) and the induction equation (2.15), which in the two-dimensional case and in the quasi-static approximation (Moreau 1990), neglecting $O(Re_m)$ terms reduces to a single equation for the component $\tilde{b}_z$, of the induced magnetic field $\mathbf{B}^i$ (Cuevas et al. 2006a, Beltrán 2006)

$$\nabla_\perp^2 \tilde{b}_z - \tilde{U}\frac{\partial \mathcal{B}_z^0}{\partial \tilde{x}} - \tilde{V}\frac{\partial \mathcal{B}_z^0}{\partial \tilde{y}} = 0, \tag{3.7}$$

where the subindex $\perp$ denotes the projection of the ∇ operator on the $(\tilde{x} - \tilde{y})$-plane. Here the induced magnetic field $\tilde{b}_z$ has been normalized by $Re_m B_{max}$. Once $\tilde{b}_z$ is determined, Ampère's law (2.13) gives an expression to calculate electric currents,

$$\tilde{j}_x = \frac{\partial \tilde{b_z}}{\partial \tilde{y}}, \qquad \tilde{j}_y = -\frac{\partial \tilde{b_z}}{\partial \tilde{x}}. \tag{3.8}$$

Besides, equation (3.8) also guarantees that the electric current density is divergence-free (see equation (2.7)). In the following section we present the numerical method used in this work.

3.2.1 Boundary conditions and numerical implementation

A rectangular domain of 35 $\times$ 20 measured in units of the characteristic length L, is considered. For numerical purposes, the origin was located at the bottom-left corner of the rectangular domain. A uniform flow in the $\tilde{x}$-direction is prescribed at the inlet, namely, $\tilde{U} = 1$, $\tilde{V} = 0$, $\tilde{j}_x = \tilde{j}_x = 0$. The center of the magnetic obstacle, that is the point of maximum magnetic field strength, is located in the midline axis 10 units downstream from the inlet, (so the magnetized surface is located in $9.5 < \tilde{x} < 10.5$ and $9.5 < \tilde{y} < 10.5$). At the outlet, Neumann conditions are used, $\partial\tilde{U}/\partial\tilde{x} = \partial\tilde{V}/\partial\tilde{x} = \partial\tilde{j}_x/\partial\tilde{x} = \partial\tilde{j}_y/\partial\tilde{x} = 0$. At the lateral boundaries, symmetry-type conditions simulating a frictionless wall were imposed, $\partial\tilde{U}/\partial\tilde{y} = \tilde{V} = 0$. Finally, we assume that at the lateral boundaries the induced current components satisfy $\partial\tilde{j}_y/\partial\tilde{y} = \tilde{j}_x = 0$. These conditions on velocities and electric currents are equivalent to assume that lateral walls are sufficiently far from the obstacle region so that they do not influence the flow. For the induced currents j_y and j_x, these are also symmetry-type conditions for the current. In fact, the width of the domain in the $\tilde{y}$-direction is chosen long enough so that the induced current is negligible at lateral boundaries. As initial condition, the fluid was assumed to be at rest.

Finally, for the case of B-formulation, we use the same conditions for the velocity at the inlet, outlet and lateral boundaries as in the j-formulation. In addition, we assume that the induced field is zero at a long enough finite distance from the source of the applied field. Therefore, we impose that the single component of the induced field satisfies the condition

$$\tilde{b_z} \mid_S = 0, \tag{3.9}$$

where the subindex S denotes all the boundaries of the integration domain.

3.2.2 Numerical method

The solution to the set of equations (3.2)-(3.6) is obtained with a numerical method based on the primitive variables, the velocity and pressure, and the induced electric currents or the induced magnetic field as the electromagnetic variable. A finite difference projection method on an orthogonal equidistant grid in a rectangular domain was used to solve the governing equations under suitable boundary conditions, assuming a motionless fluid as initial condition. The standard time-marching procedure described in Griebel et al. (1998) was extended to consider MHD flows.

A spatial discretization of second-order accuracy was done on a staggered grid arrangement while the Euler method was used for time discretization. Accurate time integration was provided by choosing a small enough time step. The velocity components $\tilde{U}$ and $\tilde{V}$ were defined at the midpoints of the vertical and horizontal surfaces of

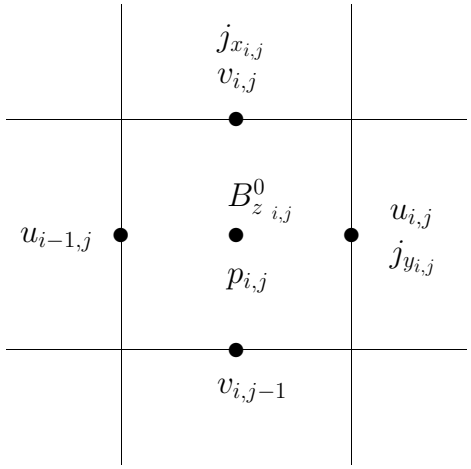

Figure 3.3: Computational cell used in the computations.

the computational cell, respectively. The induced currents j_y and j_x are defined at the same location as velocity components, while the pressure, the induced and the applied magnetic field were defined at the center of the cell (see Figure 3.3). Diffusive terms were discretized using central differences. For convective terms a mixture of central differences and the donor-cell discretization was used.

The time discretization of the momentum equations (3.3) and (3.4) is given in the form

$$\begin{aligned} \tilde{U}^{(n+1)} &= F^n - \delta t \frac{\partial \tilde{P}^{(n+1)}}{\partial \tilde{x}} \\ \tilde{V}^{(n+1)} &= G^n - \delta t \frac{\partial \tilde{P}^{(n+1)}}{\partial \tilde{y}} \end{aligned} \tag{3.10}$$

We evaluate F and G at a time level n, where

$$\begin{aligned} F^n &= \tilde{U}^{(n)} + \delta t \left[\frac{1}{Re} \nabla^2_{\perp} \tilde{U} - \frac{\partial \left(\tilde{U}^2 \right)}{\partial \tilde{x}} - \frac{\partial \left(\tilde{U}\tilde{V} \right)}{\partial \tilde{y}} + \frac{Ha^2}{Re} \tilde{j}_y \mathcal{B}^0_z \right] \\ G^n &= \tilde{V}^{(n)} + \delta t \left[\frac{1}{Re} \nabla^2_{\perp} \tilde{V} - \frac{\partial \left(\tilde{V}^2 \right)}{\partial \tilde{y}} - \frac{\partial \left(\tilde{U}\tilde{V} \right)}{\partial \tilde{x}} - \frac{Ha^2}{Re} \tilde{j}_x \mathcal{B}^0_z \right] \end{aligned} \tag{3.11}$$

All velocities in equation (3.11) belong to time level t_n, while the pressure gradient values in (3.10) are associated with time level $t_{(n+1)}$

If we substitute equation (3.10) into the continuity equation (3.2), we obtain (after rearranging) a Poisson equation for the pressure P:

$$\frac{\partial^2 \tilde{P}^{(n+1)}}{\partial \tilde{x}^2} + \frac{\partial^2 \tilde{P}^{(n+1)}}{\partial \tilde{y}^2} = \frac{1}{\delta t}\left(\frac{\partial F^{(n)}}{\partial \tilde{x}} + \frac{\partial G^{(n)}}{\partial \tilde{y}}\right) \tag{3.12}$$

As we can see from equations (3.10) and (3.12), the time discretization of the momentum equations was explicit in the velocities and implicit in the pressure.

The Poisson equation for the pressure was solved subject to homogeneous Neumann conditions on the boundary, simulating far-field conditions commonly used in the analysis of flows past solid obstacles in unbounded regions. The Gauss-Seidel method was used for the solution of the pressure Poisson equation (3.12), which was iterated until the divergence of the velocity field reached values of the order of 10^{-6}. Equations for the induced electric current density (3.5) and (3.6), as well as, equation(3.7) for the induced magnetic field $\tilde{b}_z$ were solved at $t_{(n+1)}$ using the same method.

3.2.3 Preliminary description of the flow

We offer here an introductory qualitative description of the phenomena involved in the flow past a magnetic obstacle (Cuevas et al. 2006a; Beltrán 2006). This flow has some resemblance with the duct flow at the entrance/exit of a magnet (Müller and Bühler 2001, Moreau 1990), though the size of the obstacle and the absence of lateral (side) walls change the flow structure strongly. The fluid passing through the magnetic obstacle encounters mainly four different regions of fringing magnetic field. The lateral fringing regions have a secondary effect on the flow in most cases while inlet and outlet fringing regions are always of primary importance. In a short distance (on the order of the characteristic length of the obstacle), the oncoming fluid passes from a region of nearly zero magnetic field to one with $O(1)$ strength, and then again to a region of negligible field. Different flow regimes can be observed depending on the values of the Reynolds and Hartmann numbers. For the Reynolds numbers explored in this study, stationary as well as periodic solutions were found depending on the value of Ha.

In the neighborhood of the inlet fringing zone the oncoming fluid passes from a region of low-intensity field to one with a high intensity. The electromotive force $\mathbf{U} \times \mathbf{B}^0$ induces a lower voltage in the low-intensity region and a higher voltage in the region where the field is stronger. If we place the origin in the center of the magnetized surface, the voltage difference drives a current in the flow direction for $y > 0$ and in the opposite direction for $y < 0$. These currents close in the cross-stream direction upstream and downstream of the inlet fringing zone. When the fluid moves through the outlet fringing zone, the voltage difference is inverted, as

is the current circulation. Therefore, upstream of the obstacle, currents circulate clockwise and produce an induced magnetic field in the normal direction that points downwards, in accordance with Lenz's law. Downstream of the obstacle, the current circulation is anti-clockwise and the induced magnetic field points upwards. Under certain conditions, only these two main current loops are formed. However, additional current loops may appear. The number and particular structure of current loops depend on both Reynolds and Hartmann numbers (Cuevas et al. 2006b).

In the duct flow at the entrance or exit of a magnet, the sidewalls confine the current loops in such a way that they are elongated in the flow direction, intensifying the streamwise current density components. This is of particular importance when the sidewalls are electrically insulated. The current density components in the streamwise direction give rise to Lorentz forces that point towards the sidewalls. This provokes the expulsion of the volumetric flow from the core towards the side layers with high velocities and, therefore, an M-shape velocity profile is created (Müller and Bühler 2001, Moreau 1990). In contrast, in the flow past a magnetic obstacle where sidewalls are absent, current loops tend to spread in the flow domain. In the region of high-intensity field, currents close through the lateral fringing zones and, consequently, cross-stream current density components are dominant. In fact, in this region electric currents from the upstream and downstream loops reinforce flowing in the negative direction, transverse to the main flow. The current density interacts with the magnetic obstacle field giving rise to a non-uniform Lorentz force that points mainly in the streamwise direction, opposing the flow and creating vorticity. This causes a pressure increase in the neighborhood upstream of the obstacle, while downstream it drops abruptly. As can be seen in Cuevas et al. (2006a), for $Re = 100$ and a small Hartmann number ($Ha \approx 1 - 10$), the fluid moves with reduced velocity through the high-intensity field region. As the Hartmann number increases and the opposing Lorentz force is stronger, the oncoming fluid tends to flow around the obstacle and a noticeable cross-stream velocity component appears. The flow past a magnetic obstacle displays some of the characteristic regions observed in the flow around a cylinder, namely a region of retarded flow upstream of the obstacle, two sidewise regions of displaced and accelerated flow, and a wake downstream of the obstacle (Zdrakovich 1997, Oertel 1990). In the neighborhood of the lateral fringing zones, the velocity is higher than near the central region where the opposing force is more intense. This leads to a velocity deficit in the central region, and the creation of two lateral free-shear layers parallel and aligned with the main flow direction where a maximum and a minimum of vorticity exist. When the Re number is small ($Re = 10$) and Hartmann number is about 11.5 the fluid may become stagnant in the region of intense field, while far away from the obstacle the flow remains nearly unperturbed, (Figure 3.4a). If the Hartmann number is sufficiently high ($Ha \approx 15$), vortices can appear in the near wake, (Figure 3.4b). These vortices, although created by Lorentz forces, are formed

and evolve inside a negligible magnetic field. When convective effects and the magnetic braking are strong enough, the wake can become destabilized and present unsteady behavior. In fact, a periodic vortex shedding similar to the von Kármán street in the flow around a cylinder, can be observed (Figure 3.4c). The previous discussion is valid when the constrainment factor $\kappa = L_y/H$, where L_y is the length of the magnet in the transversal $\tilde{y}$-direction and H is the separation between the lateral boundaries, is small ($\kappa \lesssim 0.2$; Votyakov and Zienicke 2007). When $\kappa \approx 0.4$ a steady flow pattern of six vortices appears, as will be discussed on section 3.3.1.

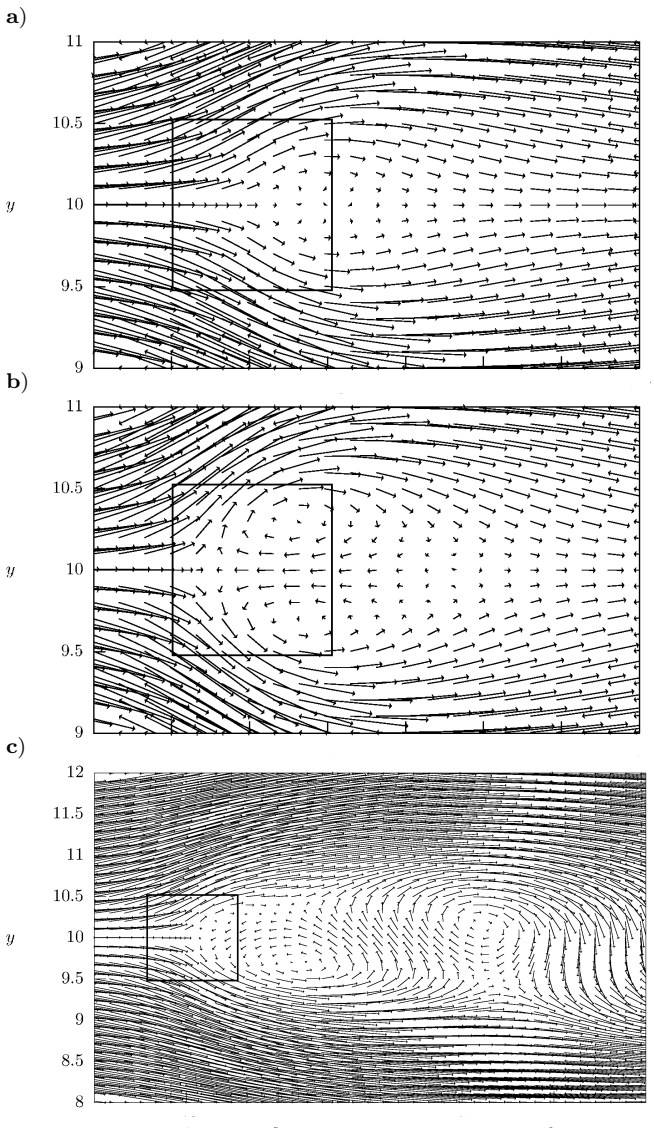

Figure 3.4: Different flow patterns for the magnetic obstacle problem. (a) streamlined flow for $Re = 10$ and $Ha = 11.5$, (b) vortices for $Re = 10$ and $Ha = 15$ and c) vortex shedding for $Re = 100$ and $Ha = 27$

3.2.4 Numerical results

As it was previously mentioned, depending on the governing parameters Re and Ha, that determine inertial and magnetic braking effects, the flow can display steady patterns with or without vortices or a wavy wake and even a periodic vortex shedding. For particular sets of Re and Ha, results computed with the new formulation based on the induced electric current are compared with those using the B-formulation (Cuevas et al. 2006a) that utilizes the same mesh and time increment. Figure 3.5a shows the induced magnetic field isolines in the neighborhood of the magnetic obstacle, calculated with the B-formulation for the case $Re = 100$ and $Ha = 50$. The isolines correspond to the current paths since the induced field serves as a stream function for the current density (see equations (3.8)). In turn, Figure 3.5b shows the corresponding current density field calculated with the j-formulation. The current distribution displayed in both figures match very well.

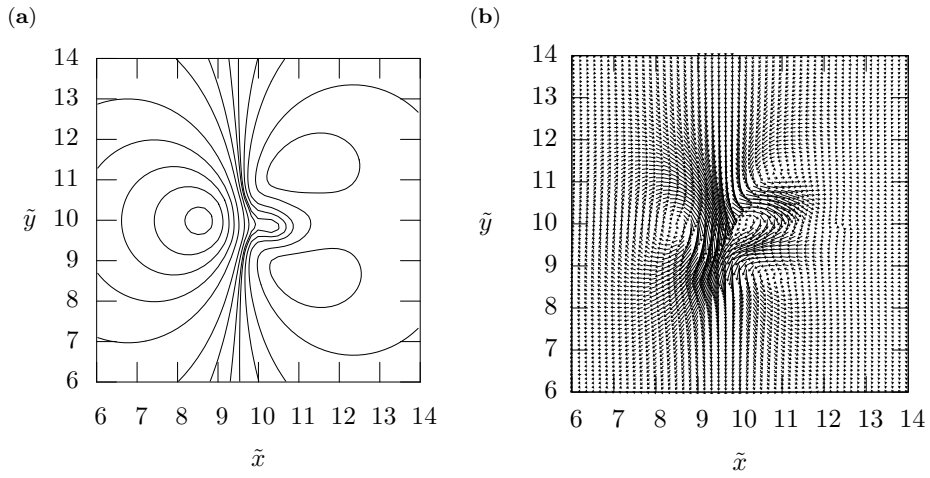

Figure 3.5: Comparison between two formulations for the flow past a magnetic obstacle. (a) Induced magnetic field isolines calculated with B-formulation. (b) Induced current density field calculated with j-formulation. $Re = 100$ and $Ha = 50$.

For the previous parameter values, the wake of the magnetic obstacle presents a periodic vortex shedding so that a von Kármán street is formed, as clearly observed in Figures 3.6a and 3.6b where the vorticity isolines calculated with the B- and j formulation, respectively, are shown in the flow domain. Note that the comparison is also very good.

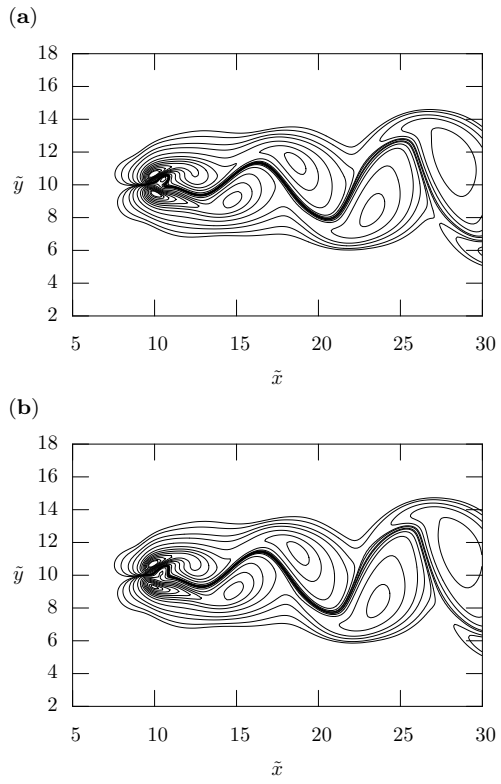

Figure 3.6: Vorticity isolines in the flow past a magnetic obstacle for $Re = 100$ and $Ha = 50$. (a) Calculated with B-formulation. (b) Calculated with j-formulation.

Figure 3.7a shows the comparison for velocity component $\tilde{U}$ as a function of the axial coordinate for a steady flow ($Re = 100$, $Ha = 10$), while Figure 3.7b presents the same comparison for a time-dependent flow ($Re = 100$, $Ha = 50$). Figures 3.7c and 3.7d show, respectively, the current component $\tilde{j}_x$ in the axial direction and the vorticity as a function of time for the same unsteady case at $Re = 100$ and $Ha = 50$. Note that the component $\tilde{j}_x$ displays a very regular behavior that incidentally is very similar to the one found in the steady flow. On the other hand, the variation of vorticity with time clearly reflects the periodic behavior of the flow. However, it should be mentioned, that transient states are slightly different for each formulation. In fact, the j-formulation reaches a steady state faster than the B-formulation. In general, it can be observed that even in a time-dependent flow, computations performed with both formulations are in a fair agreement. A good match between results computed with the two formulations for unsteady flows is also seen in Figure 3.8 where a global parameter, namely, the dimensionless frequency associated with vortex shedding in

the wake, (the Strouhal number) is shown. The Strouhal number is defined as $St = fL/U_0$, where f is the frequency of vortex shedding. In Figure 3.8, St is computed for two Reynolds numbers as a function of Ha. Although the results are close, the j-formulation gives slightly lower frequencies compared to the other one. This might be related to differences in approximation of equations (3.5)-(3.6) for the electric current and the induction equation in the B-formulation.

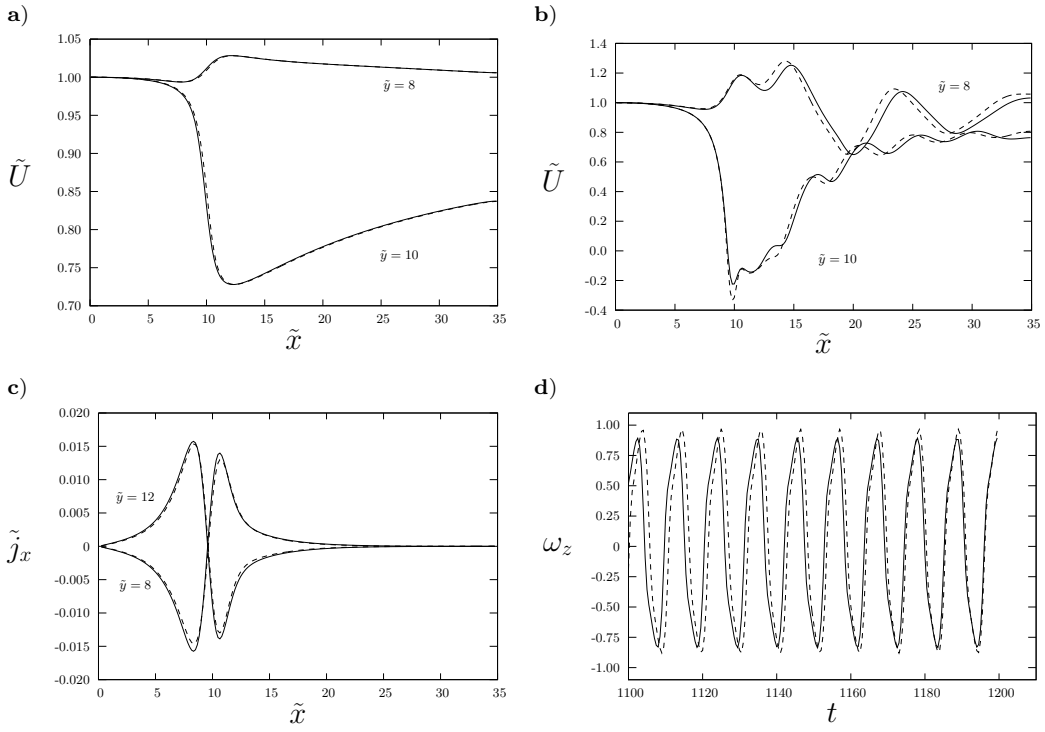

Figure 3.7: Comparison between two formulations for the flow past a magnetic obstacle. B-formulation: continuous line; j-formulation: dotted line. (a) Velocity component in steady flow at $Re = 100$ and $Ha = 10$. (b) Axial velocity component in unsteady flow at $Re = 100$ and $Ha = 50$. (c) Axial induced current in unsteady flow at $Re = 100$ and $Ha = 50$. (d) Vorticity as a function of time at $\tilde{x} = 15$, $\tilde{y} = 0$ for $Re = 100$ and $Ha = 50$.

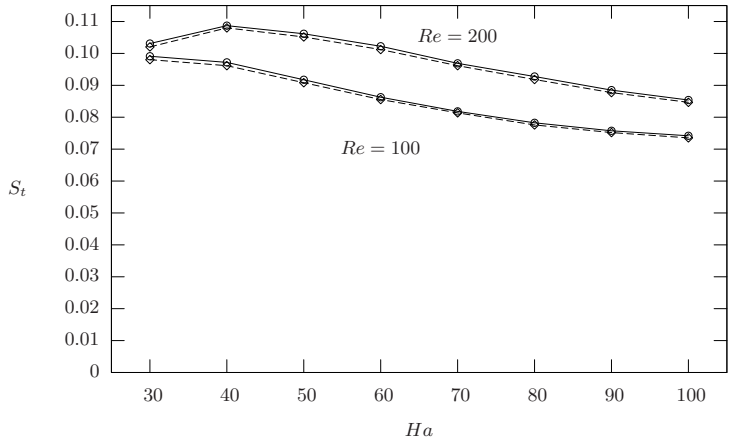

Figure 3.8: Strouhal number versus Hartmann number computed with two formulations. B-formulation: continuous line. j-formulation: dotted line.

Previous results show that the j-formulation can be used in computations of steady and time-dependent MHD flows as well as the classical B-formulation, demonstrating very good agreement. As discussed in chapter 2, the new suggested formulation does not require computations of the electric potential in the flow region but an additional equation for the wall potential has to be solved at the liquid-solid interface to compute the tangential component of the induced current at the interface. The wall-normal current component at the interface is described with the Robin boundary condition. In this way, the derived equation for the induced electric current, the boundary conditions for the tangential and wall-normal current components along with the flow equations and proper conditions on the velocity components form a closed problem.

Compared to the traditional φ- and B-formulation, the new one introduces some advantages. First of wall, it does not rely on Ohm's law for computing the induced electric current in the flow domain and thus is free from the potential numerical error that may result in electric current discontinuity, which is often observed in high Hartmann number computations when the φ- formulation is used. Second, it does not require computations in the wall and in the outer space as needed when the B-formulation is used for 3-D flows. The disadvantage compared to the φ-formulation is the need to solve three (in 3-D flows) or two (in 2-D flows) equations for the current components compared to only one for the electric potential. Compared to the B-formulation, extra computational time may be needed due to additional computations associated with the wall potential. However, total benefits of the new formulation will depend on a concrete physical problem and can be affected by many parameters, including the flow geometry, wall conductivity, applied magnetic field distribution, etc.

In addition to the flow discussed here, a number of examples of MHD duct flows have been studied to illustrate the implementation of the new formulation (Smolentsev et al. 2010) and also to test several standard numerical techniques in combination with the newly-derived equations for the induced electric current and thin conducting wall boundary conditions. In spite of many potential advantages, the present approach and especially the associated numerical codes have similar limitations as analogous non-MHD codes. For example, increasing Re significantly in calculations of unsteady or developing flows may cause unphysical oscillations presumably related to the limit on the schematic Reynolds number. Nevertheless the ways of mitigating such problems are well described in the specialized literature (see, e.g. Tannehill et al. 1997). No limitation has been determined on the Hartmann number providing a special care is taken on accurate resolution of the Hartmann and side layers. Also, we have not observed any violation of the charge conservation law $\nabla \cdot \mathbf{j} = 0$ as directly seen from the induced electric current distributions, where all induced currents are closed within the integration domain. Although $\nabla \cdot \mathbf{j} = 0$ is not satisfied precisely in the computations, the discrepancy is always within the usual computational errors, which can easily be controlled by changing the computational mesh or increasing the approximation order of the numerical schemes. If necessary, for essentially three-dimensional flows, cleaning procedures to ensure $\nabla \cdot \mathbf{j} = 0$ can also be added in analogy with the B-formulation.

3.2.5 Some dynamic properties of a magnetic obstacle

As we previously discussed, when a localized magnetic field is in relative motion with an electrically conducting fluid (a liquid metal), electric currents are induced that in turn produce a spatially localized Lorentz force oriented in the direction anti-parallel to the relative motion. When the interaction between the induced Lorentz force and the external flow is strong enough, it generates two hyperbolic critical points aligned with the flow direction. Also, two elliptic critical points appear, aligned in a direction perpendicular to flow direction. This can be clearly observed in Figure 3.4b. This geometrical distribution of critical points coincide with that of a flow past a blunt body where front and trailing stagnant points (topologically equivalent to hyperbolic points), aligned with the direction of the flow, are formed. The stability of the resulting flow and the corresponding vortex shedding depends on two effects. First, on the magnitude of the induced Lorentz force and second, on the stability of the elongated vortices that are formed around the elliptic critical points, due to convection. It is important to notice that the previously described flow configuration is one of the possible scenarios since, as it is discussed in section 3.3.1 a steady six-vortex flow pattern can also arise under specific conditions.

In the present section, we describe some dynamic properties of a LM flow past a magnetic obstacle in terms of the Hartmann and Reynolds numbers of the im-

posed flow. For these calculations, we have used the B-formulation although φ- or j-formulation can also be used. Specifically, we analyze the stability of the flow in the (Re, Ha) parametric space, and show that the Hartmann number is related to the " rigidity " of the magnetic obstacle. We find that even though for a given Hartmann number the steady flow may be unstable, when a critical Reynolds number is reached, a further increase in Reynolds number, may result in the flow becoming steady again. Evidently, this behavior is not observed in the flow past a rigid obstacle, as can be seen in the sketch of Figure 3.9. In this case, the flow goes from a steady laminar flow with no vortices for low Reynolds numbers to a turbulent wake for high Re. Thus, the increase of Re leads to stronger destabilization.

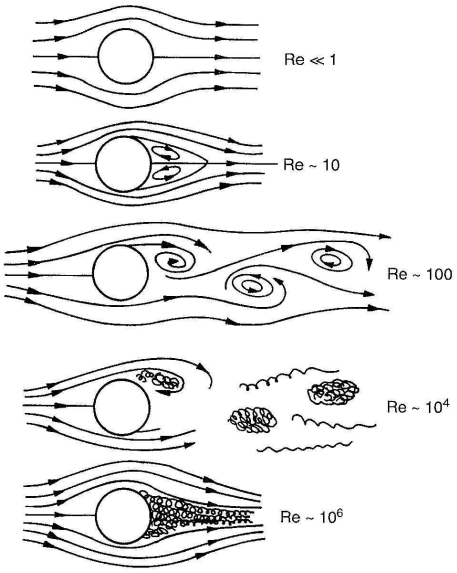

Figure 3.9: Flow past a cylinder as the Reynolds number is increased (Davidson 2001).

In the flow past a solid obstacle the dynamic behavior is determined only by the action of inertial and viscous forces whose effects are described by a single governing parameter, the Reynolds number. In contrast, in the LM flow past a magnetic obstacle, in addition to inertial and viscous forces, magnetic forces are also presented. It is the interplay of these forces, characterized by the Reynolds and Hartmann numbers, which determine the flow dynamics. The existence of an additional governing parameter enlarges the possibilities of dynamic behavior and leads to richer flow patterns.

The evolution of the flow generated by the interaction of a localized magnetic field and the oncoming LM flow as the Reynolds number is increased from 10 to 230 and keeping the Hartmann number fixed at 26, is illustrated in Figure 3.10. The instantaneous streamtracers for a given Re and the corresponding plot of vorticity as a function of time at $\tilde{x} = 5$ and $\tilde{y} = 0$, are shown, on the left and right columns, respectively. The same flow configuration and boundary conditions from section 3.2.4, were used but now, the origin of coordinates is located in the geometrical center of the magnetized surface. For small Reynolds numbers ($Re < 35$), the inertia of the fluid and the magnetic force are not enough to destabilize the flow and the pattern consist of two steady vortices attached to the zone where the magnetic field is intense. Observe from Figure 3.10a that parcels of fluid get trapped in these recirculating regions but, the vorticity at the test point does not present a time variation. If the Reynolds number is increased past a threshold of approximately 38, the induced currents generate a strong enough Lorentz force oriented in a direction opposite to the main flow, the vortex bubbles get elongated and broken by the drag exerted by the main flow and periodic shedding of alternate vortices ensues after a rather long transient state (see Figure 3.10b). In the interval $38 < Re < 70$, the magnetic obstacle generates and sheds vortices with increasing larger vorticity. In fact, as Re increases within this range, the time elapsed for the appearance of vortex shedding is reduced. However, flows with $70 < Re < 230$ display the opposite trend, i.e. the intensity of vorticity reduces with an increasing Reynolds number. At $Re \sim 200$, the flow ceases to display vortical structures, although vorticity in the flow is not negligible, as can be appreciated from Figure 3.10d. Eventually, at $Re \sim 230$, the stream traces are practically rectilinear, with almost no influence of the magnetic field on the motion of the fluid. The occurrence of this phenomenon is in sharp contrast to the corresponding observations of vortex shedding by a rigid obstacle where an increase of the Reynolds number leads to ever more complex flow. In all cases studied, we start the integration considering a motionless fluid, and we have observed that in the cases where vortices are emitted, the vortex shedding start after a time interval (kick-off time) whose duration depends on Re.

In analogy to the case of a rigid obstacle, the vortex shedding non-dimensional frequency (Strouhal number, St), is an increasing function of the Reynolds number in the interval $38 < Re < 100$, but in the interval $100 < Re < 150$, the frequency of vortex shedding as a function of the Reynolds number, displays a small decrease. At Reynolds number 100, we obtained the maximum Strouhal number of 0.098.

A similar phenomenon to that described in the previous paragraphs can be observed when the calculation is made using different Hartmann numbers, as illustrated in Figure 3.11 where the stability (Re, Ha) map is shown. It is found that for small enough Hartmann numbers ($Ha < 20$), the magnetic obstacle is too weak to trigger vortex shedding, regardless of the Reynolds number. However, for larger Hartmann numbers,

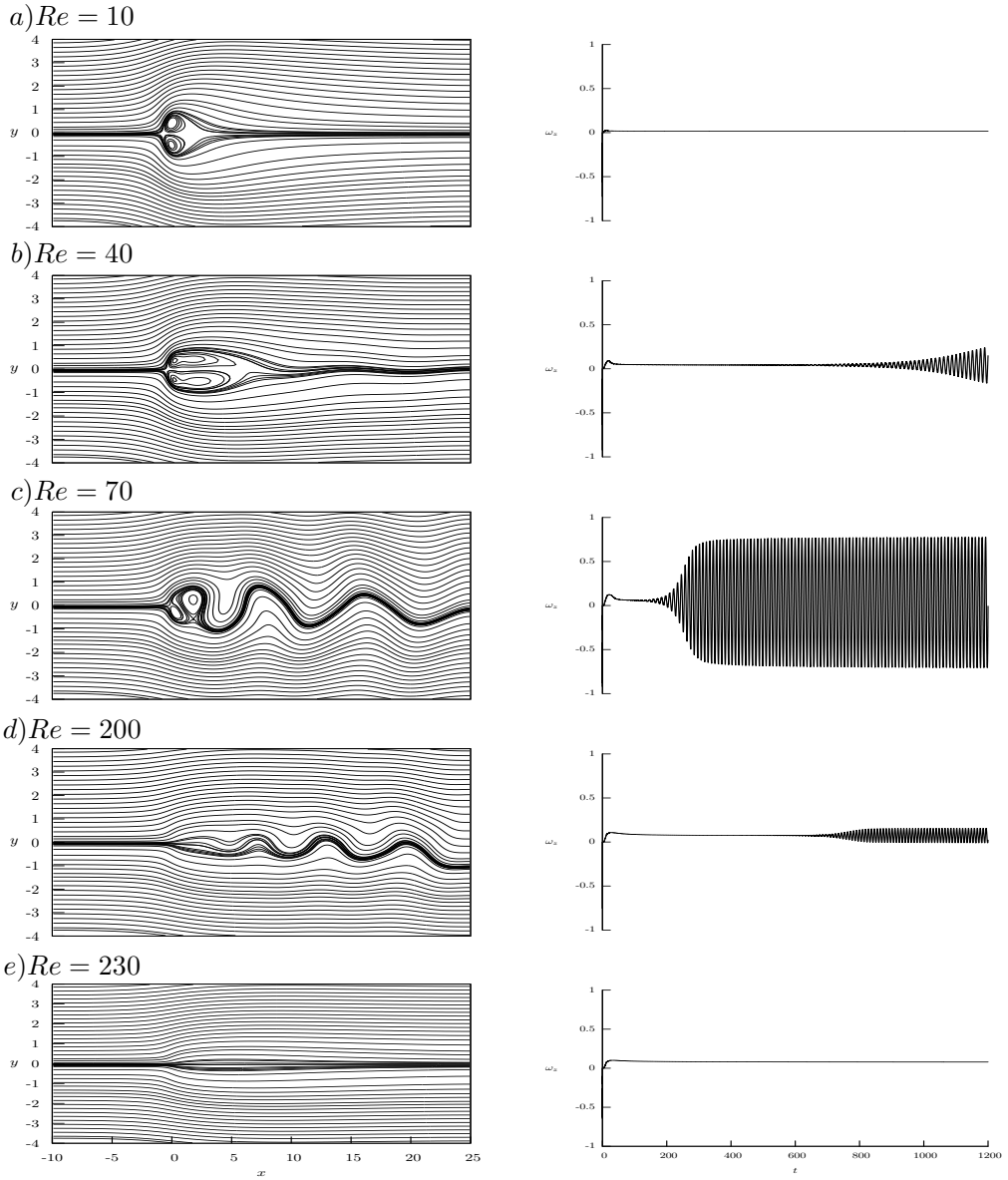

Figure 3.10: Left column: Instantaneous stream traces for five flows with Reynolds numbers from 10 to 230. Right column: Vorticity as function of time at the point $(\tilde{x} = 5, \tilde{y} = 0)$ for the cases illustrated in the left column. In all cases, $Ha = 26$.

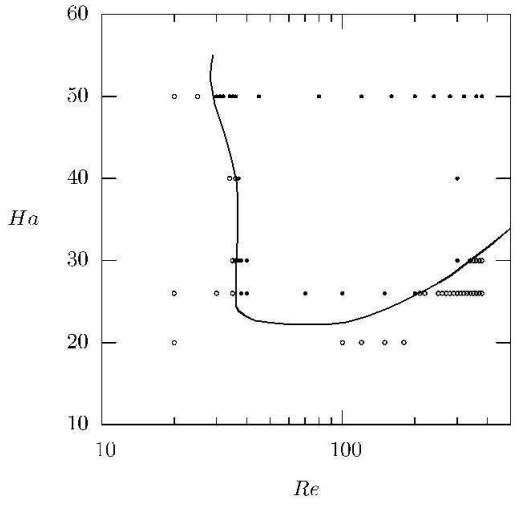

Figure 3.11: (Re, Ha) map of stability. Open circles denote steady flow; black circles represent flows with vortex shedding. The continuous line is the interpolation for neutral stability.

critical Reynolds number for vortex shedding can be clearly identificable. In all cases explored, the start of vortex emission occurs at Reynolds numbers around 40, but the critical Reynolds numbers for the suppression of vortex emission depends strongly on the Hartmann number. For Hartmann number 50, no steady flow was found for Reynolds numbers as large as 350.

The qualitative interpretation of previous results can be given in terms of the acting forces. When both Re and Ha are small, inertia and magnetic forces are too weak, while viscous forces are dominant, leading to a steady laminar flow. In fact, if Re is kept very small and Ha reaches higher values, the stronger magnetic force may lead to more complex flow patterns, for instance, four steady vortices (Cuevas et al. 2006b). For a given Re, the magnetic force will act as an obstacle for the flow provided that the Hartmann number is sufficiently high. If that is the case, an increase of Re may desestabilize the flow, indicating the competing effects of inertia and magnetic forces. If Re is increased even further, inertia may overcome the magnetic force, diminishing its obstacle character. Beyond a specific threshold for Re that depends on the Ha value, the magnetic obstacle is completely *transparent* for the flow, that is, remains unperturbed by the presence of the localized field.

3.3 Quasi-two dimensional approach

Let us now consider a Q2D approach to model the uniform shallow flow of an electrically conducting incompressible viscous fluid, past a strongly localized non-homogeneous magnetic field. The flow configuration is essentially the same considered in section 3.2 (see Figure 3.1), but now it is explicitly assumed that the flow is bounded in the normal $\tilde{z}$-direction, at the bottom, by an insulating rigid wall and, at the top, by a free surface. Also, the magnetized surface that produces the localized field is assumed to be embedded in the bottom wall. The Q2D model involves an averaging procedure of the governing equations in the thin fluid layer that results in the consideration of friction effects due to the existence of the bottom wall. We formulate the model in a generalized form so that it can be applied, with the proper assumptions, to the two physical cases of interest. In the first one, the fluid layer is free from externally injected electric currents, therefore, only induced currents are present, as occurs in the case involving a thin layer of liquid metal. In the second case, an external direct electric current is injected to the fluid layer, transversely to the main flow direction, a common situation when dealing with a thin layer of electrolyte. As previously discussed, the Lorentz force created by the interaction of the electric currents (induced currents for the first case and injected for the second) with the non-uniform magnetic field act as an obstacle for the flow and creates vorticity. In the generalized situation it will be assumed that both induced and injected currents are present.

The main assumption of the Q2D model is that the transport of momentum in the normal direction is mainly diffusive so that the velocity components can be expressed in the form

$$U(\tilde{x},\tilde{y},\tilde{z},t)=\tilde{U}(\tilde{x},\tilde{y},t)\overline{f}(\tilde{x},\tilde{y},\tilde{z}),\quad V(\tilde{x},\tilde{y},\tilde{z},t)=\tilde{V}(\tilde{x},\tilde{y},t)\overline{f}(\tilde{x},\tilde{y},\tilde{z}),\qquad (3.13)$$

where $\tilde{U}$ and $\tilde{V}$ are the averaged velocity components in the $\tilde{x}$ and $\tilde{y}$ directions, respectively. Coordinates $\tilde{x}$ and $\tilde{y}$, are normalized by L, $\tilde{z}$ by h, velocities $\tilde{U}$ and $\tilde{V}$ by the uniform entrance velocity , U_0, and time by L/U_0. The function $\overline{f}$ considers the variation of the velocity profile in the $\tilde{z}$-direction and must satisfy the normalization condition $\int_0^1 f d\tilde{z}=1$. Its dependence on $\tilde{x}$ and $\tilde{y}$ coordinates must reflect the different flow regions due to the localization of the magnetic field.

We will again consider only the dominant normal magnetic field component B_z^0. Since the localized field produced by the magnetized surface in the bottom wall decays through the fluid layer, we consider a field dependence on the normal coordinate that can be approximated in the form

$$B_z^0(\tilde{x},\tilde{y},\tilde{z})=\mathcal{B}_z^0(\tilde{x},\tilde{y})\ g(\tilde{z}),\qquad (3.14)$$

where the function $g(\tilde{z})$ accounts for the field decay in the fluid layer.

The geometrical confinement imposed by the shallow layer restricts three-dimensional perturbations in the normal direction. In shallow flows, the role of bottom friction is of fundamental importance since it promotes a vertical diffusion, associated with the exponential damping of the flow. The bottom friction is determined through the function $\overline{f}$ which can be obtained from a balance between viscous and Lorentz forces generated by both injected and induced currents. Since the applied Lorentz force points in the negative $\tilde{y}$-direction and is maximum at the geometrical center of the magnet, we establish the balance at the central $\tilde{y}-\tilde{z}$ plane ($\tilde{x}=0$). Then, f must satisfy the equation

$$\frac{d^2 f}{d\tilde{z}^2} - (Ha\ \mathcal{B}_z^0(\tilde{x},\tilde{y})\ g)^2 f = \varepsilon^2\ Q\ Re\ \mathcal{B}_z^0(\tilde{x},\tilde{y})\ g \tag{3.15}$$

where $\varepsilon = h/L$ is the aspect ratio or dimensionless layer thickness. The new dimensionless parameter $Q = J_0 B_{max} L/\rho U_0^2$, is the ratio of a magnetic pressure drop due to the applied Lorentz force and the free-stream dynamic pressure, where J_0 is the magnitude of the injected current density. In the paper by Honji and Haraguchi (1995) this parameter is referred as the reduced Lorentz force.

In equation (3.15) the function f has still to be normalized. The terms on the left-hand side correspond to the viscous and induced Lorentz forces while the term on the right-hand side is the applied Lorentz force. The function f must satisfy non-slip conditions at the bottom wall ($f(\tilde{z}=0)=0$), and stress free condition at the free surface ($df(\tilde{z}=1)/d\tilde{z}=0$).

Once $\overline{f}$ is determined, we substitute the assumption (3.13) into the governing MHD equations and integrate in the normal direction from the bottom wall to the free surface. The dimensionless averaged equations of motion take the form

$$\frac{\partial \tilde{U}}{\partial \tilde{x}} + \frac{\partial \tilde{V}}{\partial \tilde{y}} = 0, \tag{3.16}$$

$$\frac{\partial \tilde{U}}{\partial t} + \left(\tilde{U}\frac{\partial \tilde{U}}{\partial \tilde{x}} + \tilde{V}\frac{\partial \tilde{U}}{\partial \tilde{y}}\right) K = -\frac{\partial \tilde{P}}{\partial \tilde{x}} + \frac{1}{Re}\nabla_\perp^2 \tilde{U} + \frac{\tilde{U}}{\tau} + \frac{Ha^2}{Re}\tilde{j}_y \mathcal{B}_z^0 - Q\ \mathcal{B}_z^0, \tag{3.17}$$

$$\frac{\partial \tilde{V}}{\partial t} + \left(\tilde{U}\frac{\partial \tilde{V}}{\partial \tilde{x}} + \tilde{V}\frac{\partial \tilde{V}}{\partial \tilde{y}}\right) K = -\frac{\partial \tilde{P}}{\partial \tilde{y}} + \frac{1}{Re}\nabla_\perp^2 \tilde{V} + \frac{\tilde{V}}{\tau} - \frac{Ha^2}{Re}\tilde{j}_x \mathcal{B}_z^0, \tag{3.18}$$

where the induced current density components $\tilde{j}_x$ and $\tilde{j}_y$ are normalized by J_0.

The factor K in the convective terms in equations (3.17) and (3.18) stands for the integral $\int_0^\varepsilon \overline{f}^2 d\tilde{z}$. In turn, the third term in the right-hand-side (RHS) of these

equations represents the Hartmann-Rayleigh friction (Cuevas et al. 2006a) due to the existence of boundary layers attached to the bottom wall. It involves a characteristic dimensionless timescale, τ, for the decay of vorticity due to dissipation in the Hartmann and viscous layers. The inverse of this timescale is given by $\tau^{-1} = (1/\varepsilon^2\ Re)d\overline{f}/d\tilde{z}|_0^1$. The forth term in the RHS of equations (3.17) and (3.18) corresponds to the $\tilde{x}$- and $\tilde{y}$-component respectively, of the induced Lorentz force. Finally, the fifth term in the RHS of equation (3.17) denotes the applied Lorentz force due to the injected current.

In order to close the system of equations (3.16)- (3.18), we have to consider the induction equation (3.7) and Ampère's law (3.8). Once we solve equation (3.15), we will be able to calculate τ^{-1} and K

3.3.1 Q2D Liquid metal flow past a magnetic obstacle

We now apply the Q2D model presented in the former section to the LM shallow flow past a magnetic obstacle. We are particularly interested in reproducing experimental flow patterns recently observed at the University of Ilmenau, which are described below. As it was already explained, in this case induced currents are strong enough to generate a non-negligible Lorentz force that opposses the oncoming fluid without any injected current, therefore, $Q = 0$. The dimensionless averaged equations of motion take the form

$$\frac{\partial \tilde{U}}{\partial \tilde{x}} + \frac{\partial \tilde{V}}{\partial \tilde{y}} = 0. \tag{3.19}$$

$$\frac{\partial \tilde{U}}{\partial t} + \left(\tilde{U}\frac{\partial \tilde{U}}{\partial \tilde{x}} + \tilde{V}\frac{\partial \tilde{U}}{\partial \tilde{y}} \right) K = -\frac{\partial \tilde{P}}{\partial \tilde{x}} + \frac{1}{Re}\nabla_\perp^2 \tilde{U} + \frac{\tilde{U}}{\tau} + \frac{Ha^2}{Re}\tilde{j}_y \mathcal{B}_z^0, \tag{3.20}$$

$$\frac{\partial \tilde{V}}{\partial t} + \left(\tilde{U}\frac{\partial \tilde{V}}{\partial \tilde{x}} + \tilde{V}\frac{\partial \tilde{V}}{\partial \tilde{y}} \right) K = -\frac{\partial \tilde{P}}{\partial \tilde{y}} + \frac{1}{Re}\nabla_\perp^2 \tilde{V} + \frac{\tilde{V}}{\tau} - \frac{Ha^2}{Re}\tilde{j}_x \mathcal{B}_z^0. \tag{3.21}$$

These equations are complemented with the induction equation (3.7) and Ampère's law (3.8).

The solution of equation (3.15) that determines the function $\overline{f}$ needed to model the Hartmann-Rayleigh friction due to the presence of the bottom wall, becomes very complicated if the $\tilde{z}$-dependence of B_z^0 is introduced, even for simple $g(\tilde{z})$ functions. This prevent us from getting an analytical solution. Therefore, we will neglect the field decay in the layer thickness and take $g(\tilde{z}) = 1$. With such approximation, the second order differential equation reads

$$\frac{d^2 f}{d\tilde{z}^2} - (Ha\ \mathcal{B}_z^0(\tilde{x},\tilde{y}))^2 f = 0. \tag{3.22}$$

The solution that satisfies the previously stated boundary and normalization conditions has the form

$$\overline{f} = \frac{\mathcal{H}a}{\mathcal{H}a - tanh(\mathcal{H}a)}\left(1 - \frac{cosh[\mathcal{H}a(\tilde{z}-1)]}{cosh(\mathcal{H}a)}\right), \tag{3.23}$$

where $\mathcal{H}a = Ha\ B_z^0$ is defined as the local Hartmann number. Using the previous definitions for τ^{-1} y K, we found

$$\tau^{-1} = -\frac{1}{\varepsilon^2 Re}\frac{\mathcal{H}a^2 tanh(\mathcal{H}a)}{\mathcal{H}a - tanh(\mathcal{H}a)}, \tag{3.24}$$

$$K = \frac{1}{2}\left(\frac{\mathcal{H}a}{\mathcal{H}a - tanh(\mathcal{H}a)}\right)^2\left(2 + \frac{1}{\cosh^2(\mathcal{H}a)} - \frac{3tanh(\mathcal{H}a)}{\mathcal{H}a}\right). \tag{3.25}$$

Expression (3.24) models both the magnetic (Hartmann) friction in the zone of high magnetic field strength and the viscous (Rayleigh) friction in zones where the magnetic field is negligible. It depends on $\tilde{x}-\tilde{y}$ coordinates via the applied magnetic field. It has a maximum at the origin where the applied magnetic field strength is also maximum, and decays to a constant (viscous) value as the distance from the origin grows. In turn, the K factor given by equation (3.25) takes the value of 1 in all the flow domain except in the region of high magnetic field, where it takes values slightly higher (~ 1.2) .

It is important to note that the generation of vorticity by Lorentz forces and the stability of the flow are strongly influenced by the uniformity or non-uniformity of the applied magnetic field. The generation of vorticity can be analyzed by looking at the curl of the Lorentz force, namely, $\nabla\times(\mathbf{j}\times\mathbf{B}^0) = (\mathbf{B}^0\cdot\nabla)\mathbf{j} + (\mathbf{j}\cdot\nabla)\mathbf{B}^0$, where $\mathbf{j}$ denotes the induced electric current density. In flows under uniform fields, induced currents form cross-sectional loops (in planes parallel to the applied field) that close through Hartmann layers. In this case, the vorticity is generated by the term $(\mathbf{B}^0\cdot\nabla)\mathbf{j}$. Further, Hartmann braking generated due to currents closing through Hartmann layers tend to stabilize the flow. On the other hand, under non-uniform fields, electric currents form loops in both planes parallel and perpendicular to $\mathbf{B}^0$ and the term $(\mathbf{j}\cdot\nabla)\mathbf{B}^0$ strongly contributes to the vorticity generation. In fact, current loops in planes perpendicular to $\mathbf{B}^0$ can modify dramatically the velocity distribution and affect the flow stability.

Recently, several experimental studies have been carried out at the University of Ilmenau, Germany, to analyze flows of liquid metals, (GaInSn eutectic alloy) past magnetic obstacles, with magnetics fields generated by permanent magnets (Andreev

et al. 2006, Kolesnikov et al. 2008, Andreev et al. 2009). Some experiments (Andreev et al. 2006, Andreev et al. 2009) were performed in a Plexiglas duct of rectangular cross-section ($0.1 \times 0.02 \times 0.5\ m$ width, height and length respectively), by placing two permanent magnets at the top and bottom walls of the duct. The magnets were located at a distance of $0.12\ m$ from the inlet and different magnet sizes were considered. By means of an electromagnetic pump, a steady LM flow was continuously recirculated in the duct and Re was varied in the range of $5 \times 10^2 - 1.6 \times 10^4$ while Ha was equal to 400 and 320 (based on the height of the duct as characteristic length scale and with B_{max} taken at the middle distance between the magnets). In these experiments they detected steady structures formed by three pairs of vortices that appear in the wake behind the magnetic obstacle.

Another experiment (Kolesnikov et al. 2008) was performed in a rectangular container $1.2 \times 0.1 \times 0.025\ m$ with a free surface layer of LM (with a thickness of $0.01\ m$). At the free surface of the metal alloy a 4% HCl solution was added to avoid oxidation. A permanent rectangular magnet ($0.04 \times 0.03 \times 0.02\ m$) placed externally but close to the bottom wall, was dragged with constant velocity along the midline of the longer side of the container. The maximum magnetic field measured at the inner surface of the bottom wall was $0.245\ T$ and $0.125\ T$ at a height of $0.01\ m$. By controlling the magnet velocity, the Reynolds number, was varied in the range of 20-2000, while the Hartmann number is reported with a value of 50. Here, both the Reynolds number and the Hartmann are based on the layer thickness, h, and are indicated as Re_h and Ha_h. For $Re_h = 100$ the flow structure observed, consist also of three pair of vortices (see Figure 3.12).

The Q2D model based on equations (3.7)-(3.8), (3.19)-(3.21) and (3.24)-(3.25) was implemented numerically to simulate the six-vortex flow pattern observed experimentally in the free surface shallow LM flow past a magnetic obstacle (Kolesnikov et al. 2008). The separation between the lateral boundaries, H, which determines the blockage parameter $\beta = 1/H$, as well as the aspect ratio of the rectangular magnet were preserved according to the experimental conditions. In fact, in dimensionless units based on the transversal side length of the magnet, L_y, the blockage parameter coincides with the constrainment factor κ Hence, a rectangular domain with a length of 35 dimensionless units (based on the larger side length of the rectangular magnet, L_y) and 2.5 units in the cross-stream direction was used with a grid of 424×200. The same boundary conditions mentioned in section 3.2.1, were applied except that at the lateral boundaries, where no-slip conditions ($\tilde{U} = \tilde{V} = 0$) were imposed to comply with experimental conditions. The Reynolds number reported in the experiment, $Re_h = 100$, ($h = 0.01\ m$), was used for the simulation, while the Hartmann number Ha_h, was taken as 50, which corresponds to the reported magnetic field strength at the inner surface of the bottom wall.

Figure 3.12: Experimental observations in GaInSn alloy for $Re = 100$ and $Ha = 50$. The visualization of flow was obtained using 4% HCl solution covering the metal surface (Kolesnikov et al. 2008).

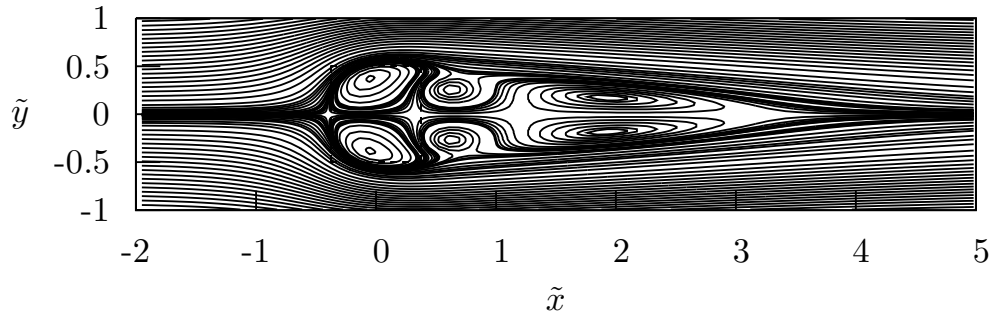

Figure 3.13: Instantaneous values of the stream function for: $Re = 100$ and $Ha = 50$. The uniform flow is from the left to the right, the magnetic obstacle is denoted by the dashed square located in the region $-0.375 < x < 0.375$ and $-0.5 < y < 0.5$.

Results of the numerical simulation are shown in Figure 3.13, where the flow streamlines are shown. It can be observed that numerical results reproduce accurately the experimental steady six-vortex flow pattern where the so-called inner, connected and attached vortices appear (Votyakov et al. 2007, 2008). It is worth mentioning that this stable configuration was obtained with a Q2D numerical simulation, which contradicts the assertion by Votyakov et al. (2008) that stationary recirculation in a 2D numerical simulation is only possible in creeping flow regime. These authors state that the six-vortex pattern can only be obtained from a 3D numerical model. Our results demonstrate that, in spite of the limitations of the Q2D approach, it allows the reproduction of the main physical features of the flow. It appears that the suitable assessment of the bottom friction modeled through the Hartmann-Rayleigh

terms in the momentum balance equations, is a key ingredient to get stable vortex configurations. The possibility of finding either two or six steady vortices seems to be related to the geometrical flow configuration, in particular to the constrainment factor $\kappa = L_y/H$. In the previously simulated case, $\kappa = 0.4$, while two vortices have been reported for $\kappa = 0.02$ (Votyakov et al. 2008) and $\kappa = 0.05$ (Cuevas et al. 2006a, Beltrán 2006).

From the topological point of view, it is interesting to notice that in the configuration of six vortices, the flow gives rise to three hyperbolic critical points aligned with the flow direction. Also, three pairs of elliptic critical points appear, each pair aligned in a direction perpendicular to flow direction. This geometrical distribution of critical points has not been observed in the flow past a solid body where front and trailing stagnant points (topologically equivalent to hyperbolic points), aligned with the direction of the flow, are formed. The hyperbolic points are the saddle points in the flow, while the elliptic points are the center of the vortices

A meaningful global parameter for the characterization of shallow flows past bluff bodies is the velocity deficit (Chen and Jirka 1997). This parameter is also very helpful for the analysis of the flows under consideration. It is defined as

$$R = \frac{U_m - U_0}{U_m + U_0}. \tag{3.26}$$

where U_m is the velocity along the midline in the flow direction, and U_0, is the imposed inlet velocity. In the present case, $U_0 = 1$. When $R = 0$, the flow is uniform; in turn, if $R = -1$, the velocity in the wake in the mid axial line is zero; on the other hand, the condition $R < -1$, means that the fluid in the midline moves in the opposite direction to the main oncoming flow, in other words, reveals the presence of recirculations. It is expected that along the wake, R will first decrease taking negative values, reach a minimum (or several local minima), and then increase to become zero at a sufficiently long distance downstream of the localized magnetic field.

In Figure 3.14, the velocity deficit R is shown as a function of the axial coordinate $\tilde{x}$, for $Re_h = 100$ and $Ha_h = 50$, which corresponds to the experimental case of Figure 3.12. It is observed that the velocity deficit decreases abruptly as the flow encounters the localized magnetic field; it shows clearly three regions; first, it reaches a global minimum at $\tilde{x} = -0.15$; second, it starts increasing going to -1, reaching a maximum at $\tilde{x} = 0.68$; third, it again decreases and reaches a local minimum at $\tilde{x} = 2.11$; finally, it increases as the distance from the magnet obstacle grows and reaches the zero value around 15 units downstream of the point of maximum magnetic field strengh ($\tilde{x} = 0$). All these maximums and minimums coincide with the axial coordinate where the center of inner, connected and attached vortices in the flow (elliptic points) are located.

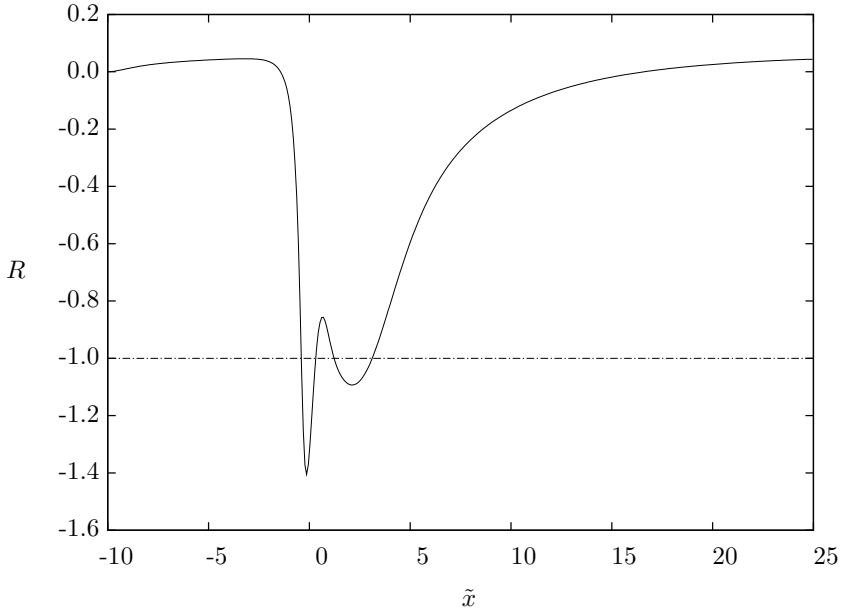

Figure 3.14: Velocity deficit as a function of the axial coordinate $\tilde{x}$.

The points where $R = -1$ are located at $\tilde{x} = -0.4, 0.32, 1.22, 3.37$ and correspond to hyperbolic points, as can be seen from Figure 3.13. These in fact, are stagnation points. Figures 3.15 and 3.16 show $\tilde{U}$ and $\tilde{V}$ velocity components, respectively, as functions of the cross-stream $\tilde{y}$-coordinate, at different axial positions that correspond to the hyperbolic (stagnation) points (so that $\tilde{U} = \tilde{V} = 0$ at $\tilde{y} = 0$). It can be observed that the $\tilde{U}$ velocity component in Figure 3.15 is completely symmetric with respect to the line $\tilde{y} = 0$

Owing to the non-slip condition at the lateral solid walls , the $\tilde{U}$ component develops an M-shape profile as the flow pass through the magnetic obstacle. This profile is characteristic of MHD duct flows at the entrance or exit of a non-uniform field created by the poles of a magnet (Müller and Bühler 2001, Moreau 1990). However, the physical effects that produce these profiles are different. In the magnetic obstacle flow the high velocities near the lateral walls are due to the flow expelled from the central region where the opposing magnetic force is higher and vortices are located. Note that the lower lateral velocity corresponds to the profile at $\tilde{x} = -0.4$ where the flow first encounters the opposing Lorentz force. In turn, the highest lateral velocity is found at $\tilde{x} = 0.32$ which corresponds to the axial location of the second hyperbolic point located approximately at the exit of the localized magnetic field.

On the other hand, Figure 3.16 shows the antisymmetric profiles of the $\tilde{V}$ com-

ponent as a function of $\tilde{y}$. Note that the highest magnitude is reached at $\tilde{x} = -0.4$, where the oncoming flow is first deviated by the magnetic obstacle. This also reflects the fact that the inner magnetic vortices are the more intense, followed by the connected and, finally the attached vortices.

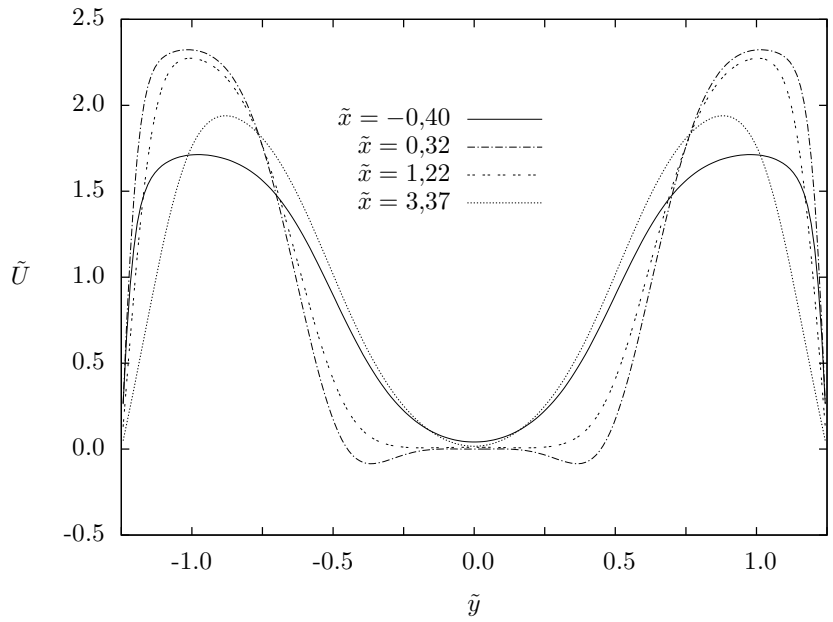

Figure 3.15: $\tilde{U}$ velocity component vs. $\tilde{y}$.

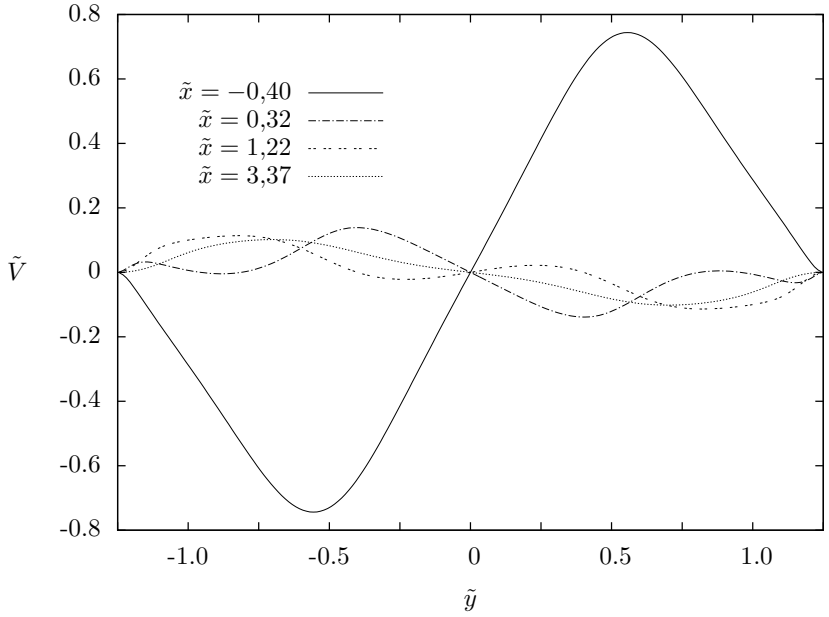

Figure 3.16: $\tilde{V}$ velocity component vs. $\tilde{y}$.

One important conclusion of the previous results is that a Q2D model that considers in a suitable way the bottom friction effects, is able to reproduce the main flow characteristics for the case of shallow liquid metal flows past a magnetic obstacle in the laminar regime. Also, it seems that the three pair of vortices are due to a combination of the aspect ratio of the magnet and the width of the duct and not necessarily to 3D effects, as was claimed in the numerical study performed by Votyakov et al. 2008.

3.3.2 Q2D Electrolytic flow past a magnetic obstacle

As it was mentioned in Chapter 1, flows produced by the interaction of injected electric currents and traveling localized magnetic fields in thin electrolytic layers have been explored in the past (Honji 1991, Honji and Haraguchi 1995, Afanasyev and Korabel 2006). To our knowledge, there is only one attempt to model these flows with a purely hydrodynamic 2D approach (Afanasyev and Korabel 2008). Here, we use a Q2D approach to simulate the characteristic flow patterns observed by Honji and Haraguchi (1995) although a full comparison is not possible since the complete information about the flow configuration and physical conditions is not available.

Let us now apply the Q2D model formulated in section 3.3 to the shallow flow of an electrolyte through a localized non-uniform magnetic field produced by a permanent

magnet, externally attached to the bottom wall. In this case, we consider the injection of a direct electrical current in the thin layer, in a direction perpendicular to the main flow, in such a way, that the interaction with the magnetic field generates a non-uniform Lorentz force that opposes the oncoming flow. It is necessary to remind that the low electrical conductivity of electrolytes, compared with that of liquid metals, and the small magnetic field intensity produced by a permanent magnets result in low Hartmann numbers (of order 10^{-1}). Therefore, the induced Lorentz force in equations (3.17) and (3.18) can be neglected, and it is unnecessary to solve the induction equation (3.7) in order to determine the induced magnetic field. With the former simplifications, the dimensionless averaged equations of motion take the form

$$\frac{\partial \tilde{U}}{\partial \tilde{x}} + \frac{\partial \tilde{V}}{\partial \tilde{y}} = 0, \tag{3.27}$$

$$\frac{\partial \tilde{U}}{\partial t} + \left(\tilde{U}\frac{\partial \tilde{U}}{\partial \tilde{x}} + \tilde{V}\frac{\partial \tilde{U}}{\partial \tilde{y}} \right) K = -\frac{\partial \tilde{P}}{\partial \tilde{x}} + \frac{1}{Re}\nabla_{\perp}^{2}\tilde{U} + \frac{\tilde{U}}{\tau} - Q\ \mathcal{B}_{z}^{0}, \tag{3.28}$$

$$\frac{\partial \tilde{V}}{\partial t} + \left(\tilde{U}\frac{\partial \tilde{V}}{\partial \tilde{x}} + \tilde{V}\frac{\partial \tilde{V}}{\partial \tilde{y}} \right) K = -\frac{\partial \tilde{P}}{\partial \tilde{y}} + \frac{1}{Re}\nabla_{\perp}^{2}\tilde{V} + \frac{\tilde{V}}{\tau}, \tag{3.29}$$

In this case, since $Ha \ll 1$ equation (3.15) for the function f that determines the friction model reduces to

$$\frac{d^2 f}{d\tilde{z}^2} = \varepsilon^2\ Q\ Re\ \mathcal{B}_{z}^{0}(\tilde{x},\tilde{y})\ g(\tilde{z}). \tag{3.30}$$

If we approximate the decay of the magnetic field through the layer thickness using the function $g(\tilde{z}) = \exp(-\gamma\ \tilde{z})$ (Figueroa et al. 2009), it is possible to integrate analytically equation (3.30) with the proper boundary conditions, yielding (once it is normalized)

$$\overline{f} = \frac{e^{-\gamma\tilde{z}} + \tilde{z}\gamma e^{-\gamma} - 1}{\frac{1}{\gamma}(1-e^{-\gamma}) + \frac{\gamma}{2}e^{-\gamma} - 1} \tag{3.31}$$

Using the definitions for $\tau^{-}1$ y K we found

$$\tau^{-1} = \frac{\gamma(1-e^{-\gamma})}{\frac{1}{\gamma}(1-e^{-\gamma}) + \frac{\gamma}{2}e^{-\gamma} - 1}, \tag{3.32}$$

$$K = 1. \tag{3.33}$$

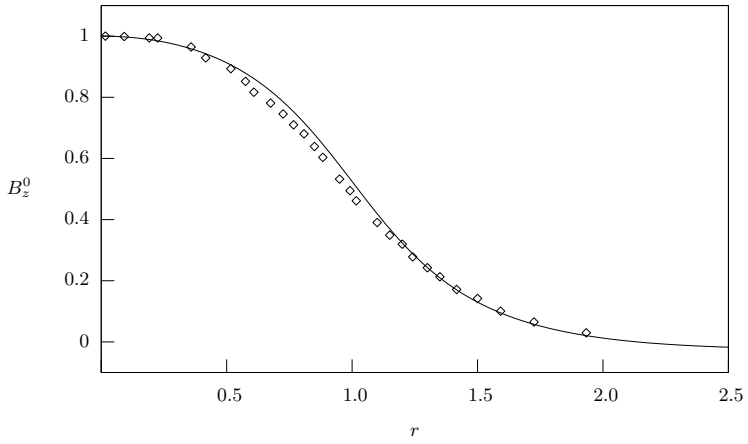

Figure 3.17: Radial normalized distribution of the $\tilde{z}$-component of the magnetic field at $\tilde{z} = 0.5$ and $\gamma = 0.51$, diamonds correspond to the experimental measurements (Honji and Haraguchi 1995) and the continuous line to equation (3.14)

The system of equations (3.27)-(3.29) and (3.32)-(3.33) was solved numerically using the same boundary conditions as the ones for the LM flow and the parameters were close [1] to those used in the experiments by Honji and Haraguchi (1995). They report experimental observations of an electromagnetically forced flow in a thin layer of an electrolyte (0.005 m deep, 0.2 m wide and 1 m long) produced by the interaction of an imposed D.C. current and a localized magnetic field. A permanent cylindrical magnet (0.03 m diameter with a maximum magnetic field intensity of 0.48 T) was placed underneath the electrolyte and dragged along the thin layer at constant velocity $\tilde{U}$ ranged from 0.013 m/s to 0.07 m/s. The experiments were conducted with in the parameter ranges $31 < Re < 1.7 \times 10^3$ and $0.13 < Q < 97$, where now Re is based on the magnet diameter. Using the diameter of the cylindrical magnet as the characteristic horizontal length, the aspect ratio results $\varepsilon = h/L = 0.166$

The authors report the radial variation of the normal magnetic field component of the permanent magnet. Figure 3.17 shows the experimental values and the corresponding fitting obtained from the superposition of two magnetized surfaces separated by a small distance, given by the analytical expressions by McCaig (1977). These surfaces correspond to the north and south poles of the magnet.

[1] Note all the required experimental conditions are reported in the paper by Honji and Haraguchi (1995)

Figure 3.18 shows the experimental observations reported by Honji and Haraguchi (1995), where the streamtracers display flow patterns obtained under three different conditions: a) a steady open-streamline flow without any recirculation zone for $Re = 700$, $Q = 0.7$, b) a steady vortex pair for $Re = 1000$, $Q = 0.92$ and c) a vortex shedding for $Re = 1000$, $Q = 1.7$.

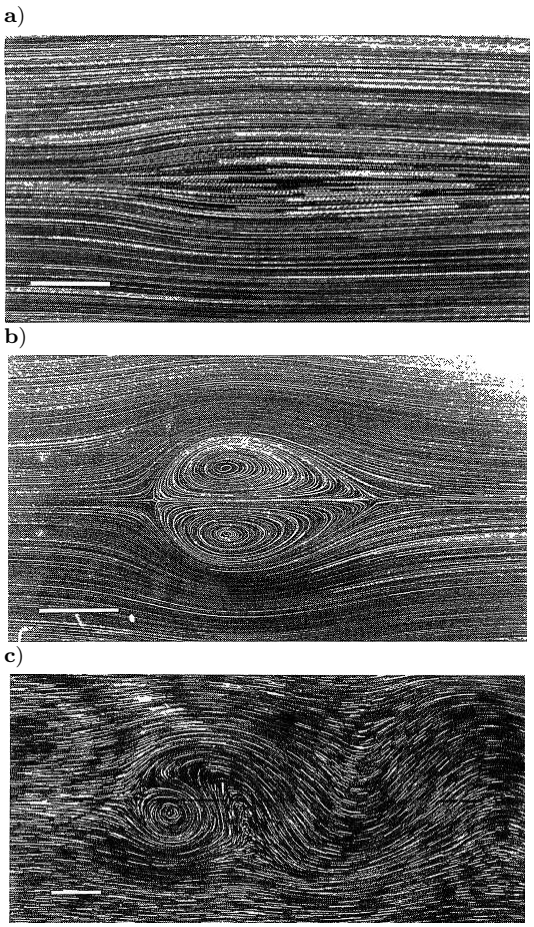

Figure 3.18: Experimental observations for : a) $Re = 700$ and $Q = 0.7$, b) $Re = 1000$ and $Q = 0.92$, c) $Re = 1000$ and $Q = 1.7$. White bars indicate 0.03 m (Honji and Haraguchi 1995)

Numerical simulations based on the Q2D numerical model were carried out with the aim at reproducing the experimental observations. The numerical solution was obtained in a rectangular domain with a length of 35 dimensionless units in the streamwise

direction and 7 units in the cross-stream direction, while a grid of 212×201 was used. In this case, according to the experimental configuration the constrainment factor take the value $\kappa = 0.14$, more than two and a half times smaller than the value of the liquid metal flow case ($\kappa = 0.4$, see section 3.3.1)

Figure 3.19 shows the instantaneous values for the streamfunction calculated numerically, where the flow patterns observed experimentally, are reproduced. The open-streamline flow shown in Figure 3.19a) was obtained for the same parameter values as in the experimental case ($Re = 700$, $Q = 0.7$). The steady vortex pair shown in Figure 3.19b) corresponds to $Re = 1000$ and $Q = 1.6$ although vortex pair flow appears even for $Q = 1.5$. For the experimental reported parameters ($Re = 1000$, $Q = 0.92$) the numerical simulation shows a steady open-streamline flow with no vortices. In turn, the vortex shedding pattern observed in Figure 3.19c) was obtained for $Re = 1000$ and $Q = 1.9$. This Q value is slightly higher than the value reported in the experiment ($Q = 1.7$). On the other hand, Strouhal number calculated numerically is 0.15 while the reported experimental value is 0.11. The numerical model is able to grasp the main characteristic features of the experimental situation and predict the transition from a steady regime to a unstable periodic vortex shedding flow. The difference in the Q values may be due to numerical diffusion or an overestimation of the bottom friction that requires a stronger Lorentz force to find the flow transition. However, it is important to remark that the experimental configuration and physical conditions are not reported in a complete form. In order to perform a fair comparison with numerical results, additional experimental data are required.

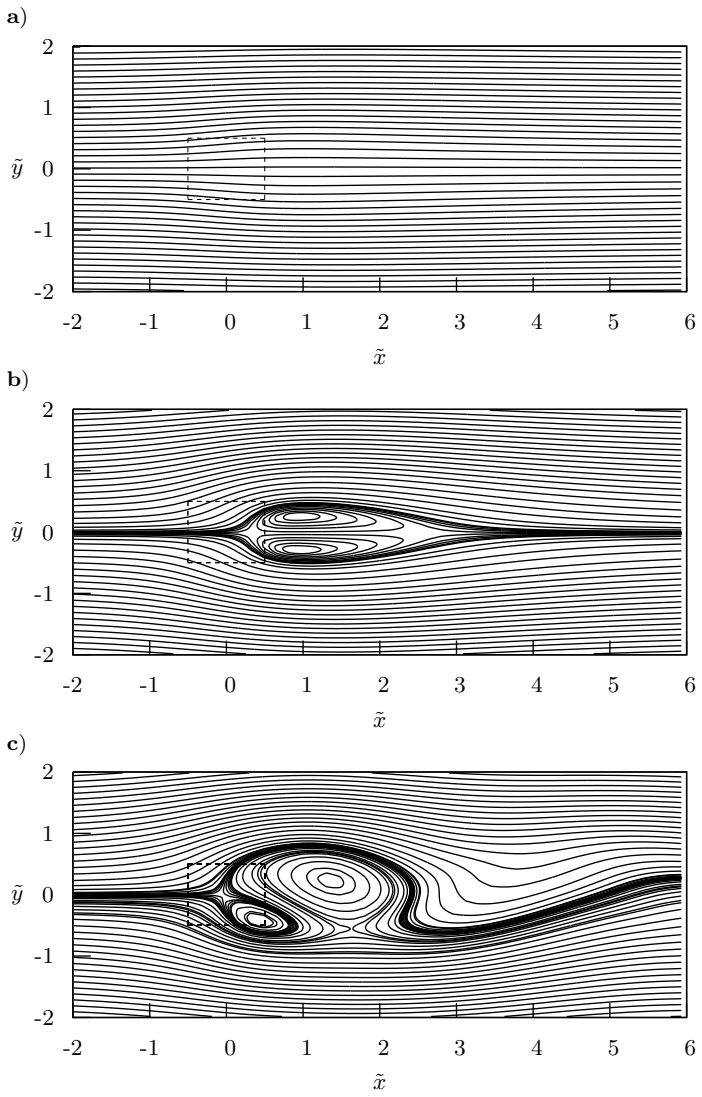

Figure 3.19: Numerical simulations for the flow past a magnetic obstacle, the uniform flow is from the left to the right, the magnetic obstacle is denoted by the dashed square located in the region $-0.5 < \tilde{x} < 0.5$ and $-0.5 < \tilde{y} < 0.5$, figures correspond to instantaneous values of the stream function for: a) $Re = 700$ and $Q = 0.7$, b) $Re = 1000$ and $Q = 1.6$, c) $Re = 1000$ and $Q = 1.9$. $\kappa = 0.14$.

In Figure 3.20 the velocity deficit R, is shown for the three different simulated cases. For the case $Re = 700$ and $Q = 0.7$, we find that $R > -1$, which means that

there are not vortices in the flow. In turn, for the case $Re = 1000$ and $Q = 1.6$, the condition $R < -1$ is obtained, which indicates the existence of recirculations (vortices) in the flow. Finally, when $Re = 1000$ and $Q = 1.9$, the condition $R < -1$ is also met, but the curve displays oscillations that denote the emergence of the flow instability.

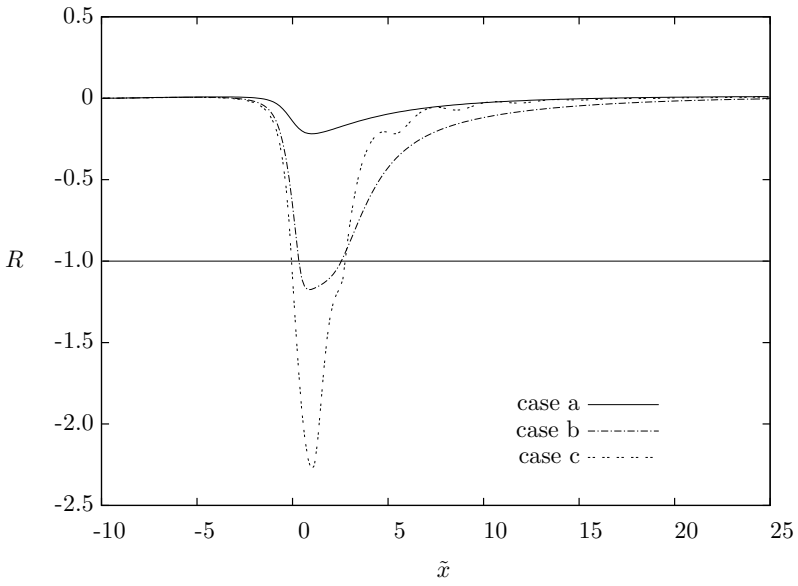

Figure 3.20: Velocity deficit as a function of the axial coordinate for the three numerically calculated cases. a) $Re = 700$, $Q = 0.7$ b) $Re = 1000$, $Q = 1.6$ c) $Re = 1000$, $Q = 1.9$. $\kappa = 0.14$

It is found that the minimum value for R is located near $\tilde{x} = 1$ for the three cases. Unlike the steady LM flow explored in the previous section, in case b) (steady vortex pair) only two hyperbolic and two elliptic points exist. Figure 3.21 shows the $\tilde{U}$ velocity component as a function of the cross-stream $\tilde{y}$-coordinate, at the axial position $\tilde{x} = 1$. A symmetric profile is observed for cases a) ($Re = 700$, $Q = 0.7$) and b) ($Re = 1000$, $Q = 1.6$), while for c) the symmetry is lost due to the unstable behavior of the flow. Comparing these profiles with those presented in Figure 3.15 for the LM flow, it is observed that the M-shape is less pronounced. This is due, in part, to the small constrainment factor of the electrolytic flow ($\kappa = 0.14$), compared to the LM flow ($\kappa = 0.4$), which restricts the opposing Lorentz force to a narrower central region. In fact, excluding the thin shear layers where the non-slip condition is satisfied, the profiles in the electrolytic flow approach those in a LM flow with stress-free conditions in the lateral boundaries (Cuevas et al. 2006a). Finally, Figure

3.22 shows the cross stream velocity component $\tilde{V}$ as a function of the cross-stream $\tilde{y}$-coordinate. As expected, profiles for cases a) and b) are antisymmetric. The profile corresponding to the vortex shedding case c) displays a much higher positive values which reflects the more intense recirculation that appears during the time periodic flow.

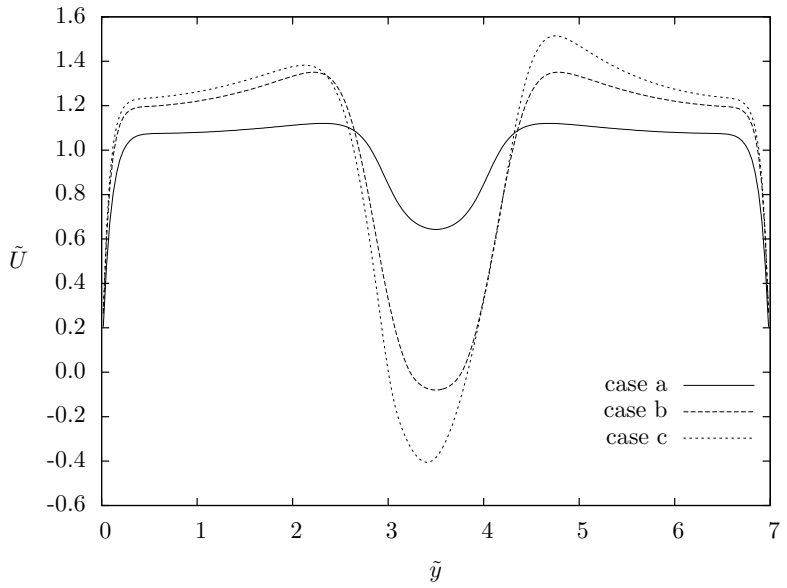

Figure 3.21: $\tilde{U}$ velocity component vs. $\tilde{y}$ for a) $Re = 700$, $Q = 0.7$; b) $Re = 1000$, $Q = 1.6$; c) $Re = 1000$, $Q = 1.9$.

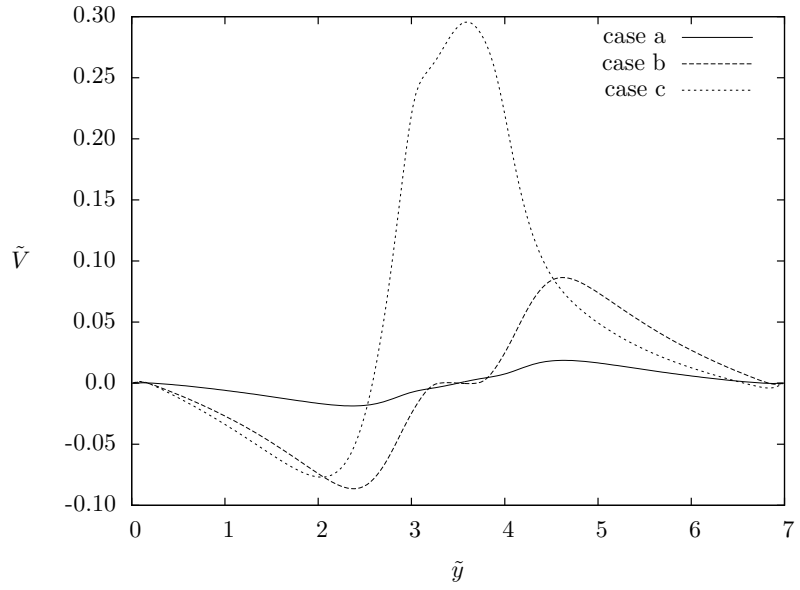

Figure 3.22: $\tilde{V}$ velocity component vs. $\tilde{y}$ for a) $Re = 700$, $Q = 0.7$; b) $Re = 1000$, $Q = 1.6$; c) $Re = 1000$, $Q = 1.9$.

3.4 3D numerical simulation of the electrolytic flow past a magnetic obstacle.

The literature on flows of conducting fluids past magnetic obstacles is not extense, in particular, that related with numerical simulations. The 3D flow of a liquid metal past a magnetic obstacle was studied numerically in the papers by Votyakov et al. (2007, 2008). These authors consider a flow between parallel insulated walls with a localized magnetic field produced by the south and north poles of two magnets located at the top and bottom walls. They analyze the flow characteristics for different magnetic field configurations according to the constrainment factor κ and, particularly, explore the 3D structure of the steady six-vortex pattern. On the other hand, to our knowledge, apart from the 2D numerical simulation by Afanasyev and Korabel (2008), where magnetic forces are modeled as point hydrodynamic forces, numerical simulations of the electrolytic flow past a magnetic obstacle, have not been reported in the literature.

In this section, we present a 3D numerical simulation for the electrolytic shallow flow past a magnetic obstacle, using the full 3D distribution of the applied magnetic field. We consider the same flow configuration as in section 3.3.2, that is, a thin layer of electrolyte in uniform motion in a rectangular open channel with a square permanent

magnet (modeled by the superposition of two magnetized surfaces) placed externally at the bottom wall, so that a non-uniform field is produced in a localized region. It is assumed that a DC current is injected in the fluid layer, transversally to the main flow direction, in such a way that the interaction with the magnetic field generates a non-uniform Lorentz force that opposes the oncoming flow. The rigid bottom wall as well as the media in contact with the free-surface at the top of the layer are assumed electrically insulating.

The normal $\tilde{z}$-component of the magnetic field produced by a rectangular magnetized surface has already been presented in section 3.2 (equation (3.1)). The expressions for the components in the $\tilde{x}$- and $\tilde{y}$-directions are given in dimensional terms by McCaig (1977)

$$\begin{aligned}\mathcal{B}_x^0 &= B_{max}\log_e\frac{Y+b+[(X-a)^2+(Y+b)^2+(Z-Z_0)^2]^{1/2}}{Y-b+[(X-a)^2+(Y-b)^2+(Z-Z_0)^2]^{1/2}} \\ &\times \frac{Y-b+[(X+a)^2+(Y-b)^2+(Z-Z_0)^2]^{1/2}}{Y+b+[(X+a)^2+(Y+b)^2+(Z-Z_0)^2]^{1/2}},\end{aligned} \tag{3.34}$$

$$\begin{aligned}\mathcal{B}_y^0 &= B_{max}\log_e\frac{X+a+[(X+a)^2+(Y-b)^2+(Z-Z_0)^2]^{1/2}}{X-a+[(X-a)^2+(Y-b)^2+(Z-Z_0)^2]^{1/2}} \\ &\times \frac{X-a+[(X-a)^2+(Y+b)^2+(Z-Z_0)^2]^{1/2}}{X+a+[(X+a)^2+(Y+b)^2+(Z-Z_0)^2]^{1/2}}.\end{aligned} \tag{3.35}$$

We again consider $a=b=L$ and take L as the characteristic length scale.

The dimensionless equations of motion take the form

$$\frac{\partial\tilde{U}}{\partial\tilde{x}}+\frac{\partial\tilde{V}}{\partial\tilde{y}}+\frac{\partial\tilde{W}}{\partial\tilde{z}}=0, \tag{3.36}$$

$$\frac{\partial\tilde{U}}{\partial t}+\tilde{U}\frac{\partial\tilde{U}}{\partial\tilde{x}}+\tilde{V}\frac{\partial\tilde{U}}{\partial\tilde{y}}+\tilde{W}\frac{\partial\tilde{U}}{\partial\tilde{z}}=-\frac{\partial P}{\partial\tilde{x}}+\frac{1}{Re}\nabla^2\,\tilde{U}-Q\;B_z^0, \tag{3.37}$$

$$\frac{\partial\tilde{V}}{\partial t}+\tilde{U}\frac{\partial\tilde{V}}{\partial\tilde{x}}+\tilde{V}\frac{\partial\tilde{V}}{\partial\tilde{y}}+\tilde{W}\frac{\partial\tilde{V}}{\partial\tilde{z}}=-\frac{\partial P}{\partial\tilde{y}}+\frac{1}{Re}\nabla^2\,\tilde{V}, \tag{3.38}$$

$$\frac{\partial\tilde{W}}{\partial t}+\tilde{U}\frac{\partial\tilde{W}}{\partial\tilde{x}}+\tilde{V}\frac{\partial\tilde{W}}{\partial\tilde{y}}+\tilde{W}\frac{\partial\tilde{W}}{\partial\tilde{z}}=-\frac{\partial P}{\partial\tilde{z}}+\frac{1}{Re}\nabla^2\,\tilde{W}-Q\;B_x^0. \tag{3.39}$$

The scale factors are the same as the ones considered in section 3.3.2, except that L has also been used to normalize the vertical $\tilde{z}$-coordinate. We can see from equations

(3.36)-(3.39) that now, in addition to the component in the main flow ($\tilde{x}$) direction, the Lorentz force has also a component in the $\tilde{z}$-direction that may affect the flow distribution in the layer thickness. This, evidently, cannot be captured with 2D or Q2D approximations.

The boundary conditions for the present problem are the following. At the inlet a plug flow is imposed ($\tilde{U} = 1$, $\tilde{V} = \tilde{W} = 0$), while at the outlet Neumann conditions were used ($\frac{\partial \tilde{U}}{\partial \tilde{x}} = \frac{\partial \tilde{V}}{\partial \tilde{x}} = \frac{\partial \tilde{W}}{\partial \tilde{x}} 0$). For the velocity components at the lateral and bottom walls, we used no-slip boundary conditions ($\tilde{U} = \tilde{V} = \tilde{W} = 0$) and finally, assuming that the free surface remains unperturbed, the absence of shear stresses at this surface was imposed ($\tilde{W} = 0$, $\frac{\partial \tilde{U}}{\partial \tilde{z}} = \frac{\partial \tilde{V}}{\partial \tilde{z}} = 0$).

The 3D model presented here represents a more realistic simulation of the problem, however, it comes with a price tag of considerably higher requirements in memory and CPU time. For this reason, we implement a parallelized numerical code for the flow simulation. In the next section, a brief explanation of the implemented procedure is given.

3.4.1 Parallelization strategy

In order to solve the 3D system of equations (3.36)-(3.39) with the proper boundary conditions, we developed a parallelized version of the numerical code. For the sake of simplicity, we explain here the strategy for the 2D dimensional case although the 3D extension is straigthforward.

A prudential approach to parallelize numerical algorithms for solving partial differential equations is to divide the total domain into subdomains $\Omega_1 ... \Omega_N$, and to treat each subdomain on a separate processor. A possible domain decomposition method is the one in which the subdomains overlap, see Figure 3.23.

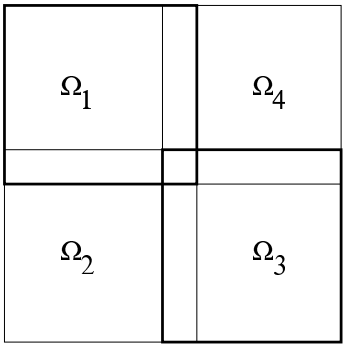

Figure 3.23: Overlapping domains

Each subdomain is thus assigned to a process that computes the unknowns belonging to this subdomain. Each individual process, therefore, no longer requires access to the whole data arrays, but rather to a part of it, and the computing operations of an iterative solution algorithm are divided among the processes. If the latter are then assigned to different processors, the algorithm can be carried out in parallel. Each processors memory only contains the data required by those processes running on itself. Note that the parallelization requires a load balancing scheme, in which the subdomains mantain an equal distribution of fluid cells among the subdomains, thereby distributing the load on the process as equally as possible.

The Message Passing Interface (MPI) was used to parallelize the code. In particular, MPI_Allreduce instruction was used to communicate the residual stop criterium to all the processors, while MPI_Send and MPI_Recv instructions were used to update the new values (velocities, pressure and induced magnetic field) calculated at each time step. The boundary values are calculated by the processes that deal with neighboring subdomains, unless they fall outside the total domain. These boundary values must therefore be sent, in an appropriate form and with a proper frequency, to the neighboring processes. The data exchange is performed in four time steps to the left, to the right, up, and down (in the 3D case additional data exchange is necessary to the rear and to the front). To evade a deadlock situation, one must stick to the following (or similar) order:

send to the left - receive from the right,
send to the right - receive from the left,
send to the top - receive from the bottom,
send to the bottom - receive from the top.

Since the code is based on a projection method, the Poisson equation for pressure, which arises from the incompressibility constraint, has to be solved at least once at each time step. It is usually the main bottleneck from a parallelizing point of view. The velocities are treated in a fully explicit way. The Poisson equation is solved using a Conjugate Gradient method (Barret et al. 1994). The pressure values located in the boundary strips must be exchanged, as represented in the left side of Figure 3.24, so that the computation can proceed in the subdomains with the most current boundary values. Since at the end of the pressure iteration the current pressure values are contained in the boundary strips, the velocity values on the subdomain boundaries can be updated without any new communication. However, in order to continue the calculation of the new velocities, the velocity values must be exchanged as depicted in the right side of Figure 3.24

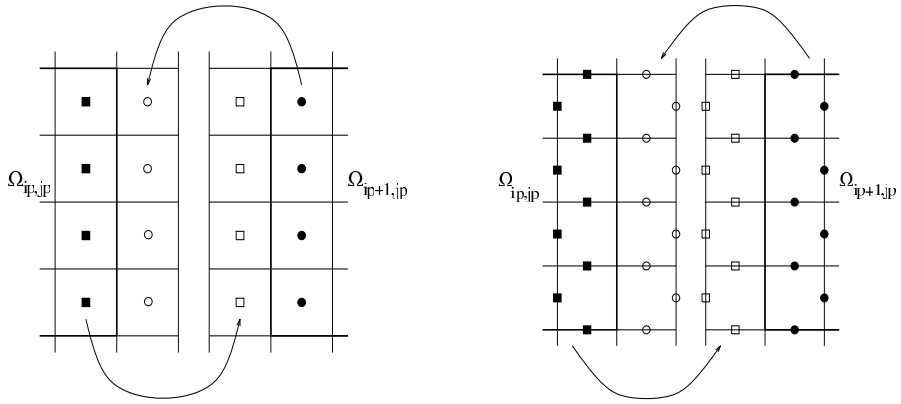

Figure 3.24: Left side: Exchange of pressure values, right side: Exchange of velocity values.

The program was compiled with the free compiler OpenMPI and run in a cluster at the Centro de Investigación en Energía, UNAM.

3.4.2 Numerical results

The computational domain was similar to the one used in section 3.2 but incorporating the vertical dimension. Therefore, we consider a rectangular parallelepiped with side lengths of 50, 7.6 and 0.19 dimensionless units in the $\tilde{x}$-, $\tilde{y}$- and $\tilde{z}$-direction, respectively. The domain was discretized by a homogeneous regular 3D grid of $600\times182\times36$. A time step of 0.001 was used. The center of the magnetized square surface that generates the 3D magnetic field distribution was located at $\tilde{x}=\tilde{y}=\tilde{z}=0$, separated a distance of 10 units from the entrance boundary. It was verified that the inlet plug flow develops into a parabolic profile in a few units before the magnetic obstacle region is reached. Also, once the flow has passed through the localized magnetic field, the downstream distance is long enough for the flow to reach again a parabolic profile at the outlet boundary.

We explored flows with different values of Re and Q parameters, in particular, those used in the experiment by Honji and Haraguchi (1995). The main characteristic flow regimes, namely, steady open-streamlined flow, steady vortex pair and time-periodic vortex shedding, are shown by analyzing three particular cases: I) $Re=700$, $Q=0.92$, II) $Re=1000$, $Q=1.2$ and III) $Re=1000$, $Q=10$. For each case, the velocity field is shown in three different orthogonal planes that help us to discern the 3D flow structures. An important piece of information is obtained from the profile of the axial velocity component $\tilde{U}$ as a function of the vertical coordinate $\tilde{z}$ in the central

plane $\tilde{y} = 0$. As it is shown below, in the neighborhood of the magnetic obstacle, the action of the Lorentz force promotes developing profiles that go from parabolic shape to profiles with inflection points. Since the magnetic field presents a fast decay, particularly in the upward direction, the localized Lorentz force is stronger near the bottom plane ($\tilde{z} = 0$). As the Q parameter is increased, the braking force reaches higher flow planes and inflection points travel upwards. As it is well known, the existence of inflection points in the velocity profile has important consequences from the stability of the flow (Schlichting and Gertsen 2000, Schmid and Henningson 2001). On the other hand, when the Lorentz force is sufficiently strong, it can generate flow recirculation indicated by negative values of $\tilde{U}$ at a given $\tilde{z}$ plane.

Case I. $Re = 700$**,** $Q = 0.7$

These values of the governing parameters correspond to the experimental case reported by Honji and Haraguchi (1995). Numerical results show an open-streamline flow with no recirculation zones, as the pattern observed experimentally. In Figure 3.25, the velocity profiles of component $\tilde{U}$ as a function of $\tilde{z}$ at the plane $\tilde{y} = 0$, are shown for different axial positions. At $\tilde{x} = -2.0$, upstream of the magnetic obstacle, a parabolic profile is observed. The velocity decreases as the flow passes through the magnetic obstacle ($\tilde{x} = 0.0$, 0.5, 1.0) and incipient inflection points appear. We observe that the maximum breaking for the flow occurs approximately at $\tilde{x} = 1.0$. Downstream the magnetic obstacle ($\tilde{x} = 5.0$), the profile starts recovering the parabolic shape. Figure 3.26 shows the velocity field at the horizontal plane $\tilde{z} = 0.02$, where the slight perturbation caused by the magnetic obstacle is clearly observed. In fact, the effect of the Lorentz force is only detected in planes close to the bottom wall, while upper planes remain mainly unperturbed.

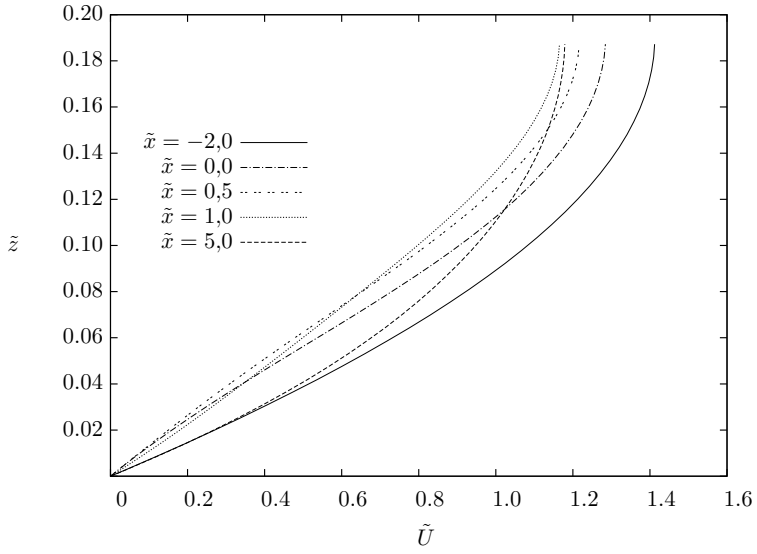

Figure 3.25: $\tilde{U}$-velocity component as function of $\tilde{z}$ for $Re = 700$ and $Q = 0.7$ taken at $\tilde{y} = 0$.

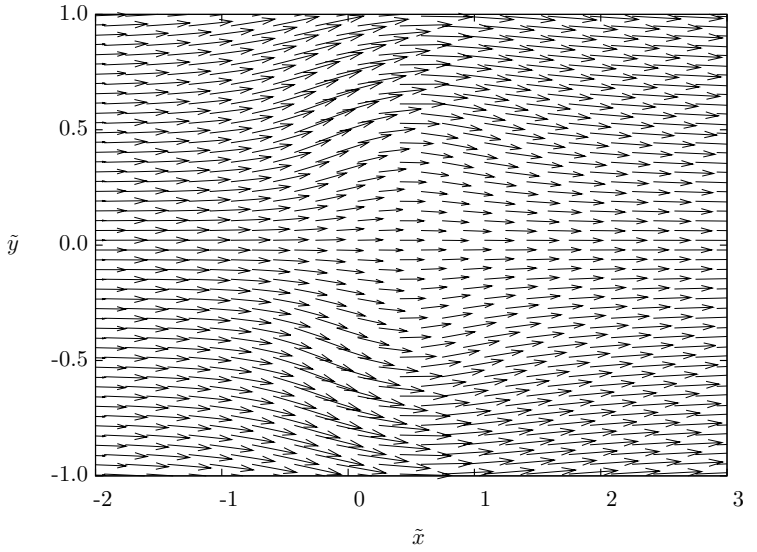

Figure 3.26: Vector velocity field in the $\tilde{x} - \tilde{y}$ plane $\tilde{z} = 0.02$, for $Re = 700$ and $Q = 0.7$.

Figure 3.27 shows a lateral view of the velocity field in the layer thickness at the mid $\tilde{x}$ - $\tilde{z}$ plane ($\tilde{y} = 0$). We observe that the breaking effect of the Lorentz force reaches only the neighborhood of the magnetic obstacle close to the bottom wall.

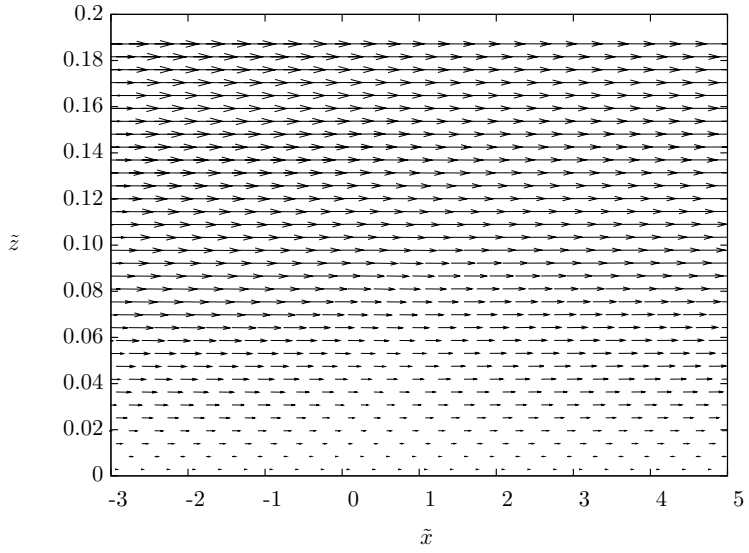

Figure 3.27: Vector velocity field in the mid $\tilde{x} - \tilde{z}$ plane ($\tilde{y} = 0$) for $Re = 700$ and $Q = 0.7$. Velocity components are scaled by a factor of 0.4.

Figure 3.28 shows the velocity field in a cross-stream vertical $\tilde{y} - \tilde{z}$ plane at $\tilde{x} = 0.5$. This axial position corresponds to the point where the $\tilde{U}$ velocity component shows the maximum velocity deficit in the flow (see Figure 3.25). It is observed that for $\tilde{z} > 0.05$ (approximately), the flow diverges from the central line $\tilde{y} = 0$, while for $\tilde{z} < 0.05$ the flow converges to this line. This complex flow behavior reveals the concurrent action of the Lorentz force components, namely, the axial and vertical components.

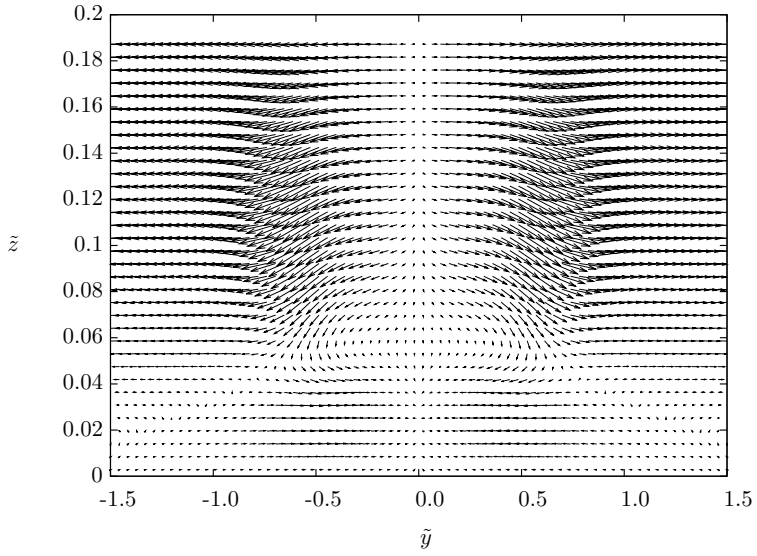

Figure 3.28: Velocity vector field in the $\tilde{y} - \tilde{z}$ plane for $Re = 700$ and $Q = 0.7$, taken at $\tilde{x} = 0.5$, velocity components are scaled by a factor of 3.

Case II. $Re = 1000$**,** $Q = 1.2$

For this case, 3D numerical results reproduce the flow pattern consisting in a steady vortex pair. The value $Q = 1.2$ is closer to the reported experimental value for this pattern ($Q = 0.92$, Honji and Haraguchi (1995)) than the one found with the Q2D model ($Q = 1.5$, see section 3.3.2). Figure 3.29 shows the velocity profiles $\tilde{U}$ vs. $\tilde{z}$ at the mid plane $\tilde{y} = 0$ for different axial positions. As in the previous case, the velocity profiles upstream ($\tilde{x} = -2.0$) and downstream ($\tilde{x} = 5.0$) of the magnetic obstacle present a parabolic shape, while the profiles within the obstacle region clearly display inflection points. In fact, $\tilde{U}$ takes negative values, indicating the existence of recirculation zones. The largest negative velocity magnitude is found at $\tilde{x} = 0.4$. A top view of the flow at the horizontal plane $\tilde{z} = 0.014$ (see Figure 3.30), corroborates the existence of a pair of symmetric counter-rotating vortices. It is important to mention that the strength of the these vortices decreases in upper planes and can hardly be identified above the mid plane $\tilde{z} = 0.095$.

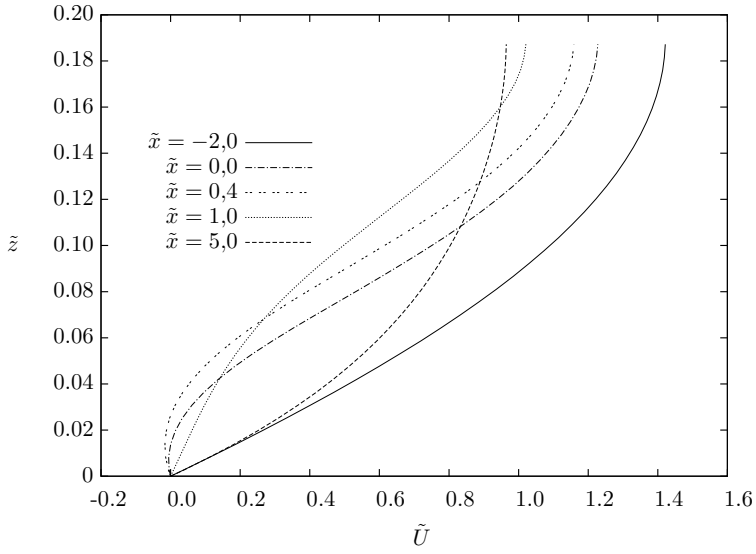

Figure 3.29: $\tilde{U}$-velocity component as a function of $\tilde{z}$ at $\tilde{y} = 0$ for different axial positions. $Re = 1000$ and $Q = 1.2$.

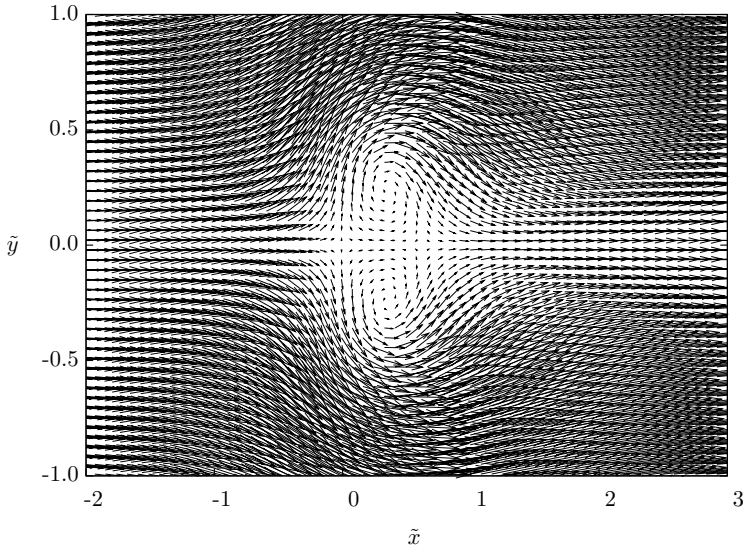

Figure 3.30: Velocity vector field in the $\tilde{x} - \tilde{y}$ plane for $Re = 1000$ and $Q = 1.2$, at $\tilde{z} = 0.014$, velocity components are scaled by a factor of 2.

The lateral view of the velocity field at the mid $\tilde{x} - \tilde{z}$ plane ($\tilde{y} = 0$), is shown in Figure 3.31. It is clearly observed that the flow perturbation caused by the magnetic obstacle reaches almost the free surface of the fluid layer. Further, in the magnetic obstacle region close to the bottom wall, a small recirculation is found. This recirculation grows and intensifies as the Q parameter takes larger values. For the sake of comparison, the velocity field in this plane is shown in Figure 3.32 for the same Reynolds number but $Q = 1.7$. The appearance of the recirculation may be related with the flow separation. In this context, the present physical situation resemblances a retarded flow produced by a localized adverse pressure gradient that creates a point of inflection of the velocity profile (see Figure 3.29). In fact, in the main flow direction the pressure increases and drops in a very short distance. The point of inflection, characterized by the condition $\partial^2 U/\partial \tilde{z}^2 = 0$, has important consequences for the flow separation (Schlichting and Gertsen 2000). In fact, in the separation point, the velocity profile must have a point of inflection and, therefore, separation can only occur when the flow is retarded (due to an adverse pressure gradient).

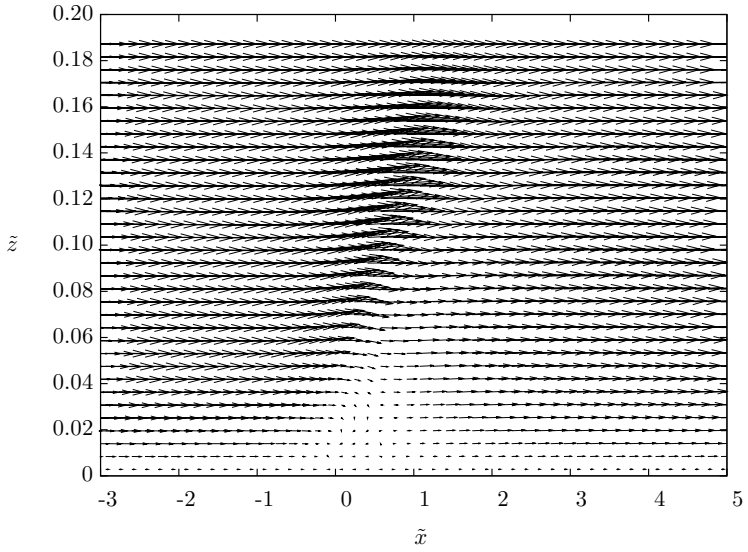

Figure 3.31: Velocity field in the mid $\tilde{x} - \tilde{z}$ plane ($\tilde{y} = 0$) for $Re = 1000$ and $Q = 1.2$.

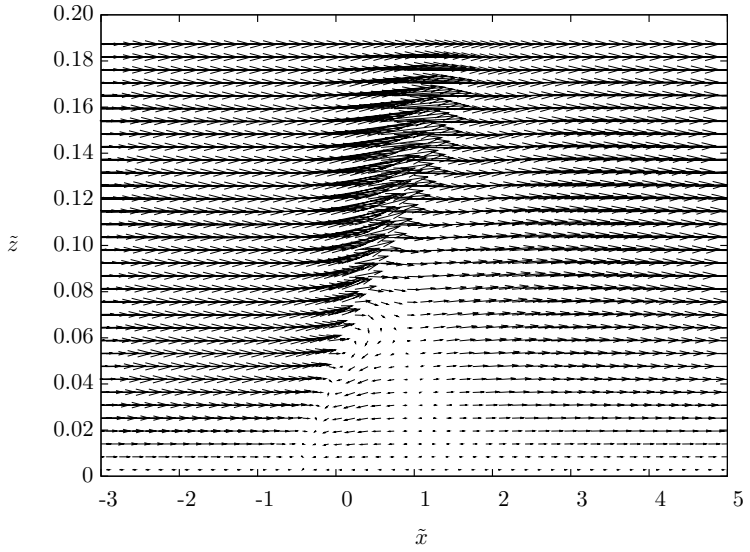

Figure 3.32: Velocity field in the mid $\tilde{x} - \tilde{z}$ plane ($\tilde{y} = 0$) for $Re = 1000$ and $Q = 1.7$.

Figure 3.33 shows the velocity field in the cross-stream vertical $\tilde{y} - \tilde{z}$ plane at $\tilde{x} = 0.4$. The symmetric flow pattern is very similar to the one observed in the previous case (see Figure 3.28) although the intensity of the flow is stronger.

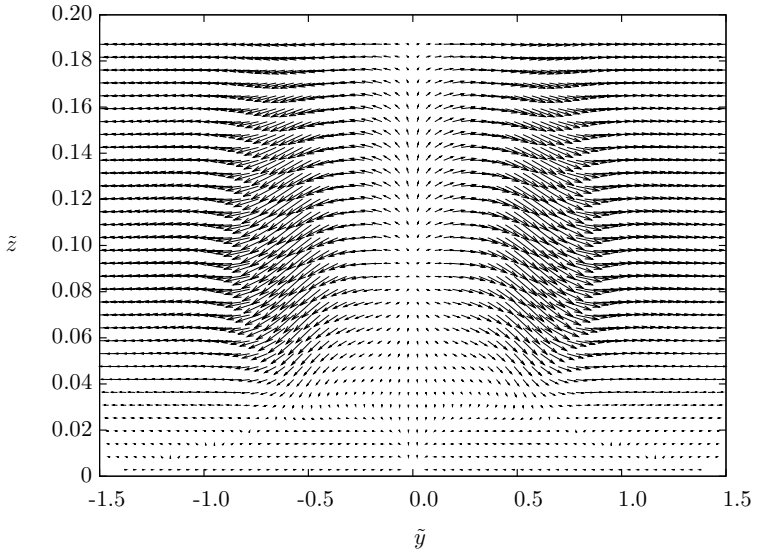

Figure 3.33: Velocity field in the $\tilde{y} - \tilde{z}$ plane $(\tilde{x} = 0.4)$ for $Re = 1000$ and $Q = 1.2$.

Case III. $Re = 1000$**,** $Q = 10$

This case presents a characteristic flow pattern of periodic vortex shedding calculated from 3D numerical simulation. For the reported experimental value $Q = 1.7$ ((Honji and Haraguchi 1995)), numerical calculations do not predict periodic vortex shedding. Vortex shedding, detected at characteristic points through the time-harmonic oscillation of a component of vorticity, was found numerically for Q values as small as 10. All the velocity profiles ($\tilde{U}$ vs. $\tilde{z}$) shown in Figure 3.34), present inflection points and show very large negative velocity values at all the axial positions in the neighborhood of the obstacle, except one ($\tilde{x} = -2.0$). This indicates a wide zone of flow recirculation which is corroborated in Figure 3.35, where the velocity field in the horizontal $\tilde{x} - \tilde{y}$ plane at $z = 0.08$ is shown at a given time.

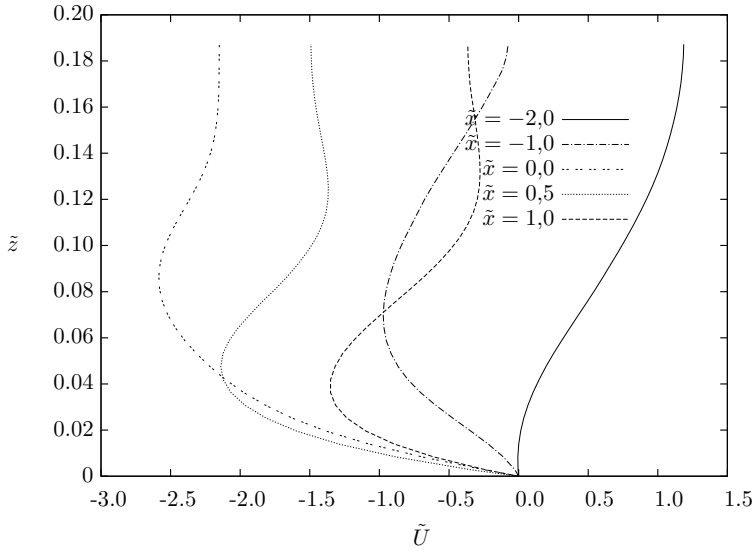

Figure 3.34: $\tilde{U}$-velocity component as function of $\tilde{z}$ for $Re = 1000$ and $Q = 10.0$ at $\tilde{y} = 0$.

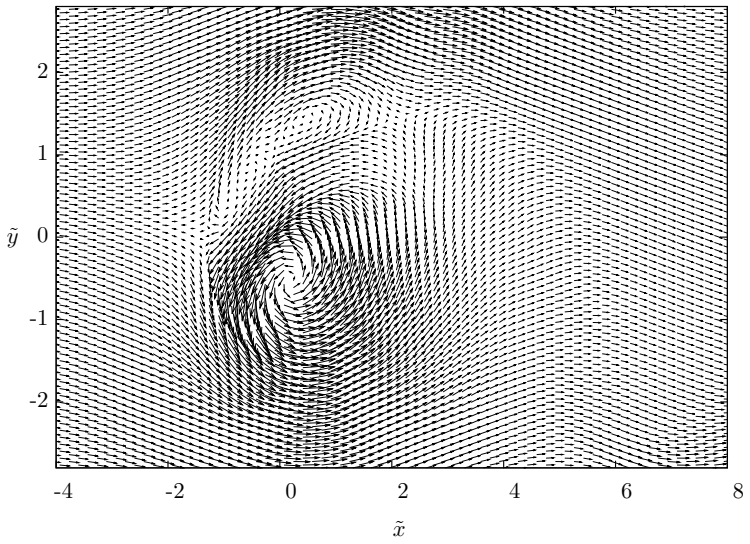

Figure 3.35: Instantaneous velocity field in the $\tilde{x} - \tilde{y}$ plane ($\tilde{z} = 0.08$) for $Re = 1000$ and $Q = 10$. Velocity components are scaled by a factor of 0.15

The lateral view of the velocity profile at the mid $\tilde{x} - \tilde{z}$ plane reveals the strong perturbation caused by the magnetic obstacle in the whole layer thickness. The complex recirculation time-dependent pattern indicates an unstable flow behavior. The large velocities near the free surface call the attention on the range of validity, as Q is increased, of the stress-free boundary condition imposed on the free surface.

Finally, Figure 3.37 shows the instantaneous velocity field at the cross-stream vertical plane $\tilde{x} = -1.3$. The symmetry of the flow observed in the previous cases is completely lost due to the vortex shedding.

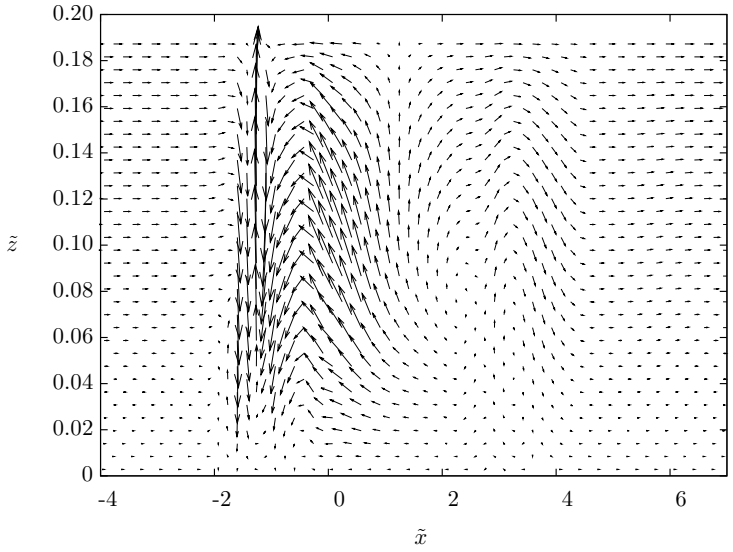

Figure 3.36: Instantaneous velocity field in the $\tilde{x}-\tilde{z}$ plane ($\tilde{y} = 0$) for $Re = 1000$ and $Q = 10$. Velocities components are scaled by a factor of 0.1.

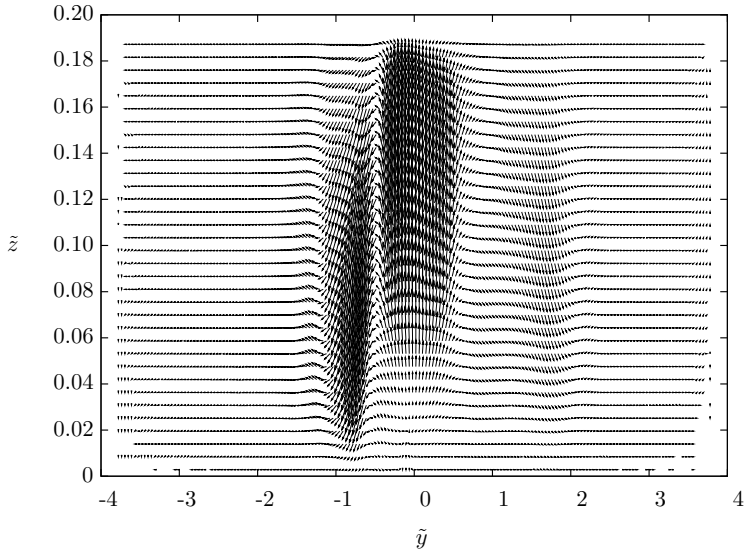

Figure 3.37: Instantaneous velocity field in the $\tilde{y} - \tilde{z}$ plane ($\tilde{x} = -1.3$) for $Re = 1000$ and $Q = 10$. Velocities components are scaled by a factor of 0.05.

Previous 3D numerical results show that for a sufficiently high Re, the flow of an electrolyte past a magnetic obstacle can present complex flow structures as the Lorentz force parameter Q is increased. Some of these structures have been presented here for the first time although a more extense study is required to characterize the transition between different flow regimes and, particularly, to determine the stability properties of the flow.

Part of the results in this chapter have been published in

- Beltrán A., Cuevas S., Smolentsev S. "Instabilities in the flow past localized magnetic fields". Second International Symposium on Instability and Bifurcations in Fluid Dynamics. Journal of Physics: Conference Series 64 (2007) 012009.

- Ramos E., Beltrán A., Cuevas S. and Smolentsev, S. "Dynamic properties of a magnetic obstacle", Proceedings of the 7th International pamir Conference on Fundamental and applied MHD, Presqu'île de Giens, France, September 8-12, Vol. 2, pp. 891-895, (2008).

and presented in

- Beltrán, A., Cuevas, S. and Smolentsev, S. - "Instabilities in the flow past localized magnetic fields". Presented at the *COST Action P17 Summer School on Instabilities and Turbulence in MHD Flows*. 26 June-1 July 2006, Coventry, UK.

- Beltrán, A., Cuevas, S., and Smolentsev, S. -"Instabilities in the flow past localized magnetic fields". Presented at *The Second International Symposium on Instabilities and Bifurcations in Fluid Dynamics*. August 15-18, 2006, Copenague, Denmark.

- Cuevas, S., Beltrán, A. and Ramos, E. "Stability of the flow past a magnetic obstacle". Presented at *The 61st Annual Meeting of the Division of Fluid Dynamics of the American Physical Society*. November 23-25, 2008, San Antonio, Texas, USA.

- Beltrán, A. and Cuevas, S. "Instabilities in flows past localized magnetic fields". Presented at the *XII Congress of the Division of Fluids and Plasmas, Mexican Physical Society*. October 16-19, 2006, San Luis Potosí, S.L.P., Mexico.

Chapter 4

Oscillatory Magnetic Obstacle

In this chapter, we consider a new physical situation that involves the generation of vortical structures in a conducting fluid layer produced by the harmonic motion of a localized magnetic field (i.e. magnetic obstacle). We analyze the flow induced by an oscillatory magnetic obstacle in two different situations. First, we consider a layer of conducting fluid in the absence of injected currents so that the flow patterns are due exclusively to the interaction of induced currents with the applied oscillating field. In these conditions, the flow generation involve Hartmann numbers that are not easy to reach with electrolytes and permanent magnets. The analysis is then performed through numerical simulations assuming a purely 2D LM flow. The flow transitions occuring between two different stages in the oscillating cycle are analyzed using a technique based on the identification and evolution of the critical points (Ouellette and Gollub 2007) that affords a simple geometrical way of describing and characterizing complex flows. In the second case, we analyze experimentally and numerically the flow produced by an oscillatory magnetic obstacle in a thin electrolytic layer when a D.C. current is injected in a direction parallel to the axis of oscillation of the magnetic field. For a restricted frequency range, the flow generated in the neighborhood of the magnet forms local vortical structures that are shed periodically along the main direction of the Lorentz force. Results show that Lorentz forces created by injected and induced currents interacting with a harmonically oscillating localized field are able to destabilize the flow and enhance the stirring.

4.1 Oscillating magnetic obstacle in a liquid metal layer

Although quite remarkable differences exist between flows past solid and magnetic obstacles, to consider electromagnetic analogies of physical situations where solid-fluid interactions lead to interesting flow patterns, may be worth exploring. That is the case, for instance, of bluff bodies in oscillatory motion within viscous fluids (Riley 2001). The analysis of the magnetic analogue, namely, the flow produced when a magnetic obstacle oscillates in a quiescent conducting fluid layer, is the aim of the present study. Some aspects of motion generated by an oscillating magnetic obstacle were briefly described in Beltrán et al. (2009).

The two-dimensional flow induced by an oscillatory magnetic obstacle is analyzed using a technique based on the identification and evolution of the instantaneous critical points. The role of the critical points for identifying structures in fluid flows has been acknowledged at least since Legendre (1956). See also Perry and Fairlie (1974) for a review of early work in this field. More recently, the role of critical points in complex and turbulent flows has been a focus of attention (Rossi et al. 2006a, Rossi et al. 2006b, Goto et al. 2005). We will employ an efficient technique based on streamline curvature proposed by Ouellette and Gollub (2007) to locate critical points.

In the present case, the harmonic motion of the magnetic obstacle generates a time-periodic localized Lorentz force that creates a vortex dipole flow that switches the direction of rotation twice per cycle. The transition between these rotation states takes place in a rather short time interval and involves the creation of elliptic and hyperbolic critical points. The particular flow topology of this transition depends on the oscillation frequency and, as it increases, bifurcations of the streamline patterns are observed, leading to more complex flow structures. The flow dynamics is analyzed numerically in order to obtain a bifurcation map that captures the topology of the flow transitions. Using a nonlinear theory, the numerical approach is complemented with a theoretical bifurcation analysis, based on the local analysis of the streamline patterns, that provides a qualitative description of the flow.

Nonuniform Lorentz forces produced by induced currents interacting with the oscillating magnetic field create periodic laminar flow patterns that can be characterized by three parameters: the oscillation Reynolds number, Re_ω, the Hartmann number, Ha and the dimensionless amplitude of the magnetic obstacle oscillation, D. Also, a theoretical model based on a local analysis that predicts most of the qualitative properties calculated numerically is proposed. The analysis is restricted to oscillations of small amplitude and $Ha = 100$. The resulting flow patterns are described and interpreted in terms of position and evolution of the critical points of the instantaneous streamlines. It is found that in most of the cycle, the flow is dominated by a pair of counter rotating vortices that switch their direction of rotation twice per cycle. The

transformation of the flow field in the first part of the cycle into the pattern displayed in the second half, occurs via the generation of hyperbolic and elliptic critical points. The numerical solution of the flow indicates that for low frequencies (v.e. $Re_\omega = 1$), two elliptic and two hyperbolic points are generated, while for high frequencies (v.e. $Re_\omega = 100$), a more complex topology involving four elliptic and two hyperbolic points appear. The bifurcation map for critical points of the instantaneous streamline is obtained numerically, also a theoretical model based on a local analysis that predicts most of the qualitative properties calculated numerically is proposed.

4.1.1 Formulation

Consider a two-dimensional quiescent layer of an electrically conducting, incompressible viscous fluid in the $\tilde{x}-\tilde{y}$ plane in presence of a spatially localized magnetic field $\mathbf{B}^0$, the B_z^0 component, is again the only one considered. The oscillatory motion of the applied field induces electric currents in the fluid that interact with the imposed magnetic field and produce a periodic non-homogeneous Lorentz force that stirs the fluid and creates vorticity. The dimensionless equations that govern the flow dynamics are:

$$\frac{\partial \tilde{U}}{\partial \tilde{x}} + \frac{\partial \tilde{V}}{\partial \tilde{y}} = 0, \tag{4.1}$$

$$Re_\omega \frac{\partial \tilde{U}}{\partial \tilde{t}} + \tilde{U}\frac{\partial \tilde{U}}{\partial \tilde{x}} + \tilde{V}\frac{\partial \tilde{U}}{\partial \tilde{y}} = -\frac{\partial \tilde{P}}{\partial \tilde{x}} + \nabla_\perp^2 \tilde{U} + Ha^2 \tilde{j}_y \mathcal{B}_z^0, \tag{4.2}$$

$$Re_\omega \frac{\partial \tilde{V}}{\partial \tilde{t}} + \tilde{U}\frac{\partial \tilde{V}}{\partial \tilde{x}} + \tilde{V}\frac{\partial \tilde{V}}{\partial \tilde{y}} = -\frac{\partial \tilde{P}}{\partial \tilde{y}} + \nabla_\perp^2 \tilde{V} - \frac{Ha^2}{Re} \tilde{j}_x \mathcal{B}_z^0, \tag{4.3}$$

where t is normalized by the forced frequency of oscillation ω. The new dimensionless parameter is the oscillation Reynolds number, $Re_\omega = \omega L^2/\nu$.

In addition, the induction equation for this case reduces to

$$\nabla_\perp^2 \tilde{b}_z - \tilde{U}\frac{\partial B_z^0}{\partial \tilde{x}} - \tilde{V}\frac{\partial B_z^0}{\partial \tilde{y}} = Re_\omega \frac{\partial B_z^0}{\partial t}, \tag{4.4}$$

The harmonic motion of the external magnet is described by the equation

$$\tilde{x}(t) = D\sin(t), \tag{4.5}$$

where $D = A/L$ is a geometrical parameter defined as the ratio of the amplitude of the oscillation, A, and the characteristic length scale.

We assume that the induced field is zero at a long enough, finite distance from the source of the applied field. Therefore, we impose the condition that the single component of the induced field vanishes at all boundaries. We look for numerical

solutions using a formulation based on the primitive variables, the velocity and pressure, and the induced magnetic field as electromagnetic variable. The integration region is a square of 25×25 units (measured in terms of the characteristic length L). The magnetic obstacle oscillates around the geometrical center of the square in the $\tilde{x}$-direction. A finite difference method on an orthogonal equidistant grid of 636×636 was used to solve the governing equations (3.2-4.4), assuming a motionless fluid as initial condition and no-slip boundary conditions for the velocity components ($\tilde{U} = \tilde{V} = 0$) at all boundaries.

The analysis of the flow is based on the identification of critical points of the instantaneous streamlines that are generated in each cycle. In order to find the position and geometrical characteristics of the critical points as functions of time, we follow the methodology presented by Ouellette and Gollub (2007) and Braun et al. (2006), which consists in determining the curvature fields of the instantaneous streamlines, and identifying the high curvature isolated points as critical hyperbolic or elliptic points of the flow. As explained in Ouellette and Gollub (2007), near the critical points, the direction of fluid particle trajectories changes over short length scales. Therefore, it is expected that local maxima of curvature correspond to topologically special points of the flow. The nature of the critical points is found using the Okubo-Weiss (OW) criterion in two dimensions (Weiss 1992). In a region dominated by rotation (elliptical critical point), the enstrophy is larger than the squared strain rate and the OW parameter is positive. In contrast, if the local deformation dominates the flow in a small region, the OW parameter is negative indicating that the critical point is hyperbolic.

Two symmetries can be identified in the flow. First, given that the magnetic obstacle moves along the horizontal direction, and that the structure of the magnetic field is symmetric with respect to the same line, we have mirror symmetry with respect to the $\tilde{y}$ coordinate, *i.e.*

$$\begin{aligned} \tilde{U}(\tilde{x}, \tilde{y}, \phi) &= \tilde{U}(\tilde{x}, -\tilde{y}, \phi), \\ \tilde{V}(\tilde{x}, \tilde{y}, \phi) &= -\tilde{V}(\tilde{x}, -\tilde{y}, \phi). \end{aligned} \tag{4.6}$$

Second, after transients have died out, we have a cyclic symmetry in the flow such that the velocity field transforms according to the following reflection around the horizontal axis,

$$\begin{aligned} \tilde{U}(\tilde{x}, \tilde{y}, \phi) &\rightarrow -\tilde{U}(-\tilde{x}, \tilde{y}, \phi - \pi), \\ \tilde{V}(\tilde{x}, \tilde{y}, \phi) &\rightarrow \tilde{V}(-\tilde{x}, \tilde{y}, \phi - \pi). \end{aligned} \tag{4.7}$$

4.1.2 Numerical results

Since the most interesting flow dynamics is observed as the oscillation frequency changes, the range of oscillation Reynolds numbers explored is from 1 to 100. In turn, the Hartmann number is fixed to a sufficiently high value ($Ha = 100$) so that MHD effects become relevant. Likewise, the dimensionless amplitude of oscillation of the localized magnetic field is fixed at $D = 0.01$. The flow displayed a transient state that lasted 50 cycles. All results shown in this section correspond to long times after the onset of the motion, once the transient effects have died out. At long times, the motion is periodic and will be described as a function of the phase ($-\pi < \phi < \pi$) in the cycle.

Low oscillation frequencies ($Re_\omega = 1$)

With $Re_\omega = 1$, the dominant pattern of the flow generated by the oscillatory, localized magnetic field is a dipole-type flow composed of two counter rotating vortices located symmetrically above and below the average position of the imposed magnetic field. Dipole vortices can also be observed when a uniform flow passes through a non-oscillating magnetic obstacle, as discussed in Cuevas et al. (2006a). These patterns are characteristic of flows generated by point momentum sources (Afanasyev and Korabel 2004). It is found that the direction of rotation of the dipole vortex is reversed twice per cycle, in such a way that each direction of rotation lasts half cycle. The value $\phi = 0$ is defined as the time where the magnet is at the point $(\tilde{x} = 0, \tilde{y} = 0)$.

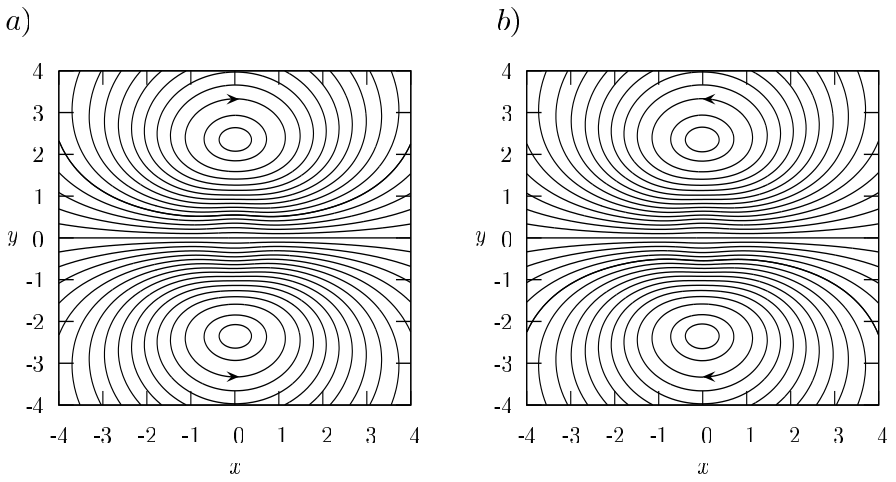

Figure 4.1: Instantaneous streamlines for $D = 0.01$, $Ha = 100$ and $Re_\omega = 1$: a) $\phi = -997\pi/1000$, b) $\phi = 3\pi/1000$. The magnetic obstacle is in the region $-0.5 < \tilde{x} < 0.5$ and $-0.5 < \tilde{y} < 0.5$.

In Figure 4.1 we show instantaneous streamlines for flows with a relative phase of π illustrating the symmetry described in equation (4.7). The topological changes leading to the reversal of the vortices are shown in Figure 4.2. At $\phi = -927\pi/1000$ (Figure 4.2a), the flow distribution is similar to that observed at $\phi = -997\pi/1000$ (See Figure 4.1a), but with the instantaneous streamlines slightly perturbed near the average position of the magnet ($\tilde{x} = 0, \tilde{y} = 0$). Then, at $\phi = -895\pi/1000$ (Figure 4.2b), a different picture is observed where four new critical points clustered near the origin appear. Two symmetric elliptic points are located vertically displaced above and below the origin; the direction of rotation of the fluid around these elliptic points is opposite to that of the vortical structures created in the previous half-cycle. Two hyperbolic points appear along the horizontal axis one at each side of the center of coordinates. The two hyperbolic critical points are linked by two heteroclinic invariant manifolds that form a separatrix with isolated regions around the recently formed elliptical points. The topology of the flow pattern is similar at a later phase ($\phi = -831\pi/1000$) as can be seen in (Figure 4.2c) but the scale of the distribution of the critical points located around the center is enlarged. The original vortices generated in the previous cycle are pushed away from the center by the emerging structures and tend to dissipate due to viscous effects. The final stage of the flow evolution is displayed in Figure 4.2d ($\phi = -752\pi/1000$) where the hyperbolic points and the vortex pair formed in the previous cycle are almost out of the region shown in the figure and the vortex pair with opposite sense of rotation prevail. This cycle is repeated when the oscillating

magnet changes its direction of motion. The thresholds where a new counter rotating vortex pair is created are $\phi_0 = -896\pi/1000$ and $\phi_0 = 104\pi/1000$.

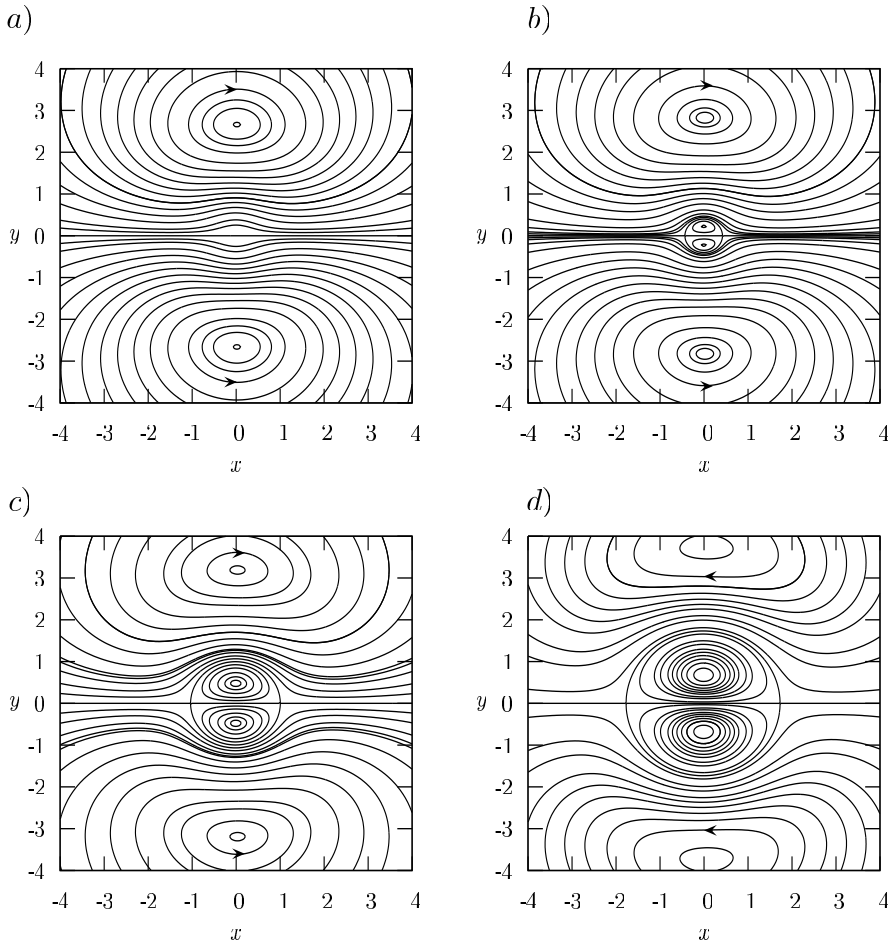

Figure 4.2: Instantaneous streamlines for $D = 0.01$, $Ha = 100$ and $Re_\omega = 1$: a) $\phi = -927\pi/1000$, b) $\phi = -895\pi/1000$, c) $\phi = -831\pi/1000$, d) $\phi = -752\pi/1000$.

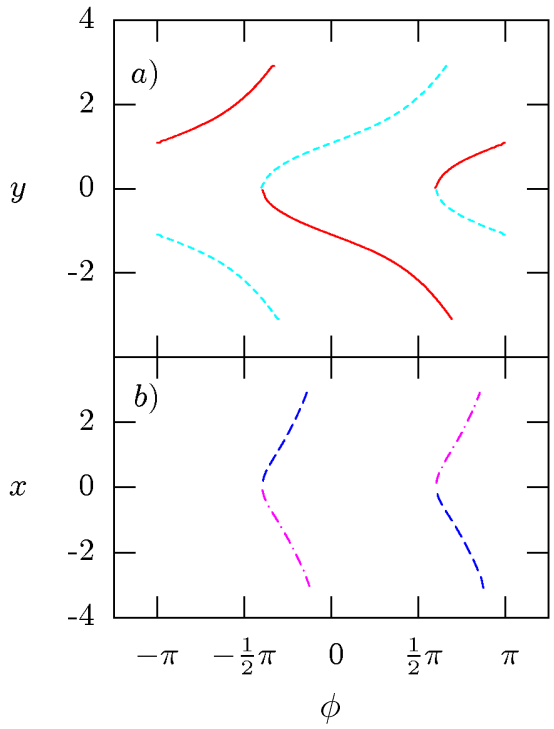

Figure 4.3: Position of critical points of the instantaneous streamlines for $D = 0.01$, $Ha = 100$ and $Re_\omega = 1$: a) $\tilde{y}$-position of elliptical points, and b) $\tilde{x}$-position of hyperbolic points, as functions of the phase ϕ. Red and blue lines refer to vortices rotating clockwise and counter-clockwise, respectively.

Figure 4.3 shows the evolution of the $\tilde{x}$- and $\tilde{y}$-position of the critical points of the instantaneous streamlines as functions of time phase. We follow a pair of each elliptic and hyperbolic points that are cyclically generated, and move away from the average position of the magnet in the $\tilde{y}$- and $\tilde{x}$-directions respectively. The initial and final velocities of the elliptical points are larger just after ϕ_o=$-896\pi/1000$ and $104\pi/1000$. The velocity of the hyperbolic points is practically constant for the whole cycle.

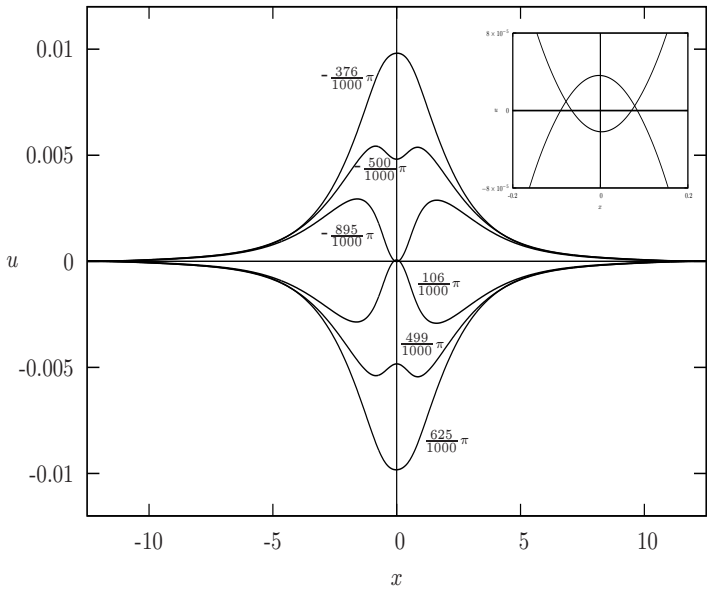

Figure 4.4: $\tilde{U}$-velocity component as a function of the axial coordinate $\tilde{x}$ for $\tilde{y} = 0$ for $Re_\omega = 1$. Labels near the lines indicate their phase in the cycle. The inset shows an amplification of the region close to the origin.

The genesis of the critical points can be traced to the behavior of the axial velocity as a function of time $\tilde{U}(t)$ at the horizontal line $\tilde{y} = 0$. At this line, the vertical velocity is zero due to the symmetry of the flow and the axial velocity evolves in time according to the profiles shown in Figure 4.4. At $\phi = -376\pi/1000$ the velocity profile displays a single local maximum at approximately $\tilde{x} = 0$. At subsequent times, the absolute value of the velocity becomes smaller and its distribution gradually develops a local minimum. This trend continues up to a time when the velocity distribution touches tangentially the $\tilde{U} = 0$ line indicating that a critical point appears close to the origin. At this time, the local maximum is the largest. At subsequent time instants, the velocity distribution crosses the $\tilde{U} = 0$ line at two points (located nearly symmetric around the origin) as can be appreciated in the inset of Figure 4.4. These points correspond to the hyperbolic critical points shown in Figure 4.2b-d. The small asymmetry displayed in the inset is generated by the fact that the flow moves in opposite directions for positive and negative phases respectively..

High oscillation frequencies ($Re_\omega = 100$)

For $Re_\omega = 100$ and $Ha = 100$, the qualitative flow features in most of the cycle are similar to those described in the previous paragraphs for $Re_\omega = 1$. Specifically, the flow is dominated by two counter-rotating vortices that switch directions of rotation twice per cycle. As in the previous example, the phase is referred to the motion of the magnet, with $\phi = 0$ at the moment when the magnetic obstacle is at $(\tilde{x} = 0, \tilde{y} = 0)$ and has maximum velocity.

However, for high Re_ω, the transformation is more complex and at a smaller scale as can be appreciated in Figures 4.5-4.7. When the phase is close to $-553\pi/1000$, the speed of the flow is reduced at two points located on the horizontal axis and at the sides of the origin; eventually, two clusters of critical points with the same distributions as those found for $Re_\omega = 1$, i.e., four elliptical and four hyperbolic points, are formed inside the area covered by the magnetized zone. This distribution of critical points was not observed in the case $Re_\omega = 1$. The initial steps in the transition are illustrated in Figures 4.5a,b. At $\phi = -542\pi/1000$ and for a short time interval smaller than $5\pi/1000$, the two sets of critical points are clearly separated with a small interval of the horizontal axis where the transversal velocity is very close to zero. This situation is illustrated in Fig. 4.5b. As will be discussed in more detail below, in fact, the two recirculation zones do not appear simultaneously. A detailed analysis shows that the rightmost appears first, but only a very short time interval follows before the other is created. See the inset of Figure 4.6 and the discussion of Figure 4.7. Shortly after they are formed, the two clusters move toward each other and merge to form structures of two elliptic points with an hyperbolic point in between, that move away from the $\tilde{y} = 0$ line as illustrated in Figure 4.5c. The two hyperbolic points located further away from the origin in Figure 4.5b move along the horizontal line. The last qualitative step in the evolution occurs when the two elliptic points and one hyperbolic point in each cluster combine to form a single elliptic point, suppressing the hyperbolic point. This configuration is topologically equivalent to that shown in Figure 4.5a, but the rotation direction is reversed. The instantaneous velocity profiles shown in Figure 4.6 indicate the history of the formation of the critical points. Just as it was described in the case for smaller oscillatory Reynolds number, the asymmetry of the extrema of the curves that is more clearly shown in the inset of the figure is originated because the magnetic obstacle moves in opposite directions in each half-cycle. The fact that the flow is slightly asymmetric with respect to the vertical line $\tilde{x} = 0$, indicates that there should be a phase interval (which might be very small) where there is only one cluster of two hyperbolic and two parabolic points located off the point ($\tilde{x} = 0$, $\tilde{y} = 0$). This situation is neatly illustrated in Figure 4.7 where the instantaneous streamlines that correspond to $\phi = 469\pi/1000$ are shown. According to the inset of Figure 4.6, at this phase, only one maximum has passed through the line $\tilde{U} = 0$ and then only one set of

two elliptic and two hyperbolic points, located at the left side of point $(\tilde{x}, \tilde{y}) = (0, 0)$ are present.

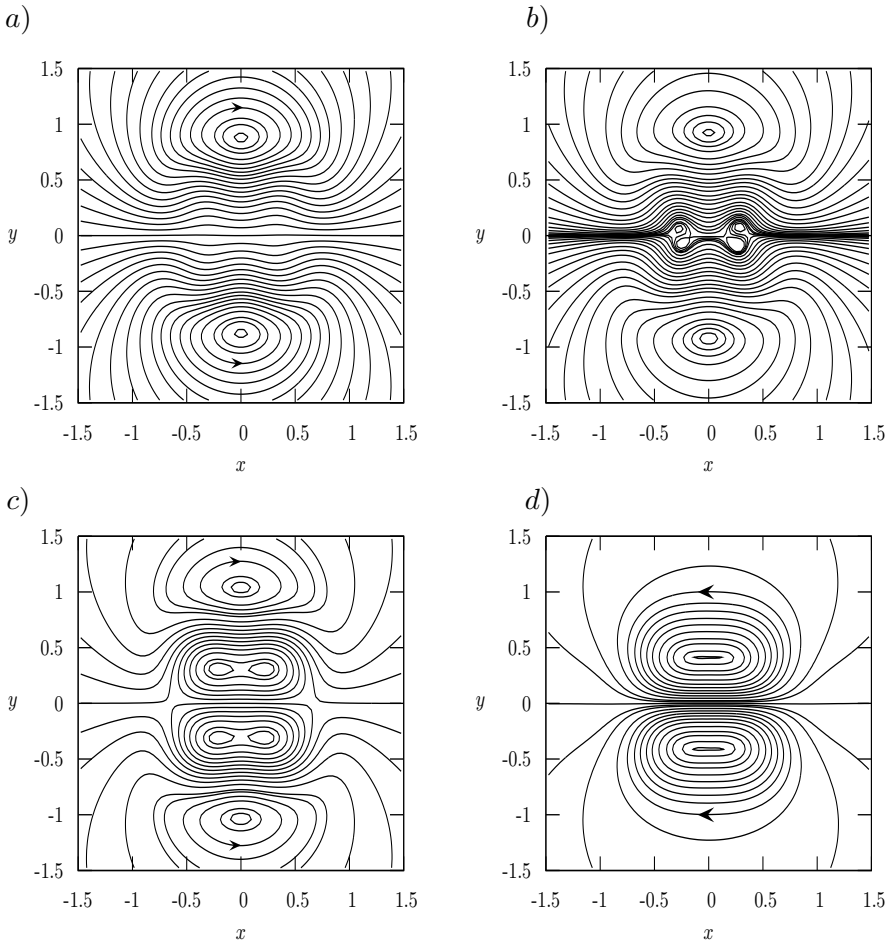

Figure 4.5: Instantaneous streamlines for $D = 0.01$, $Ha = 100$ and $Re_\omega = 100$: a) $\phi = -553\pi/1000$, b) $\phi = -542\pi/1000$, c) $\phi = -534\pi/1000$, d) $\phi = -489\pi/1000$.

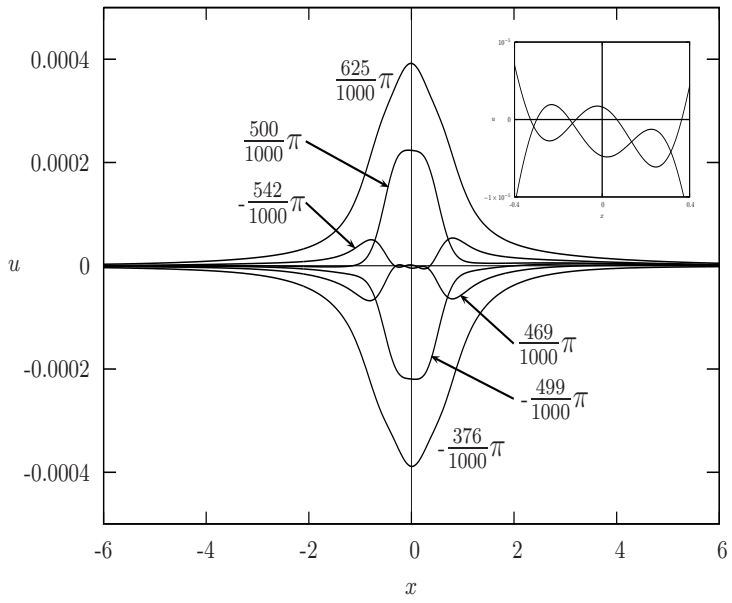

Figure 4.6: u-velocity component as a function of the axial coordinate $\tilde{x}$ for $\tilde{y} = 0$ for $Re_\omega = 100$. Labels near the lines indicate their phase in the cycle. The inset shows an amplification of the region close to the origin.

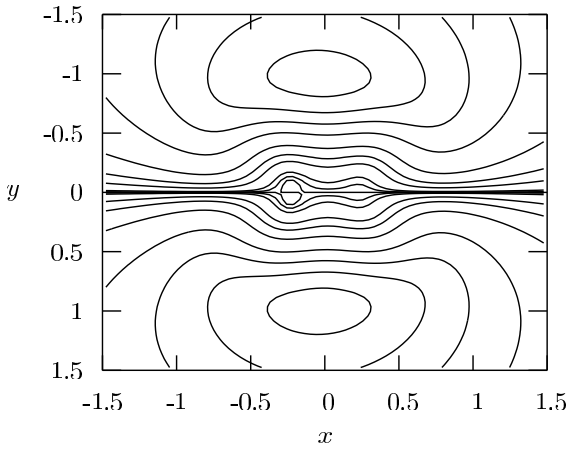

Figure 4.7: Instantaneous streamlines for $D = 0.01$, $Ha = 100$ and $Re_\omega = 100$ and $\phi = 469\pi/1000$.

4.1.3 Bifurcation map

The Re_ω-ϕ bifurcation map of qualitative behavior is shown in Figure 4.8. The inset in the figure shows the region $-0.59\pi < \phi < -0.51\pi$ in greater detail. The symbols represent actual calculations and the lines separate regions with different qualitative flow patterns. The plane is divided into five regions. In the region above the line I there are no critical points in the immediate vicinity of the origin. In a larger region critical points are present in the flow, with those closest to the origin forming a vortex pair as in Figure 4.1a. As line I is crossed, a pair of counter rotating vortices are created. An example of the flow is given in Figure 4.2b. Line I passes through the point $Re_\omega = 1$, $\phi = -896\pi/1000$, which is consistent with Figure 4.2. Above $Re_\omega = 50$, the flow transition is more complicated. The leftmost line in the inset is labeled with symbols I and II, since the scale of the plot prevents us from resolving the two lines that separate an extremely narrow region where only one set of two pairs of two elliptic and two hyperbolic points are present. See Figure 4.7. In the region between lines I and III, a pair of clusters of two elliptic and two hyperbolic points separated by a region of stagnant fluid are observed as illustrated in Figure 4.5b. The flow in the region between lines III and IV, is characterized by the two pairs of two elliptic points separated by the homoclinic orbit of a hyperbolic point. Each of these structures are located above and below the horizontal line. An example of this flow is shown in Figure 4.5c. Finally, line IV separates regions with and without homoclinic orbits.

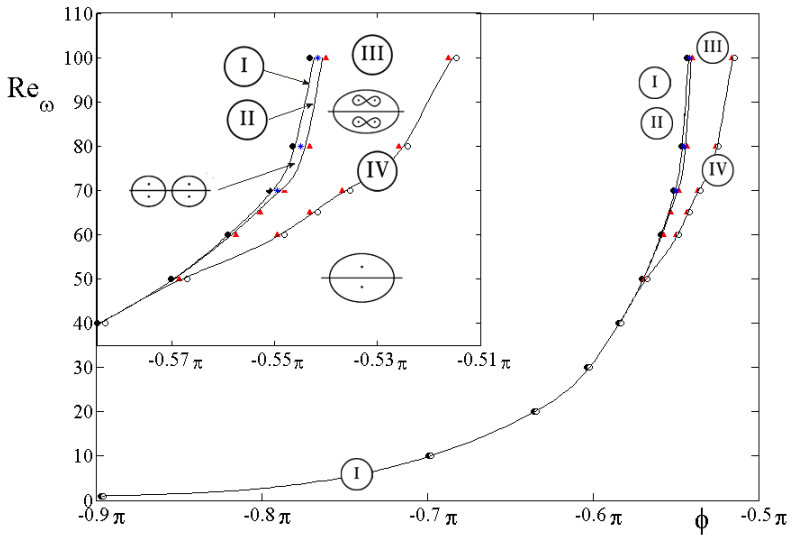

Figure 4.8: Bifurcation diagram for critical points of the instantaneous streamlines. Representative examples of flows are shown in Figures 4.2 and 4.5.

4.2 Theoretical bifurcation analysis

A local analysis of the streamline patterns near the symmetry line $\tilde{y} = 0$ can be performed with the use of a normal form of the velocity field, i.e., a simplification of the field which nevertheless gives a qualitatively correct picture of the streamline pattern (Bakker. 1991,Brøns 2007).

For the present flow, the velocity field can be expanded in a Taylor series in $\tilde{y}$,

$$\begin{aligned} u &= u_0(x) + u_2(x)y^2 + u_4(x)y^4 + \cdots, \\ v &= -y(u_0'(x) + \frac{1}{3}u_2'(x)y^2 + \frac{1}{5}u_4'(x)y^4 + \cdots), \end{aligned} \tag{4.8}$$

where

$$u_k(x) = \frac{1}{k!}\frac{\partial^k u}{\partial x^k}(x, 0). \tag{4.9}$$

Only even-order terms of $\tilde{y}$ appear in $\tilde{U}$ due to the mirror-symmetry of the velocity field in the line $\tilde{y} = 0$. See equation (4.6). The expression for $\tilde{V}$ follows from $\tilde{U}$ using the equation of continuity.

The topology of the streamlines is in general given by the lowest-order terms of the velocity field. The lowest order term in $\tilde{U}$ including both $\tilde{x}$ and $\tilde{y}$ is $\tilde{U}_2(\tilde{x})\tilde{y}^2$, and assuming the non-degeneracy condition that this term does not vanish, we drop terms of higher order and replace $\tilde{U}_2(\tilde{x})$ by a constant, which, after an appropriate scaling, can be chosen as 1.

The line $\tilde{y} = 0$ is a streamline and the velocity here is given by $\tilde{U}_0(\tilde{x})$. We approximate this by a polynomial

$$u_0(x) = c_0 + c_1 x + c_2 x^2 + \cdots + c_{n-2} x^{n-2} + \frac{1}{n} x^n. \tag{4.10}$$

The truncation order n is determined by the maximal number of stagnation points that can occur in the specific flow. Again, the value $1/n$ is obtained by an appropriate scaling. In the present case, the relevant choice is $n = 4$, as discussed in section 4.1.2, we observe up to four critical points on $\tilde{y} = 0$. See also Figs. 4.5 and 4.6. The term of degree $n - 1$ is omitted, since it can be removed by a translation of the origin.

Hence, we consider the normal form for the equations for the streamlines

$$\begin{aligned} \dot{x} &= u = u_0(x) + y^2, \\ \dot{y} &= v = -y u_0'(x). \end{aligned} \tag{4.11}$$

with $\tilde{U}_0$ given by Eq. (4.10) and the c_k being parameters. We note in passing that a rigorous derivation of this normal form can be obtained by perturbation methods following an approach previously used in similar situations (Bakker. 1991, Brøns 2007, Gurcan and Deliceoğlu. 2005, Brøns et al. 2007).

For $n = 4$ the bifurcation diagram is three-dimensional depending on the parameters c_0, c_1, c_2. Since the system Eqns. (4.11) is almost identical to the normal form for flow close to the axis in axisymmetric flow (Brøns 1999, Brøns 2007) the bifurcation analysis here immediately follows from that case. Here we summarize the results. The parameter space is divided by surfaces into regions with different flow topologies. Two of these surfaces are

$$\mathrm{R}_\pm: \quad c_1^2 = \left(\frac{2}{3}\right)^3 (-c_2 \pm \sqrt{\lambda})(2c_2 \pm \sqrt{\lambda})^2, \quad \lambda > 0, \tag{4.12}$$

where

$$\lambda = c_2^2 + 3c_0. \tag{4.13}$$

Intersecting R_+ a recirculation zone is created, and at R_- two such zones merge into a single one. At

$$\mathrm{S}: \quad c_1^2 = -4\left(\frac{2}{3}c_2\right)^3, \quad \lambda < 0, \tag{4.14}$$

a pair of critical points inside a recirculation zone are either created or destroyed.

The coefficients c_k depend on the physical parameters which in the present flow are Re_ω and ϕ. Hence, the bifurcation diagram in the (Re_ω, ϕ) plane is found from a two-dimensional slice in the (c_0, c_1, c_2) parameter space, giving rise to bifurcation curves where the slice intersects the bifurcation surfaces $\mathsf{R}_\pm$ and S. From the plots of $\tilde{U}_0(\tilde{x})$, it appears that this function is very close to being symmetric. See Figs. 4.4 and 4.6. One would expect this symmetry to be more pronounced as the speed of the magnets tends to zero and eventually disappear for high magnet velocities. The function $\tilde{u}_0(\tilde{x})$ is perfectly symmetric when $c_1 = 0$, and we hence expect that for the relevant slice $c_1(Re_\omega, \phi)$ takes small values. In Fig. 4.9 we show such a slice for a small, constant value of c_1. The two curves I and II are intersections with the bifurcation surface R_+, the curve III is the intersection with R_- and IV is the intersection with S. Three bifurcation curves emanate from a single point, denoted a *codimension-2* point. When $c_1 \to 0$, the point moves toward I, and I and II coincide in the limit $c_1 = 0$.

The physical bifurcation diagram in the (Re_w, ϕ) space is obtained from a smooth deformation of this diagram. The details will depend on the actual functional dependence between the physical and mathematical parameter which cannot be inferred from the present analysis. However, from a simple linear relation between the two sets of parameter a bifurcation diagram which is qualitative consistent with the numerical results can be obtained. If the (Re_ω, ϕ) coordinate system is located as indicated in Fig. 4.9, the two series of simulations at $Re_\omega = 1, 100$ intersect the bifurcation curves in agreement with Figs. 4.2 and 4.5. More detailed and quantitative information can be established from a rigorous perturbation approach (Brøns 2007). The point we want to stress here is that the analysis shows that the set of streamline topologies obtained numerically is expected to be complete, and, furthermore, there is a natural partition of the vortex creation into two kinds: Either Re_ω is below a certain threshold, and only a single pair of vortices occur or Re_ω is above that threshold, and the vortex creation has an intermediate step with two vortex pairs. The threshold is obtained for the value of Re_ω where the path passes through the codimension 2 point. From Fig. 4.8 this happens for Re_ω slightly below 50. The different flow topologies are shown in Fig. 4.9.

The numerical study shows that the flow is dominated by two counter rotating vortices with structure similar to the ones observed when a localized magnetic obstacle is in constant relative motion with respect to a thin layer of a conducting fluid like that described by Cuevas et al. (2006a). However, when the magnetic obstacle oscillates, the vortex pair changes its direction of rotation twice per cycle undergoing a flow transformation involving the interplay of critical points in the instantaneous streamlines that results in the flow reversal. In each cycle, two new pair of vortices are created and those generated previously are pushed away from the time average of the position of the magnetic obstacle. As a new vortex pair is created twice during a cycle, from a strict mathematical point of view, there would eventually be an infinite array

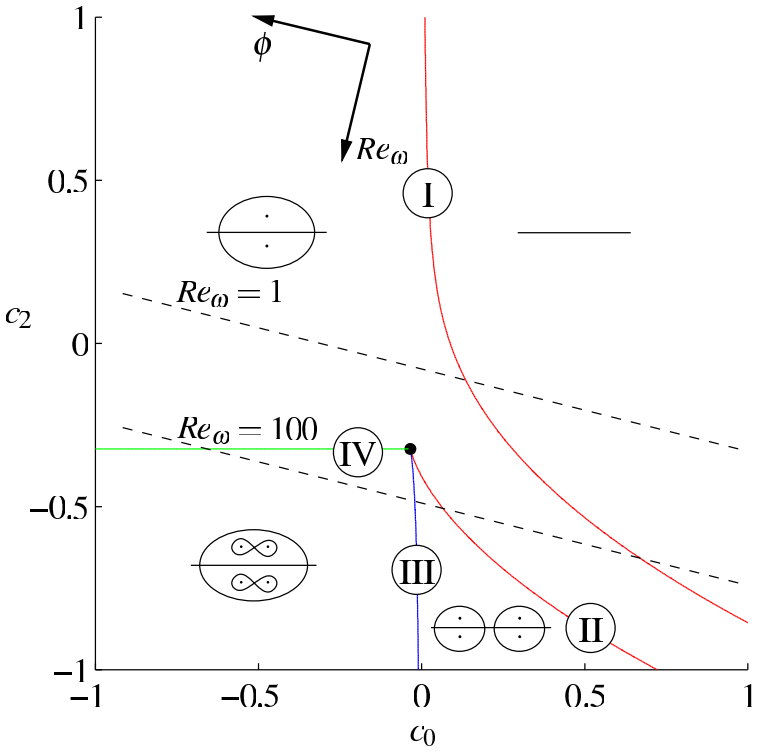

Figure 4.9: (Color online) Theoretical bifurcation diagram in the c_2, c_0 parameter plane for $c_1 = 0.2$. The dashed lines correspond to the sequences of topologies in Figs. 4.2 and 4.5.

of vortices in the flow and they do not actually disappear as they move away from the axis but only dissipate to a very low strength. Given the specificities of the motion of the magnetic obstacle that we have chosen to study, the flow generated by the induced Lorentz force displays a cyclic symmetry and a spatial symmetry which restricts the distribution of critical points in the flow. For larger oscillatory Reynolds numbers, the interplay of the sets of elliptic and hyperbolic critical points that appear near the time average position of the magnetic obstacle is increasingly complex as displayed in the map of qualitative behavior shown in Figure 4.8

4.3 Oscillating magnetic obstacle in an electrolytic layer

In this section [1], we present experimental results of the vortex flow in a thin electrolytic layer generated by the Lorentz force created by the magnetic field of a permanent magnet in oscillatory motion and an injected electric current parallel to the motion of the magnet. For a restricted frequency range, in the neighborhood of the magnetic obstacle local vortical structures are formed and shed periodically along the main direction of the applied Lorentz force. For details see Beltrán et al. (2009).

The experimental setup consists of a plexiglass rectangular frame of 28 cm $\times$ 38 cm $\times$ 1.6 cm, water-tight glued to a thin floated glass plate 0.2 cm thick to form a cell with large horizontal area and small depth. Copper electrodes are placed along the shorter sides of the cell and connected to an adjustable D.C. voltage power supply. A permanent cylindrical neodymium-iron-boron dipole magnet with a diameter of $d = 1.2$ cm and a maximum strength of 0.4 T at its surface, is located under the glass plate with its upper flat face at a distance smaller than 0.1 cm from the lower side of this plate. The magnet lies in a mechanical arm that is able to perform harmonic oscillations in the $\tilde{x}$-direction, transversally to the direction of the electrodes, through the action of an electrical step motor controlled by a computer. The oscillation amplitude is 1.5 cm and the frequency can be varied in the range 0.3-2 Hz. The cell is partially filled with an electrolytic solution of potassium chloride at 8.6% by weight. The cell was mounted on a three point support and leveled to get a horizontal layer of water solution with uniform thickness of 0.4 cm. The mass density, kinematic viscosity and electrical conductivity of the electrolyte are $\rho = 1.09 \times 10^3$ Kg/m^3, $\nu = 10^{-6}$ m^2/s, and $\sigma = 18.1$ S/m, respectively. Under these conditions, the Hartmann number at the upper surface of the layer is approximately $Ha = 0.38$. The experiment started with the magnet in a fixed position and injecting the current in the $\tilde{x}$-direction through the electrodes. The Lorentz force set the fluid in motion and generated, after a transient state, a vortex dipole with a jet-like flow along the symmetry line ($\tilde{y}$-direction) in the main direction of the force.

4.3.1 Experimental results

Experiments were performed with electric currents within the range 0.11 to 0.67 A. In order to visualize the flow, a dye was introduced in the fluid. Once the dipole was completely formed, the magnet was set in harmonic oscillation with a specified frequency. If the injected current was less than $I = 0.38$ A, the base flow remained essentially unperturbed independently of the oscillation frequency of the magnet. The

[1] This section is based on the paper Beltrán et al. 2009

only noticeable effect for some frequencies was a slight wavy motion of the jet-like flow. For injected currents higher than 0.38 A, two different behaviors were observed according to the oscillation frequency (f). For $0.45 < f < 2$ Hz, the vortex dipole structure remains practically unperturbed. In turn, if the oscillation frequency is rather low ($0.3 < f \leq 0.45$ Hz), in the first cycles of oscillation the jet-like flow displayed a wavy flow pattern along the line of symmetry. Later on, in the neighborhood of the magnet local vortical structures were formed and shed periodically along the main direction of the Lorentz force. The higher the injected current the more intense the generation and shedding of the vortices. In Fig. 4.3.1 a sequence of pictures of the experimental flow is shown for $I = 0.628$ A and $f = 0.45$ Hz. It is observed that the vortex street presents a flapping around the symmetry $\tilde{y}$-axis. Note that the wall where the jet impinges affected the development of the vortical structures. These results point to the existence of a characteristic frequency able to destabilize the flow and lead to vortex shedding. Under these conditions the scalar transport is intensified.

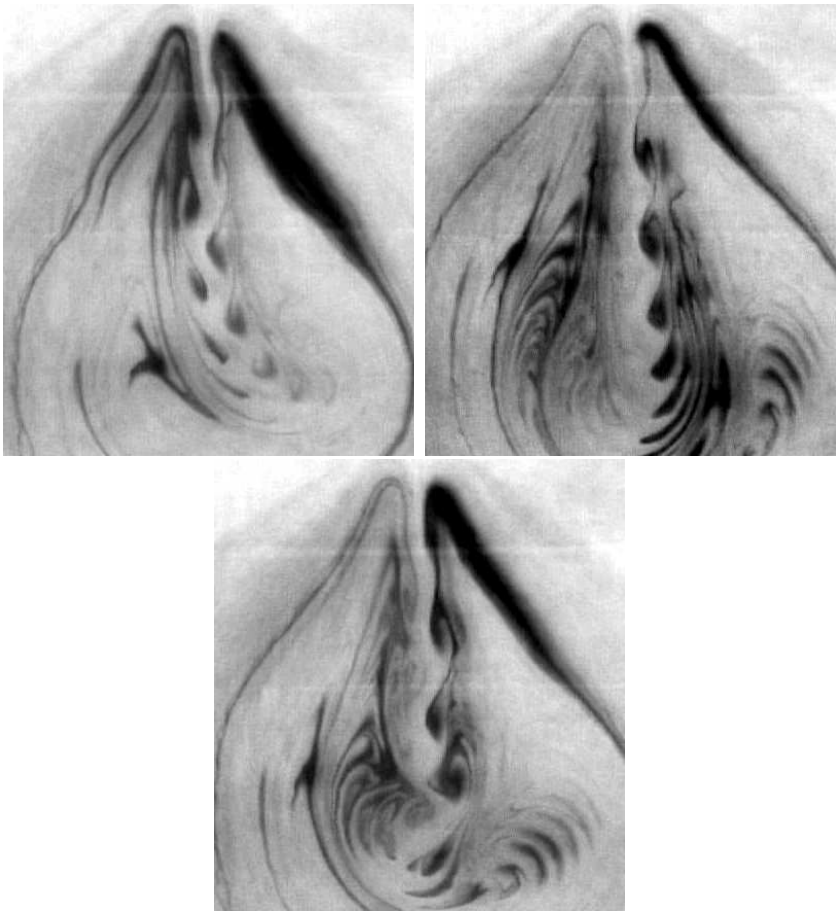

Figure 4.10: Experimental visualization of the flow generated by an oscillating magnetic obstacle with injected current in the direction parallel to the oscillation. $f = 0.45$, $I_0 = 0.628$,$B_{max} = 0.3T$.

4.3.2 Numerical results

A preliminary numerical simulation was carried out in order to reproduce approximately the experimental conditions with a two-dimensional model. Due to the presence of an injected current, the governing equations are slightly modified with respect to the case where only induced currents exist. In the present case, the electric current density is normalized by the injected current density. Therefore, the dimensionless equations that govern the flow dynamics are:

$$\frac{\partial \tilde{U}}{\partial \tilde{x}} + \frac{\partial \tilde{V}}{\partial \tilde{y}} = 0, \tag{4.15}$$

$$Re_\omega \frac{\partial \tilde{U}}{\partial \tilde{t}} + \tilde{U}\frac{\partial \tilde{U}}{\partial \tilde{x}} + \tilde{V}\frac{\partial \tilde{U}}{\partial \tilde{y}} = -\frac{\partial \tilde{P}}{\partial \tilde{x}} + \nabla_\perp^2 \tilde{U}, \tag{4.16}$$

$$Re_\omega \frac{\partial \tilde{V}}{\partial \tilde{t}} + \tilde{U}\frac{\partial \tilde{V}}{\partial \tilde{x}} + \tilde{V}\frac{\partial \tilde{V}}{\partial \tilde{y}} = -\frac{\partial \tilde{P}}{\partial \tilde{y}} + \nabla_\perp^2 \tilde{V} - Re\mathcal{B}_z^0, \tag{4.17}$$

Note that equation (4.17) now includes a constant force produced by the injected current.

where $Re = U_0 d/\nu$, and the characteristic velocity is defined as $U_0 = J_0 B_0 L^2/\rho\nu$. As discussed before, given the small value of the Hartmann ($Ha = 0.38$) number, inuced currents are also small and the flow is dominated by the Lorentz force produced by the injected current. The numerical procedure applied in section 3.2.2 was also used in this case, with no slip boundary conditions at the walls ($\tilde{U} = \tilde{V} = 0$). Figure 4.11 shows the Lagrangian tracking of advected particles once a periodic flow was established for $R_\omega = 125$ and $Re = 10^4$. The first parameter coincides with experimental conditions while the second was adjusted since the model does not consider the effect of the bottom friction. The numerical simulation reproduces some of the main characteristics observed in the experiments like vortex shedding and the flapping of the jet-like flow.

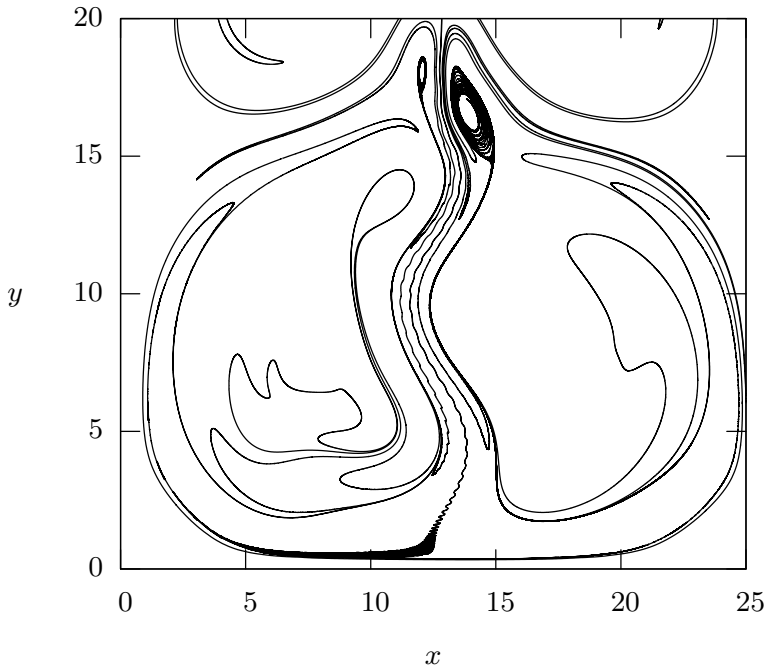

Figure 4.11: Numerical simulation of an oscillating magnetic obstacle with injected current. The lines correspond to Lagrangian particles advected by the periodic flow. $R_\omega = 125$, $Ha = 0.38$, $Re = 10^4$.

We found that the flow can be described as a jet-like structure emanating from the neighborhood of the magnet. For low frequencies, the oscillation of the magnet provokes the flapping of the jet-like flow and the periodic shedding of vortices generated in the magnetic obstacle region. This observation points to the conclusion that the jet is destabilized by a characteristic frequency of oscillation of the magnetic field.

Part of the results in this chapter have been published in

- Beltrán A., Cuevas S., Ramos E. and Smolentsev, S. "Vortex generation by an oscillatory localized magnetic field", Proceedings of the 7th International pamir Conference on Fundamental and applied MHD, Presqu'île de Giens, France, September 8-12, Vol. 1, pp. 415-420, (2008).
- Beltrán A., Cuevas S., Ramos E. Vortex generation by an oscillatory localized magnetic field. *Magnetohydrodynamics*, Vol. 45, No. 2, 173 - 180. 2009.
- Beltrán A., Cuevas S., Ramos E, Brøns M. Bifurcation analysis in a vortex flow generated by an oscillatory magnetic obstacle. *Physical Review E*, 81, (2010), 036309.

and presented in

- Beltrán, A., Cuevas, S. and Ramos, E. "Flow generated by an oscillatory magnetic obstacle". Presented at the *XIII Congress of the Division of Fluids and Pla smas, Mexican Physical Society*. October 28-Noviembre 1, 2007, Boca del Río, Veracruz. Mexico.
- Beltrán, A., Ramos, E. and Cuevas, S. - "Generation of local vortical structures in electromagnetically forced flow under a localized time-dependent magnetic field ". Presented at the *Second Latin American SCAT Workshop*. November 12-16, 2007, Cozumel, Mexico.
- Beltrán, A., Ramos, E. and Cuevas, S. - "Generation of local vortical structures in electromagnetically forced flow under a localized time-dependent magnetic field ". Presented at *The 60th Annual Meeting of the Divison of Fluid Dynamics American Physical Society*. November 18-20, 2007, Salt Lake City, Utah, USA.
- Beltrán, A., Cuevas, S. and Ramos, E. "Unstable vortical flow produced by an oscillatory non-uniform magnetic field". Presented at *The 61st Annual Meeting o f the Division of Fluid Dynamics of the American Physical Society*. November 23-25, 2008, San Antonio, Texas, USA.
- Beltrán, A., Ramos, E., Cuevas, S. and Brøns M. "Vortex generation by an oscillatory magnetic obstacle". Presented at the *Third International Symposium o n Bifurcations and Instabilites in Fluid Dynamics*. August 10-13, 2009, Nottingham, UK.
- Beltrán, A., Ramos, E., Cuevas, S. and Brøns M. "Flow generated by an oscillatory magnetic obstacle". Presented at *XV Congress of the Division of Fluids, Mexican Physical Society*. October 26-30, 2009, Acapulco, Mexico.

Chapter 5

Conclusions

In this thesis, the study of flows of electrically conducting fluids, either liquid metals or electrolytes, under spatially localized magnetic fields has been carried out, fundamentally, through a numerical simulation approach. In fact, important technological applications rely on a deep understanding of this kind of flows (e.g. electromagnetic braking, electromagnetic stirring, Lorentz force velocimetry). Nevertheless, from a fundamental perspective flows of conducting fluids in localized magnetic fields are worth exploring fluid dynamical systems which can shed new light on flows in ordinary hydrodynamics. We have developed suitable numerical models and computational strategies that allow their exploration offering new insights and providing a deeper physical understanding of these flows. Regarding such issues, some contributions have been presented.

From a mathematical point of view, the new proposed formulation of the MHD equations based on the electric current density (j-formulation) was introduced and tested through the modeling of the 2D LM flow past a magnetic obstacle. Results showed the viability of using this formulation in steady as well as in time-dependent MHD flows, presenting some potential advantages with respect to alternative formulations. Many developments are still to be considered, mainly the extension to 3D flows in ducts with conducting walls. On the other hand, using the B-formulation with a 2D numerical model, a peculiar dynamical behavior of a LM flow past a magnetic obstacle was explored as the Hartmann and Reynolds numbers were varied. We found that for a given Hartmann number, the flow is steady for small Reynolds numbers, becoming time-dependent, with periodic vortex shedding, as the Reynolds number grows. But in sharp contrast to the flow past a rigid obstacle, for even larger Reynolds numbers,

the flow becomes steady again. The stability curve in terms of Re and Ha was also obtained.

A Q2D model that accounts for the bottom friction effects in shallow flows of conducting fluids under localized magnetic fields was developed and applied to the analysis of flows with either liquid metals or electrolytes. The model was able to reproduce the main flow characteristics, reported experimentally (Kolesnikov et al. 2008), for the steady shallow flow of a liquid metal past a magnetic obstacle. In fact, the six vortex pattern was neatly obtained. To our knowledge, this is the first time that this kind of flow structure is reported using a Q2D numerical model. It seems that the three pair of vortices are due to a combination of the aspect ratio of the magnet and the width of the duct and not necessarily to 3D effects, as was claimed in the numerical study performed by (Votyakov, Zienicke, and Kolesnikov 2008). Also, for the case of electrolytic flows, the Q2D model was able to reproduce the flow patterns observed experimentally by Honji and Haraguchi (1995) although a complete agreement with the reported values of the governing parameters was not found, probably due to the lack of experimental information. On the other hand, a paralellized version of the numerical code was developed for the modeling of 3D flows of electrolytes under non-uniform magnetic fields, allowing the analysis of interesting 3D flow structures in different flow regimes. It was shown that it is possible to resolve MHD and hydrodynamical problems with large domains in an efficiently way. The code has run in a cluster with a free operating system and using MPI libraries; to our knowledge this is the first time that a parallelized code has been developed at CIE-UNAM to model fluid dynamic problems. The code is easily adaptable to model other flow configurations in cartesian coordinates.

The analysis of a physical situation that had not been previously reported in the literature, namely, the flow induced by an oscillatory magnetic obstacle, was also carried out in the present work. Two different situations were studied. First, we considered the effects of an harmonically oscillating localized magnetic field on a thin layer of liquid metal. The interaction of induced currents with the applied oscillating field, generate different vortex patterns according to the oscillation frequency. The analysis was performed through numerical simulations assuming a purely 2D LM flow. The numerical study shows that the flow is dominated by two counter rotating vortices with a structure similar to the ones observed in the rectilinear steady flow past a magnetic obstacle. The vortex pair changes its direction of rotation twice per cycle undergoing a flow transformation involving the interplay of critical points in the instantaneous streamlines that results in the flow reversal. In each cycle, two new pair of vortices are created and those generated previously are pushed away from the time average of the position of the magnetic obstacle. The transformation of the ow eld present in the rst part of the cycle into the pattern displayed in the second half occurs via the generation of hyperbolic and elliptic critical points. The numerical solution of the ow indicates

that for low frequencies two elliptic and two hyperbolic points are generated, while for high frequencies a more complex topology involving four elliptic and two hyperbolic points appear. The bifurcation map for critical points of the instantaneous streamline was obtained numerically and a theoretical model based on a local analysis that predicts most of the qualitative properties calculated numerically was proposed. Secondly, we also analyzed experimentally the flow produced by an oscillatory magnetic obstacle in a thin electrolytic layer when a D.C. current was injected in a direction parallel to the axis of oscillation of the magnetic field. Some preliminary numerical results were also obtained. The oscillatory localized Lorentz force produced a vortex dipole with a jet-like flow along the symmetry line in the direction of the force, perpendicular to both the injected current and the normal magnetic field. For certain oscillation frequencies of the magnet, the jet-like flow was destabilized and local vortical structures, formed in the neighborhood of the magnet, are swept away periodically by the base flow. Results showed that Lorentz forces created by injected and induced currents interacting with a harmonically oscillating localized field were able to destabilize the flow and enhance the stirring. This could be of potential interest for fluid mixing applications in a non-intrusive way.

The study of flows of conducting fluids in localized magnetic fields is rather incipient and very few reliable experimental data and numerical models are available in the literature. The advancement in this field require new experimental and numerical developments that can address the complexity of these flows and lead to deeper physical understanding as well as to relevant applications. It is expected that the results obtained in this thesis can offer some guidance for future works in this topic.

References

Abdou, M., A. Ying, N. Morley, K. Gulec, and S. Smolentsev (2001). On the exploration of innovative concepts for fusion chamber technology. - *APEX Interim Report Overview, Fusion Eng. Des. 54*, 181–247.

Afanasyev, Y. and V. Korabel (2008). Wakes and vortex streets behind a localized force: Numerical simulations. *Communications in Nonlinear Science and Numerical Simulation 13*(6), 1101 – 1111.

Afanasyev, Y. D. and V. Korabel (2006). Wakes and vortex streets generated by translating force and force doublet: laboratory experiments. *J. Fluid. Mech. 553*, 119–141.

Afanasyev, Y. D. and V. N. Korabel (2004). Starting vortex dipoles in a viscous fluid: Asymptotic theory, numerical simulations, and laboratory experiments. *Phys. Fluids. 16*(11), 3850–3858.

Alpher, A., H. Hurwitz, R. H. Johnson, and D. R. White (1960). Some studies of free surface mercury magnetohydrodynamics. *Rev. Mod. Phys. 32*, 758–769.

Andreev, O., Y. Kolesnikov, and A. Thess (2006). Experimental study of liquid metal channel flow under the influence of a nonuniform magnetic field. *Physics of Fluids 18*(6), 065108.

Andreev, O., Y. Kolesnikov, and A. Thess (2009). Application of the ultrasonic velocity profile method to the mapping of liquid metal flows under the influence of a non-uniform magnetic field. *Experiments in Fluids 46*(1), 77–83.

Bakker., P. G. (1991). *Bifurcations in Flow Patterns*. Kluwer Academic Publishers, Dordrecht.

Barret, R., M. Berry, T. Chan, J. Demmel, J. M. Donato, J. Dongarra, V. Eijkhout, R. Pozo, C. Romine, and H. V. der Vorst (1994). *Templates for the Solution of Linear Systems: Building Blocks for Iterative Methods*. SIAM.

Beltrán, A. (2006). *Flows of electrically conducting fluids past localized magnetic fields. MSc thesis (In Spanish)*. National University of Mexico.

Beltrán, A., S. Cuevas, and E. Ramos (2009). Vortex generation by an oscillatory magnetic obstacle. *Magnetohydrodynamics 45*(2), 173–180.

Brackbill, J. and D. Barnes (1980). The effect of nonzero on the numerical solution of the magnetohydrodynamic equations. *J. Comput. Phys. 35*, 426–430.

Braun, W., F. de Lillo, and B. Eckhardt (2006). Geometry of particle paths in turbulent flows. *Journal of Turbulence 7*(62), 1–10.

Brøns, M. (1999). Topological fluid mechanics of axisymmetric flows. *In J. N. Sørensen, E. J. Hopfinger and N. Aubry, editors,* Simulation and Identification of Organized Structures in Flows, 213–222.

Brøns, M. (2007). Streamline topology – patterns in fluid flows and their bifurcations. *Advances in Applied Mechanics 41*, 1–43.

Brøns, M., B. Jakobsen, K. Niss, A. V. Bisgaard, and L. K. Voigt (2007). Streamline topology in the near-wake of a circular cylinder at moderate reynolds numbers. *J. Fluid Mech. 584*, 23–43.

Bühler, L. (1996). Instabilities in quasi-two-dimensional magnetohydrodynamics flows. *J. Fluid Mech. 326*, 125–150.

Burr, U., L. Barleon, U. Müller, and A. Tsinober (2000). Turbulent transport of momentum and heat in magnetohydrodynamic rectangular duct flow with strong side wall jets. *J. Fluid Mech. 406*, 247–279.

Chen, D. and H. G. Jirka (1997). Absolute and convective instabilities of plane turbulent wakes in a shallow water layer. *J. Fluid Mech. 338*, 157–172.

Cuevas, S., S. Smolentsev, and M. A. Abdou (2006a). On the flow past a magnetic obstacle. *J. Fluid. Mech. 553*, 227–252.

Cuevas, S., S. Smolentsev, and M. A. Abdou (2006b). Vorticity generation in the creeping flow past a magnetic obstacle. *Phys. Rev E 70*, 053601.

Davidson, P. A. (1999). Magnetohydrodynamics in materials processing. *Annu. Rev. Fluid Mech. 31*, 273–300.

Davidson, P. A. (2001). *Introduction to magnetohydrodynamics flows*. Cambridge.

Figueroa, A., F. Demiaux, S. Cuevas, and E. Ramos (2009). Electricalli driven vortices in a weak dipolar magnetic field in a shallow electrolytic layer. *J. Fluid Mech. 641*, 245–261.

Frank, M., L. Barleon, and U. Müller (2001). Visual analysis of two dimensional magnetohydrodymanics. *Phys. Fluids 13*, 2287–2295.

Gelfgat, Y. M. and S. V. Olshanskii (1978). Velocity structure of flows in nonuniform constant magnetic fields. ii. experimental results. *Magnetohydrodynamics 14*, 151–154.

Gelfgat, Y. M., D. E. Peterson, and E. V. Shcherbinin (1978). Velocity structure of flows in nonuniform constant magnetic fields 1. numerical calculations. *Magnetohydrodynamics 14*, 55–61.

Goto, S., D. R. Osborne, J. C. Vassilicos, and J. D. Haigh (2005). Acceleration statistics as measures of statistical persistence of streamlines in isotropic turbulence. *Physical Review E 71*, 015301(R).

Griebel, M., T. Dornseifer, and T. Neunhoeffer (1998). *Numerical Simulation in Fluid Dynamics*. SIAM.

Gurcan, F. and A. Deliceoğlu. (2005). Streamline topologies near nonsimple degenerate points in two-dimensional flows with double symmetry away from boundaries and an application. *Phys. Fluids 17*, 093106.

Hansen, A. E., D. Marteau, and P. Tabeling (1998). Two-dimensional turbulence and dispersion in a freely decaying system. *Phys. Rev. E 58*, 7261–71.

Honji, H. (1991). Wavy wake formation in the absence of sumerged bodies in electrolyzed salt water. *J. Phys. Soc. Japan 60*, 1161–1164.

Honji, H. and Y. Haraguchi (1995). Electrolytically induced quasi-two dimensional vortex pairs. *J. Phys. Soc. Japan 64*, 2274–2277.

Kolesnikov, Y., C. Karcher, and V. Minchenya (2008). Lorentz force velocimetry: Development and application. *Proceedings of the 7th International pamir conference on Fundamental and applied MHD; Presqu'île de Giens 2*.

Kunstreich, S. (2003). Electromagnetic stirring for continuous casting. *Rev. Met. Paris 4*, 395–408.

Leboucher, L. (1999). Monotone scheme and boundary conditions for finite volume simulation of magnetohydrodynamic internal flows at high hartmann number. *J. Comput. Phys. 150*, 181–198.

Legendre, R. (1956). Séparation de l'écoulement laminaire tridimensionel. *La recherche aérospatiale 54*, 3–8.

McCaig, M. (1977). *Permanent magnets in theory and practice*. Wiley.

Moreau, R. (1990). *Magnetohydrodynamics*. Kluwer Academic Publishers, Dordrecht/Boston/London.

Mück, B., C. Günther, U. Müller, and L. Bühler (2000). Three-dimensional mhd flows in rectangular ducts with internal obstacles. *J. Fluid Mech. 418*, 265–295.

Müller, U. and L. Bühler (2001). *Magnetofluiddynamics in Channels and Containers.* Springer.

Oertel, H. (1990). Wakes behind blunt bodies. *Annu. Rev. Fluid Mech. 22*, 539–564.

Ouellette, N. T. and J. P. Gollub (2007). Curvature fields, topology, and the dynamics of spatiotemporal chaos. *Phys. Rev. Lett. 99*(19), 194502.

Perry, A. E. and B. D. Fairlie (1974). Critical points in flow patterns. *Advances in Geophysics 18B*, 299–315.

Reed, C. B. and B. F. Picologlou (1989). Side wall flow instabilities in liquid-metal flow under blanket relevant conditions. *Fusion Technol. 15*, 705–715.

Riley, N. (2001). Steady streaming. *Annu. Rev. Fluid Mech. 33*, 43–65.

Rossi, L., J. C. Vassilicos, and Y. Hardalupas (2006a). Electromagnetically controlled multi-scale flows. *J. Fluid Mech. 558*, 207–242.

Rossi, L., J. C. Vassilicos, and Y. Hardalupas (2006b). Multiscale laminar flows with turbulentlike properties. *Phys. Rev. Lett. 97*, 144501.

Rothstein, D., E. Henry, and J. P. Gollub (1999). Persistent patterns in transient chaotic fluid mixing. *Nature 401*, 770–772.

Schlichting, H. and K. Gertsen (2000). *Boundary layer theory* (8th ed.). Springer.

Schmid, P. J. and D. S. Henningson (2001). *Stability and flow transition in shear flows*. Springer.

Shercliff, J. A. (1956). The flow of conducting fluids in circular pipes under transverse magnetic fields. *J. Fluid Mech. 6*, 644–666.

Shercliff, J. A. (1965). *Magnetohydrodynamics*. A film produced by Educational Services Inc. Watertown, Massachusetts, USA.

Smolentsev, S. (1999). Mathematical models for magnetohydrodynamic flows in a fusion reactor blanket. *Plasma Dev. Operat. 7*, 231–241.

Smolentsev, S., S. Cuevas, and A. Beltran (2010). Induced electric current-based formulation in computations of low magnetic reynolds number magnetohydrodynamic flows. *J. Comp. Phys. 229*, 1558–1572.

Smolentsev, S., S. Cuevas, and A. Beltrán (2010). Induced electric current-based formulation in computations of low magnetic reynolds number magnetohydrodynamic flows. *J. Comput. Phys. 229*(5), 1558 – 1572.

Smolentsev, S., N. B. Morley, M. Abdou, R. Munipalli, and R. Moreau (2006). Current approaches to modeling mhd flows in the dual coolant lead lithium blanket. *Magnetohydrodynamics 42*, 225–236.

Takeuchi, S., J. Kubota, Y. Miki, H. Okuda, and A. Shiroyama (2003). Change and trend of molten steel flow technology in a continous casting mould by electromagnetic force. *In Proc. EPM-Conference. Lyon, France*.

Tannehill, J. C., D. A. Anderson, and R. H. Pletcher (1997). *Computational Fluid Mechanics and Heat Transfer* (Second ed.). Taylor & Francis.

Thess, A., E. V. Votyakov, and Y. Kolesnikov (2006, Apr). Lorentz force velocimetry. *Phys. Rev. Lett. 96*(16), 164501.

Votyakov, E. V. and S. C. Kassinos (2009). On the analogy between streamlined magnetic and solid obstacles. *Physics of Fluids 21*(9), 097102.

Votyakov, E. V., Y. B. Kolesnikov, O. Andreev, E. Zienicke, and A. Thess (2007). Structure of the wake of a magnetic obstacle. *Phys. Rev. Lett. 98*(14), 144504.

Votyakov, E. V. and E. Zienicke (2007). Numerical study of liquid metal flow in a rectangular duct under the influence of a heterogenous magnetic field. *Fluid Dynamics and Materials Processing 3*(2), 97–113.

Votyakov, E. V., E. Zienicke, and Y. Kolesnikov (2008). Constrained flow around a magnetic obstacle. *J. Fluid Mech. 610*, 131–156.

Walker, J. S. (1981). Magnetohydrodynamic flows in rectangular ducts with thin conducting walls. *Journal de Mècanique 20*(1), 79–112.

Weiss, J. (1992). The dynamics of enstrophy transfer in two-dimensional hydrodynamics. *Physica D 48*(273).

Williamson, C. K. H. (1996). Vortex dynamics in the cylinder wake. *Annu. Rev. Fluid Mech. 28*, 477–.

Zdrakovich, M. M. (1997). *Flow around Circular Cylinders. Vol. 1: Fundamentals*. Oxford.